Circulation and Upwelling in Mackenzie Canyon, a Dynamically Wide Submarine Canyon in the Beaufort Sea

by

Idalia Alicia Machuca

B.Sc. Geophysics, The University of British Columbia, 2014

A.Sc. Physics and Mathematics, St. John's College Junior College, 2010

A THESIS SUBMITTED IN PARTIAL FULFILLMENT

OF THE REQUIREMENTS FOR THE DEGREE OF

Master of Science

in

THE FACULTY OF GRADUATE AND POSTDOCTORAL STUDIES

(Oceanography)

The University of British Columbia

(Vancouver)

April 2019

The following individuals certify that they have read, and recommend to the Faculty of Graduate and Postdoctoral Studies for acceptance, the thesis entitled:

Circulation and Upwelling in Mackenzie Canyon, a Dynamically Wide Submarine Canyon in the Beaufort Sea

submitted by **Idalia Alicia Machuca** in partial fulfillment of the requirements for the degree of **Master of Science** in **Oceanography**.

Examining Committee:

Susan Allen, Earth, Ocean and Atmospheric Sciences
Supervisor

Michael Dunphy, Fisheries and Oceans Canada
Supervisory Committee Member

Brian Hunt, Institute for the Oceans and Fisheries
Supervisory Committee Member

Stephanie Waterman, Earth, Ocean and Atmospheric Sciences
Supervisory Committee Member

Rich Pawlowicz, Earth, Ocean and Atmospheric Sciences
External Examiner

Abstract

Mackenzie Canyon, in the southeastern Beaufort Sea, is a site for strong upwelling compared to the adjacent continental shelf and slope and potentially supplies the shelf with significant levels of nitrate. Research regarding the circulation and upwelling mechanisms in submarine canyons has previously been limited to dynamically narrow canyons, and most studies have used numerical models with idealized bathymetry. The main goal of the study presented in this thesis is to describe the circulation and upwelling in Mackenzie Canyon, which is classified as a dynamically wide canyon. This study also identifies key flow features that act as significant modifiers of upwelling, examines differences between idealized and realistic model simulations, and estimates the canyon-induced upwelling of nitrate.

To address these goals, the circulation and upwelling associated with an upwelling event induced by an impulsive wind forcing in Mackenzie Canyon was simulated using a nested-grid modelling system configuration based on the Nucleus for European Modelling of the Ocean framework. Numerical simulations were conducted using realistic and idealized bathymetry and three cases of wind stress forcing. The model performance was evaluated using observational data from Mackenzie Canyon during an upwelling event.

This study finds that near-geostrophic flows are topographically steered around the Mackenzie Canyon walls. Strong cyclonic vorticity is generated on the upstream corner of the canyon mouth and evolves into a closed, cyclonic eddy, which becomes a site for strong upwelling. A coastal trapped wave (CTW) is induced on the downstream side of the canyon and propagates upstream. It is characterized as a shelf wave using a model that searches for the free wave solutions of CTWs along straight coastlines. An upwelling signal in the canyon exits the canyon and propagates along the slope with the CTW. Unlike narrow canyons, upwelling in Mackenzie Canyon is stronger on the upstream side than on the downstream side, likely as a consequence of the upstream propagation of the CTW. The nitrate flux

across the nitracline depth supplied by upwelling in Mackenzie Canyon during the initial 36 hours of an upwelling event is estimated to be twice the seasonal draw-down in the Beaufort Sea.

Lay Summary

Submarine canyons are steep, complex topographic features off the world's coasts. These regions are characterized by unique circulation patterns and strong upwelling, which is an oceanographic phenomenon whereby water from deeper layers of the ocean is driven upward. Nutrient-rich water delivered by upwelling to the top layers of the ocean fertilizes photosynthetic organisms near the surface which support coastal populations of fish, mammals, and birds.

Research using computer models of the ocean circulation to study the mechanisms driving upwelling in submarine canyons has previously only focused on narrow canyons and mostly used simplified canyon bathymetry. This project studies the different circulation and upwelling patterns in Mackenzie Canyon, which is a wide canyon, and compares the results of models which use simplified and realistic bathymetry. This study finds that upwelling in Mackenzie Canyon is sufficiently strong to support high biological productivity in the region.

Preface

This thesis is the original work of the author, Idalia Alicia Machuca. The research project presented in this thesis was supervised by Susan Allen, who assisted with the model configuration, interpretation of results, and manuscript editing. The numerical experiments were conducted using the NEMO (Nucleus for European Modelling of the Ocean) ocean modelling framework. The AGRIF (Adaptive Grid Refinement in Fortran) software was used to implement a nested grid, which was primarily configured by Michael Dunphy. Model evaluation was conducted using observational data provided by Amy Waterhouse. This work is unpublished, but it is undergoing preparation for future publication.

Table of Contents

List of Tables

List of Figures

Acknowledgments

I extend my heartfelt gratitude and appreciation to everyone who has been a part of my journey in graduate school. Susan, you have been not only a supportive and encouraging supervisor and mentor, but also an incredible role model. Your dedication to fostering an inclusive, empowering, and caring environment for your students has enriched my experience in the Waterhole. Stephanie, Michael, Brian, thank you for your guidance and enthusiasm throughout the completion of this project.

Folks of the Waterhole, I am truly lucky to have you all in my life! Thank you for the hugs, words of encouragement, mid-afternoon chats and coffee breaks, and Friday evening excursions around Vancouver. Special thanks to my fellow colleagues from the Submarine Canyons - Arctic group, Karina, Birgit, Saurav, and Gonzalo, who have been like family away from home.

Rob, thank you for your unwavering confidence that this day was just around the corner and for reminding me of a bright future.

Thank you to my family, and especially to my abuelitos, for tirelessly cheering me on over the years and nurturing the curiosity and dedication that has proven invaluable for this endeavour.

Finally, I dedicate this thesis to my mother, who is my hero, inspiration, and pillar of strength. Everything that has led to this moment would not have been possible without you.

Dedication

Por tus esfuerzos, sacrificios, y valentía.

Por tus consejos y oraciones.

Y sobre todo, por el amor y apoyo incondicional que me has brindado.

Te la dedico, mami. Lo logramos!

Chapter 1

Introduction

1.1 Motivation for submarine canyons research

Submarine canyons are "relatively narrow, deep depressions with steep sides" (Bouma, 1990) that incise the shelves and slopes of all continental margins. The origin and evolution of submarine canyons is attributed to mass wasting events, erosive turbidity currents, tectonic activity, and subaerial erosion by rivers and glaciers during the last ice age. A comprehensive database of the topographic features of the world's major oceans called the Global Seafloor Geomorphic Features Map (Harris and Whiteway, 2011) identifies 9477 individual canyons. Submarine canyons are classified as either shelf-incising (2,076 of the total, often associated with a major river system) or blind (7,401 of the total, confined to the continental slope). On average, the areas (777 km^2 vs. 375 km^2) and lengths (54.8 km vs. 37.3 km) are greater for shelf-incising canyons than for blind canyons. In total, canyons make up 1.21% of the global ocean area and 11.2% of the global continental slope area. The pervasiveness and coverage of submarine canyons along the world's continental slopes draw attention to their role in local physical, sedimentary, and ecological dynamics.

The knowledge network related to submarine canyons has been mapped using information retrieval techniques on a large volume of relevant publications, and it shows that submarine canyon research consists of various knowledge clusters spanning geology, oceanography, and ecology (Matos et al., 2018). The largest cluster, *Geology and Geophysics*, arises early in the history of submarine canyon research and deals with the geomorphology, sediment dynamics, and geological survey and sampling of submarine canyons. *Biology and Ecology* is the second largest cluster and initially focused on community

composition and trophic structure of benthic ecosystems in canyon systems. Technological developments and the use of multidisciplinary data from observatory networks have further expanded this field to include environmental and conservation work. *Oceanographic Processes*, which includes work on oceanographic phenomena, seasonal variability, and particle transport, is found at the core of the submarine canyons research network as it shares many connections with the other clusters. For example, a *Modelling* cluster, which has emerged recently and shares a strong connection with *Oceanographic Processes*, includes topics that range from currents and internal waves to distribution patterns of whales and larvae, all addressed via modelling approaches. Technological advancements in both sampling and computing have led to growing interdisciplinarity in research regarding not only canyons but also coastal and deep-ocean environments. The work presented in this thesis explores oceanographic processes in one submarine canyon region and considers the resulting biological implications using numerical modelling.

Although submarine canyon research is conducted by many institutions and researchers in over 50 countries, the work has been focused on a limited number of canyons (Matos et al., 2018). The 11 most studied canyons account for 48% of the research effort and have more than 50 associated publications each. These canyons are, in descending order of publications, Monterey, Baltimore, Hudson, Gully, Nazare, Lacaze-Duthiers, Cap de Creus, Blanes, Gaoping, La Jolla, and Alaminos, and are located along the Pacific and Atlantic coasts of North America, the South China Sea coast of Taiwan, and the Mediterranean. The interest in these canyons may be derived from their proximity to research institutions, scientific or economic interest in their geology and/or ecology, or continual effort building upon previous data collection. It is crucial to acknowledge, however, that the shortage of studies on submarine canyons in other major regions, such as the Arctic, South Atlantic, South Pacific, Indian, and Southern Oceans, may compromise our understanding of the variability of canyon dynamics and processes. The role of submarine canyons on oceanic processes in the Arctic region may be of particular interest since the largest and longest shelf-incising canyons, with an average size of 2160 km^2 and mean length of 99.6 km, are located along the Arctic shelves and slopes (Harris and Whiteway, 2011). In fact, compared to the other major ocean regions, the Arctic Ocean has the highest percentage (16.1%) of the slope area covered by canyons (Harris and Whiteway, 2011). The subject of this study is Mackenzie Canyon, a shelf-incising canyon associated with the Mackenzie River and located in the southeastern Beaufort Sea in the Arctic Ocean. As such, this work will provide insight into the oceanic processes in a region that has yet to be adequately studied.

Submarine canyons have been described as "keystone structures" (Vetter et al., 2010) because they provide social and economic services that impact human wellbeing (Fernandez-Arcaya et al., 2017; Jobstvogt et al., 2014). Services provided by canyons can be classified as provisioning (the direct products derived from an ecosystem), regulating (the benefits offered by an ecosystem's regulatory processes), or supporting (the underlying processes that support these services). Supporting services include water circulation and exchange by up/downwelling, turbidity currents, hyperpycnal flows, dense shelf water cascading, and mixing (Jobstvogt et al., 2014; Puig et al., 2014). These processes support regulating services, such as nutrient and sediment cycling, carbon sequestration, and removal of pollutants from shelf areas. Canyons also contribute to the biodiversity of coastal regions by acting as nurseries for demersal fish and other mobile species (Johnson et al., 2013), recruitment grounds for juvenile fish and crustaceans (Sardà et al., 1994), and refugia from predation and anthropogenic disturbances (Huvenne et al., 2011). Consequently, canyons offer provisioning services as prime locations for commercial fishing (Martín et al., 2014; Puig et al., 2012) and several form Marine Protected Areas (Hooker et al., 1999; Sanchez et al., 2013). Research on the various elements involved in these services plays a critical role in not only increasing our understanding on these dynamic regions, but also supporting proper management and protection measures through science-based decision-making.

Submarine canyons are sites for strong down-canyon and up-canyon flows, mixing, and internal wave generation and breaking. Downwelling and other down-canyon currents are known as "concentrating processes" (Moors-Murphy, 2014) since these processes supply organic matter derived from surface primary production over the canyon to the benthic community on the seabed (Leduc et al., 2014). Other down-canyon currents include turbidity currents, which are high-velocity, turbulent, sediment-laden plumes that flow down-slope as a result of having higher density than the surrounding water due to their high particle concentration. These currents are triggered by shelf sediment resuspension induced by storms, sediment slumping and submarine slides along canyon walls, failures of sediments recently deposited by fluvial sources, and sediment resuspension induced by bottom-trawling (Puig et al., 2012, 2014; Sanchez-Vidal et al., 2012). Canyons associated with river mouths may also experience hyperpycnal flows, which are gravity flows driven by the density contrast caused by excess sediments supplied by high river discharge during floods (Liu et al., 2009; Puig et al., 2014). In contrast, dense shelf water cascading involves currents that are driven by the density contrast of the water itself. As shelf waters cool or evaporate, they may become dense enough to sink and initiate a down-slope current (Canals et al.,

2006; Pasqual et al., 2010). These down-canyon flows export high amounts of resuspended sediments containing aged (eroded from the shelf and canyon head) and new (derived from any coinciding phytoplankton blooms) organic carbon at higher sedimentation rates than the adjacent slope (Canals et al., 2013; Masson et al., 2010; Zúñiga et al., 2009). The accumulation of organic material on the canyon floor not only promotes high abundance and diversity of demersal and benthic organisms (Brodeur, 2001; De Leo et al., 2012), such as detritivores and suspension feeders (Moors-Murphy, 2014; Vetter et al., 2010), but also reveals canyons as significant sinks for organic carbon (Masson et al., 2010).

In contrast, upwelling and mixing are considered "enrichment processes" (Moors-Murphy, 2014) that transport nutrient-rich water from the deep ocean to the euphotic zone (Allen et al., 2001). Episodes of canyon upwelling involve up-canyon flows that are driven by an unbalanced cross-shelf pressure gradient associated with currents flowing with the shallower side to the left in the Northern Hemisphere, and vice versa in the Southern Hemisphere (Allen and Durrieu De Madron, 2009; Freeland and Denman, 1982). Other enrichment processes in canyons include the elevated levels of mixing and turbulence produced by the generation and breaking of internal waves and the focusing of internal tides on canyon topography (Gardner, 1989; Gordon and Marshall, 1976; Hall et al., 2017). Altogether, the increased supply of nutrients to the euphotic zone by these processes stimulates primary production (Bosley et al., 2004; Hickey and Banas, 2008; Ryan et al., 2005), which in turn supports high zooplankton abundance and attracts large pelagic fish and cetaceans (Allen et al., 2001; Brodeur, 2001; Hooker et al., 1999; Moors-Murphy, 2014; Rennie et al., 2009). The dynamics involved in canyon upwelling are described in Section 1.2.

1.2 Upwelling dynamics in submarine canyons

In this thesis, the *alongshore* and *cross-shore* directions refer to the movement of flows or winds along or across the shelf or shore isobaths. In the cross-shore direction, flows can be *onshore* or *offshore* (i.e. towards or away from the coast). Alongshore flows are described as *up-shelf/downstream* when the shallower side (or coast) is to the left of the flow in the Northern Hemisphere, and vice versa in the Southern Hemisphere. Conversely, *down-shelf/upstream* refer to the opposite direction. In the Northern Hemisphere, flows are considered *left-bounded* if movement is in the downstream/up-shelf direction, and vice versa in the Southern Hemisphere. In canyons, the *cross-canyon* and *along-canyon* directions are taken across the canyon width (i.e. alongshore) and along the canyon length (i.e. cross-shore),

respectively. Additionally, the sides of a canyon are referred to as upstream or downstream based on this vocabulary. These terms are summarized in Figure 1.1.

Coastal upwelling is associated with an alongshore, up-shelf wind stress, which induces offshore-directed Ekman transport of the surface layers. As surface water moves offshore, the sea level lowers towards the coast and creates an onshore pressure gradient. The pressure gradient is generally balanced by the Coriolis force, and a geostrophic current is initiated in the up-shelf direction. Due to mass conservation, deeper water is upwelled to replace the surface water that was carried offshore. Although initiated by similar forcing, canyon upwelling involves a more complex series of processes and produces stronger upwelling compared to its adjacent shelf (Allen, 1996).

The response of a submarine canyon to shelf currents is largely dependent on the canyon width and stratification (Allen, 2000; Hickey, 1997; Hyun, 2004; Klinck, 1996). Canyons are considered dynamically narrow, intermediate, or wide depending on the ratio between the canyon width W and the internal Rossby radius of deformation a (Klinck, 1988, 1989). The internal Rossby radius of deformation $a = NH_c/f$ (Hickey, 1997; Klinck, 1996; Williams et al., 2006) characterizes the horizontal scale at which rotation and gravity (in this format, through stratification) are equally significant. For these expressions, N is the Brunt-Väisälä or buoyancy frequency where $N^2 = -g/\rho_o \partial \rho / \partial z$, H_c is the depth of the canyon at the mouth, f is the Coriolis parameter, g is the gravitational acceleration, ρ is the density, ρ_o is a reference density, and z is the vertical coordinate. Flows with length scales greater than the deformation radius are generally geostrophic. Canyons with widths W smaller than $2a$ are considered "narrow" (Hyun, 2004), and have been extensively studied (Allen and Hickey, 2010; Hickey, 1997; Klinck, 1988, 1996). The details regarding the circulation and upwelling response associated with narrow canyons are described below.

Geostrophic currents upstream of a canyon are supported by an onshore, barotropic pressure gradient produced by the tilted free surface. The pressure gradient is balanced by the Coriolis force and the resulting geostrophic flow is constrained to follow isobaths, thereby inhibiting transport up the steep topography. In a narrow canyon, however, alongshore flow is prevented by the canyon walls and the effect of the Coriolis force is secondary compared to other terms in the momentum balance (Allen, 2004). As a result, flow inside the canyon is driven down the unbalanced, onshore pressure gradient and is allowed to move along-canyon and up the topography (Allen, 1996; Freeland and Denman, 1982; Klinck, 1988, 1989; She and Klinck, 2000). Thus, the enhanced upwelling observed in narrow submarine canyons is

driven by the onshore, barotropic pressure gradient over the shelf which is unbalanced due to the canyon topography (Allen, 2004).

Throughout an upwelling event, the continuous tilting of isopycnals associated with the upwelling transport inside the canyon generates an offshore, baroclinic pressure gradient to compensate for the onshore, barotropic pressure gradient above the canyon rim (Klinck, 1996; She and Klinck, 2000). The baroclinic pressure gradient force due to the tilting isopycnals eventually balances the barotropic pressure gradient force associated with the offshore surface transport, inhibiting further upwelling inside the canyon (Howatt and Allen, 2013). The upwelling depth $\mathcal{Z}$ (Figure 1.2) is considered an important characteristic of upwelling in submarine canyons (Allen and Hickey, 2010; Howatt and Allen, 2013). Assuming upwelling occurs mostly near the head with little or none at the mouth, the upwelling depth is defined as the change in depth of the deepest isopycnal that is upwelled onto the shelf over the rim of the canyon at the canyon head. In other words, this isopycnal is upwelled from a depth $\mathcal{Z} + H_h$ to the head at depth H_h (Figure 1.2). At the depth of this isopycnal at the canyon mouth (i.e. $\mathcal{Z} + H_h$), where upwelling is minimal, a balance is expected between the barotropic pressure gradient force due to the tilting free surface and the baroclinic pressure gradient force due to the tilting isopycnals inside the canyon (Allen and Hickey, 2010; Howatt and Allen, 2013). An estimate for the barotropic pressure gradient, which drives the upwelling event, can be made by first considering the directionality of flow over the canyon.

The Rossby number characterizing flows over a canyon is typically based on the width of the canyon at half-length and is defined as $R_{W*} = U/f\mathcal{R}_W$, where U is the velocity scale upstream of the canyon and $\mathcal{R}_W$ is the width of the canyon taken half-way along the canyon length and measured across the shelf break isobath (Howatt and Allen, 2013). A Rossby number quantifies the relative scales of the inertial acceleration of a flow to the magnitude of the Coriolis force deflecting the flow and, in the case of the Rossby number R_{W*}, indicates the degree to which the incoming shelf currents will follow the canyon topography or flow across it (Figure 1.3). For narrow canyons (large R_{W*}), the inertial acceleration will be large enough for the shelf currents to flow past the upstream side of the canyon mouth before being deflected onshore (Allen, 2004). If the flow crosses the canyon without significant onshore deflection, then the cross-shelf pressure gradient will be similar to that on the shelf away from the canyon (Allen and Hickey, 2010). Therefore, for a narrow canyon, the pressure gradient force over the canyon is approximated to be on the order of $\rho_o f U \mathcal{F}_{W*}(R_{W*})$ (Allen, 2004; Howatt and Allen, 2013), while the

pressure gradient force due to the tilting isopycnals is on the order of $\rho_o N^2 \mathcal{Z}^2$, where ρ_o is a reference density, f is the Coriolis parameter, U is the velocity of the incoming shelf currents, and N is the Brunt-Väisälä buoyancy frequency. Here, $\mathcal{F}_{W*} = R_{W*}/(0.9 + R_{W*})$ is a function of the Rossby number R_{W*} and ranges between 0 and 1 (Howatt and Allen, 2013). The function $\mathcal{F}_{W*}$, therefore, shows the role of the Rossby number R_{W*} in describing the ability of the canyon flow to generate the pressure gradient that drives upwelling.

In contrast, flows over wide canyons (low R_{W*} and $W > 2a$) are expected to be steered by and around the canyon topography (Allen, 2004), and the cross-shelf pressure gradient considered to be the main driver for upwelling in narrow canyons is expected to be negligible (Allen and Hickey, 2010). For this reason, it was originally assumed that wide canyons would only distort flows to move along the canyon isobaths without generating any substantial upwelling (Klinck, 1988, 1989). Numerical experiments varying canyon width (Hyun, 2004), however, show that upwelling does occur in canyons wider than twice the internal radius of deformation. The characteristics of the circulation and upwelling observed in both narrow and wide canyons are detailed below.

Circulation inside a canyon during an upwelling event is typically thought to evolve in three stages (Waterhouse et al., 2009, Figure 5) based on the response of the flow to the influence of the canyon topography (Allen and Durrieu De Madron, 2009). The initial, transient stage of upwelling is referred to as the acceleration phase since it covers the period during which upwelling-favourable winds produce an offshore Ekman transport which removes water from the upper Ekman layer at a constant rate (Allen, 1996). As such, the amount of water removed near the coast increases linearly, and the horizontal velocity of the shelf currents increases in time. The momentum balance describing this stage is:

$$\frac{\partial \vec{u}}{\partial t} + f\hat{k} \times \vec{u} = \frac{-1}{\rho_o} \nabla p \tag{1.1}$$

where the first term on the left hand side represents the acceleration of shelf currents, the second term represents the Coriolis acceleration, the term on the right hand side represents the onshore pressure gradient force per unit mass, $\vec{u}$ is the horizontal velocity, t is time, f is the Coriolis parameter, ρ_o is a reference density, and p is the pressure. As the upwelling event progresses and flows over the shelf reach constant velocity, advection replaces time-dependence as the dominant process for upwelling (Allen, 1996, 2004). The quasi-steady, advection-driven stage is described by:

7

$$\vec{u} \cdot \nabla \vec{u} + f\hat{k} \times \vec{u} = \frac{-1}{\rho_o} \nabla p \qquad (1.2)$$

where the first term on the left hand side represents the non-linear, advection of momentum per unit mass. The third and final stage, the relaxation stage of upwelling, occurs once the shelf current velocities decrease towards the end of the event (Allen and Durrieu De Madron, 2009).

During the time dependent stage of upwelling in a narrow canyon, currents along the slope enter the canyon through the mouth and move towards the downstream wall. At the downstream wall, flows either upwell onto the shelf, continue towards the head or turn offshore to exit the canyon. Flows inside narrow and long canyons are typically slow and form a weak cyclonic circulation (Waterhouse et al., 2009). Notably, there is a narrow band of downwelling along the upstream wall (Klinck, 1996) as the onshore flux upstream of the canyon is redirected through the canyon (Allen, 1996). As velocities inside the canyon continue to decrease into the advection-driven stage, the cyclonic circulation evolves into a cyclonic eddy at the canyon rim depth and cyclonic vorticity develops deeper inside the canyon (Allen, 1996; Waterhouse et al., 2009). Flows are advected into the canyon and upwelled onto the shelf over the downstream wall near the canyon head. At the downstream wall, anticyclonic vorticity develops (Allen et al., 2001; Allen, 2004) and upwelled flows over the shelf turn offshore towards the shelf break (Waterhouse et al., 2009).

The generation of the cyclonic vorticity inside narrow canyons has been attributed to flow separation from the topography on the upstream corner of the canyon mouth (Pérenne et al., 2001; She and Klinck, 2000) and to vortex stretching due to shelf flows dipping into the canyon on the upstream side (Hickey, 1997; She and Klinck, 2000). Vortex stretching, however, is found to be the dominant mechanism (Waterhouse et al., 2009). Shelf flows passing over the canyon rim plunge into the canyon and stretch the water column. Due to the conservation of potential vorticity, stretching the water column generates cyclonic vorticity on the upstream side of the canyon (Hickey, 1997). Similarly, stretching due to tilting isopycnals generate cyclonic vorticity deeper in the canyon (Allen, 2004; Klinck, 1996; She and Klinck, 2000). Conversely, anticyclonic vorticity is generated on the downstream side of the canyon by the fluid column being compressed as upwelling flows are advected onto the shelf (Allen, 2004; Klinck, 1996; She and Klinck, 2000).

Wide (e.g. $W/a \sim 3$) and intermediate-sized (e.g. $W/a \sim 1.5$) canyons exhibit similar circulation

features as narrow canyons, but the coverage, shape, strength of, and dynamics behind such features are different (Hyun, 2004). In wider canyons, the surface elevation is higher in the centre of the canyon compared to either side since the canyon walls are sufficiently far apart to only weakly interact (ibid.). This pressure distribution most likely allows flows entering the canyon on the upstream side to move around the canyon walls and form an anticyclonic circulation. The mean flow inside the canyon has been found to weaken as the canyon becomes wider (ibid.). During the initial stage of the upwelling event, flows are directed onshore along the upstream wall, downstream around the canyon head, and offshore along the downstream wall (ibid.). With increasing wind-stress forcing, the incoming currents along the upstream slope strengthen and separate from the upstream corner of the canyon mouth (ibid.). It should be noted that, while the cyclone (i.e. the rim depth eddy) spans the width of a narrow canyon, the cyclone produced in a wide canyon is attached to the upstream wall of the canyon (ibid.). While upwelling inside wide canyons also occurs along the downstream wall, the isopycnals are displaced higher inside narrow canyons (ibid.). Furthermore, the transport per unit width is larger in narrow canyons than in wide canyons (ibid).

The deformation radius $a = NH_c/f$ of Mackenzie Canyon is ~ 23.6 km, where N is the Brunt-Väisälä frequency and H_c is the depth of the canyon at the mouth, f is the Coriolis parameter, and the width W is 62 km. If the ratio between the canyon width W and radius of deformation a is used to define the dynamical width of a canyon, Mackenzie Canyon would be classified as a marginally wide (or intermediate) canyon (Carmack and Kulikov, 1998; Williams et al., 2006). The known details concerning the circulation patterns and upwelling in Mackenzie Canyon are summarized in Section 1.3.

1.3 Circulation and upwelling in the Beaufort Sea and Mackenzie Canyon

The Mackenzie Shelf (Figure 1.4) is in the southeastern Beaufort Sea and is bordered by the Mackenzie River delta to the south, Mackenzie Canyon to the west, and the Amundsen Gulf to the east (Carmack et al., 1989). The shelf is shallow (average depth of 35 m) and flat (average bottom slope of 10^{-4}), and it extends 530 km along the coast and 120 km offshore to the shelf break at 80 m depth (Carmack et al., 1989; Forest et al., 2007; Hill et al., 1991). The shelf bottom is mostly regular, with the exception of Mackenzie Canyon and Kugmallit Canyon (Carmack et al., 1989). Mackenzie Canyon is a U-shaped trough which incises the shelf nearly perpendicular to the coast and is topographically associated with

the Mackenzie River (Hill et al., 1991; Moors-Murphy, 2014). It is 98 km long (cross-shore or along-canyon direction), 62 km wide (along-shore or cross-canyon direction), and 372 m deep at the mouth. Given a depth-averaged buoyancy frequency $N \sim 8.7 \times 10^{-3}\,\mathrm{s}^{-1}$ (averaged between the ocean surface and 500 m depth from the salinity and temperature profiles used to define the stratification for the control experiments conducted in this study), the maximum depth of the canyon bottom $H_c = 372\,\mathrm{m}$, and a Coriolis parameter $f = 1.37 \times 10^{-4}\,\mathrm{s}^{-1}$, the canyon's radius of deformation is $a = NH_c/f \sim 23.6\,\mathrm{km}$, making Mackenzie Canyon a wide canyon.

The Canada Basin is characterized by a two-layer circulation system (Lique et al., 2015): the anticyclonic Beaufort Gyre at the surface, which is driven by the Beaufort atmospheric high-pressure system centred north of Alaska (Serreze and Barrett, 2011), and the cyclonic, topographically steered Beaufort shelf-break current (an extension of the Alaskan Coastal Current), which is 20 km wide and spans 150 m and 200 m depth over the Atlantic Water (Pickart, 2004). In Mackenzie Canyon, diurnal tidal currents are negligible ($<0.3\,\mathrm{cm\,s}^{-1}$) and semidiurnal tidal currents are relatively weak (for example, the M_2 tidal constituent which dominates semidiurnal tides in the region has maximum velocities $\sim 0.7\,\mathrm{cm\,s}^{-1}$ in Mackenzie Canyon compared to $\sim 6.5\,\mathrm{cm\,s}^{-1}$ in the Amundsen Gulf) (Kulikov et al., 2004). Additionally, the Mackenzie River plume extends offshore throughout Mackenzie Bay and is predominantly forced eastward along the Tuktoyaktuk Peninsula and into the Amundsen Gulf (Carmack and Macdonald, 2002; Dunton et al., 2006; Forest et al., 2007).

Six main water masses (Carmack et al., 1989; Lansard et al., 2012; Macdonald et al., 1989) can be identified in the southeastern Beaufort Sea: 1. Sea Ice Melt (SIM) 2. Meteoric Water (MW), 3. Winter Polar Mixed Layer (PML), 4. Upper Halocline Water (UHW), 5. Atlantic Water (AW), and 6. Canada Basin Deep Water (CBDW). The MW (Mackenzie River outflow and precipitation) has been detected in the upper 10 m (Lansard et al., 2012) to the upper 50 m (Williams et al., 2006) beyond the shelf break and along Mackenzie Canyon during periods of strong runoff from the Mackenzie River. The MW has a characteristic salinity of $0\,\mathrm{g\,kg}^{-1}$ and low nutrient concentrations. The UHW, which is derived from Pacific water that flows into the Arctic Ocean through the Bering Strait (Pickart, 2004), typically extends from 120 m to 180 m depth in the interior ocean, but it has also been found at 50 m depth along Mackenzie Canyon, potentially as a consequence of canyon upwelling (Williams and Carmack, 2008; Williams et al., 2006). It has a characteristic salinity of $33.26\,\mathrm{g\,kg}^{-1}$ (Macdonald et al., 1989) and high nutrient concentrations (Carmack et al., 2004; Macdonald et al., 1989). The AW, which is formed by

water entering the Arctic Ocean through the Fram Strait and Barents Sea, is found between 200 m and 800 m depth and has a characteristic salinity of 34.99 g kg^{-1} and relatively low nutrient concentrations (Macdonald et al., 1989).

Primary productivity in the southern Beaufort Sea is controlled by nutrient supply through riverine input and mixing and/or upwelling of deep waters and by light availability through ice cover (Macdonald et al., 1987). In the winter, nutrients in the inner shelf are supplied by the Mackenzie River and contain high nitrate, high silicate, and low phosphate levels (Macdonald et al., 1987). At this time, ice and snow cover inhibit light penetration, resulting in low primary productivity (Carmack et al., 2004). In the spring, while there are sufficient nutrients for primary production, light is still limited due to increased turbidity from river outflow and lingering ice (Carmack and Macdonald, 2002). Additionally, the water column becomes more stratified as a result of ice melt and river discharge, thereby preventing nutrient exchange between the nutrient-rich UHW and the photic zone (Carmack et al., 2004). Productivity increases in the summer, but it remains phosphate-limited over the inner shelf (onshore of the 20 m isobath) as these levels remain low while nitrate levels rise (Carmack et al., 2004). Over the middle (between the 20 m and 80 m isobaths) and outer shelf (beyond the 80 m isobath, which defines the shelf break), however, nitrate values are lower, indicating nitrate limitation (Carmack and Macdonald, 2002). In the autumn, stratification weakens due to reduced river outflow, sea ice formation, and increased wind-driven mixing. Overall, primary production in the southern Beaufort Sea is characteristic of oligotrophic waters (Carmack et al., 2004; Martin et al., 2010).

Canyon-driven upwelling in Mackenzie Canyon was first observed through the tilting of nitrate and density isolines (Macdonald et al., 1987). It was suggested that this upwelling signal plays a critical role in nutrient supply to the shelf given the low productivity typical of the Beaufort Sea (Macdonald et al., 1987). Since then, there have been two published, observational studies on the circulation and upwelling in Mackenzie Canyon, namely Williams et al. (2006) and Carmack and Kulikov (1998). Carmack and Kulikov (1998) uses temperature, salinity, and current observations from moorings deployed at stations SS1, SS2, SS3, and SS4 (Figure 1.4) between spring 1987 and spring 1988. Williams et al. (2006) uses temperature, salinity, and current observations from moorings deployed at stations A, B, C, and D (Figure 1.4) from August 1993 to September 1996 and Conductivity-Temperature-Depth (Williams et al., 2006, Figure 8) and Acoustic Doppler Current Profiler (Williams et al., 2006, Figure 9) data collected for along-canyon and cross-canyon transects in September 2002. The main findings of these

studies are outlined below.

Currents along the Mackenzie Shelf, as observed at stations B (Williams et al., 2006), SS3, and SS2 (Carmack and Kulikov, 1998), are strongly aligned in the along-shore direction and are topographically steered by the slope. In contrast, currents on the downstream slope, specifically at station A, do not show any preferential directionality. Along the upstream slope, upstream flows (towards the northeast) are generally stronger than downstream flows (towards the southwest) and show seasonal variability, with maximum velocities occurring in October and November (Williams et al., 2006). Additionally, unlike the circulation for narrow canyons, near-surface flows over Mackenzie canyon are deflected around the canyon head, indicating that the influence of this canyon extends to the surface (Williams et al., 2006).

Upwelling in Mackenzie Canyon is significantly correlated with easterly winds and southwestward currents (Carmack and Kulikov, 1998). Upwelling flows are observed at station C for downstream-directed currents at station B, but there is no correlation between flows at station C and station A (Williams et al., 2006). Furthermore, there is a stronger correlation between upwelling and mean daily wind stress compared to hourly wind stress, implying a stronger relationship to the cumulative effect of short but intense wind events (Carmack and Kulikov, 1998). In addition, ice motion during the winter has also been observed to produce upwelling (Williams et al., 2006). Time series for the vertical displacement of water masses, temperature anomaly, and alongshore velocity show that approximately 6-7 upwelling events occur in Mackenzie Canyon over the course of a year (Carmack and Kulikov, 1998; Williams et al., 2006), which is similar to the 9-10 upwelling events per year identified for the Beaufort Shelf west of Mackenzie Canyon (Pickart et al., 2013a).

During an upwelling event, isohalines in Mackenzie Canyon have been observed to tilt upwards towards the upstream side of the canyon and towards the head (Williams et al., 2006, Figure 8). After a series of easterly winds over the preceding weeks in the autumn, upwelling has been recorded to produce a maximum isopycnal displacement of 600 m, with water being displaced from a depth of 600 m to about 50 m (Carmack and Kulikov, 1998). Measurements at 200 m depth from station C and 90 m depth from station D show upwelling flows towards the canyon head (Williams et al., 2006). In fact, it has been suggested that even weaker upwelling events are likely to produce a flux of nitrates, for which the concentration peak lies between 100 m to 200 m depth, to the shelf (Williams et al., 2006). As upwelling relaxes, flows inside the canyon are directed offshore from the head to the mouth and travel along the isobaths on the upstream side of the canyon (Williams et al., 2006, Figure 9). Additionally,

eddy-like oscillations are observed not only for outgoing flows on the upstream side of the canyon, but also at station A on the downstream slope and at 100 m depth in the centre of the canyon near station C (Williams et al., 2006).

Notably, the upwelling signal initially observed in Mackenzie Canyon at station SS4 has been observed to propagate eastward along the shelf break (Carmack and Kulikov, 1998, Figure 12). It is suggested that, given the propagation speed, this disturbance is likely the first mode of an internal Kelvin wave (Carmack and Kulikov, 1998). Indeed, it has been shown that irregular bathymetric features, such as submarine canyons, can induce coastal trapped waves under upwelling-favourable wind conditions (Zhang and Lentz, 2017); however, the dynamics involved in this phenomenon require further attention.

Mackenzie Canyon is an interesting subject for the study of circulation patterns and upwelling dynamics inside wide canyons. While previous work on both narrow and wide canyons show that upwelling typically occurs on the downstream side of the canyon, observations in Mackenzie Canyon show the strongest upwelling occurring on the upstream side. The influence of a canyon also generally does not reach near-surface layers, while flows well above shelf break depth in Mackenzie Canyon region still display significant distortion due to the canyon. The upwelling signal propagating upstream of Mackenzie Canyon also offers the possibility to examine a relatively unstudied mechanism for upwelling around submarine canyons. With this context in mind, we define the scope of this thesis in the following section.

1.4   Research objectives

Understanding the oceanic processes that play a role in the recirculation of nutrients is critical, especially for oligotrophic regions such as the Arctic Ocean. Bathymetric features, such as submarine canyons, have been found to produce enhanced upwelling in coastal regions. Initiated by shelf currents flowing in the direction opposite to that of coastal trapped waves, upwelling in dynamically narrow canyons is driven by an unbalanced cross-shore pressure gradient over the canyon. Questions remain regarding the mechanisms driving upwelling in dynamically wide canyons. Using a numerical model, this study aims to simulate the circulation and upwelling inside Mackenzie Canyon during a wind-driven upwelling event and consider the implications for nutrient delivery to near-surface waters. Idealized and realistic models are used to investigate the various processes inside and near Mackenzie Canyon during the upwelling event. To evaluate the performance of the model, the simulated circulation and upwelling

patterns are compared to real-world observations. Owing to the dearth of studies on the upwelling dynamics in wide and realistic canyons, this study contributes to our understanding of the influence of canyon geometry and bathymetric details on canyon upwelling. Understanding the physical mechanisms involved in circulation and upwelling in Mackenzie Canyon supplements the current knowledge on the numerous interlinked processes supporting the complex ecological systems in the Beaufort Sea. Specifically, this study aims to answer the following research questions.

1. What are the circulation patterns inside and near Mackenzie Canyon during an upwelling event?

2. What flow features are significant modifiers of the upwelling in Mackenzie Canyon?

3. What differences in upwelling are caused by smoothing the topography to make an idealized canyon?

4. Are the model results for circulation and upwelling in Mackenzie Canyon supported by observational evidence?

5. Does upwelling in Mackenzie Canyon produce significant upward transport of nitrate across the nitracline depth and, if so, how much?
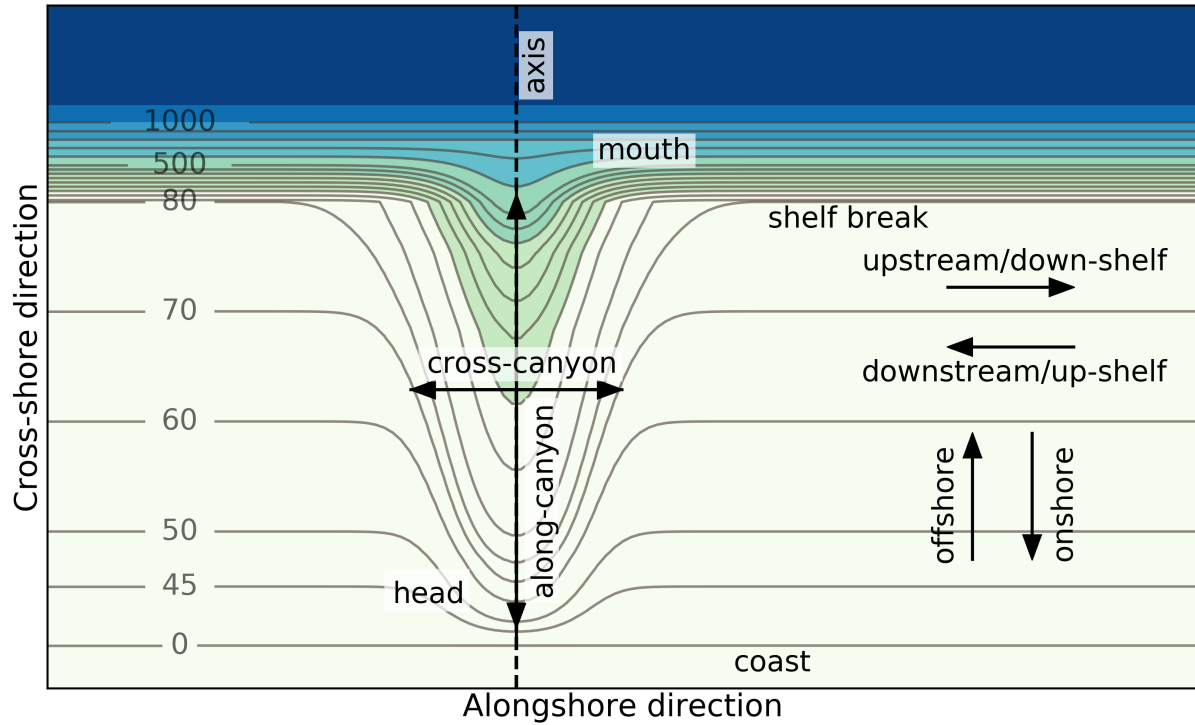
Figure 1.1: Plan view of idealized canyon bathymetry with definitions of the relevant directions of flow used in this study. The canyon bathymetry is coloured with light green colours indicating shallow depths and blue colours indicating deeper depths, and the isobaths are labelled in metres. The head, mouth, and axis of a canyon are typically used as references for the direction of flows in the region. Flows are considered to be upwelling-favourable if movement is in the downstream/up-shelf direction.
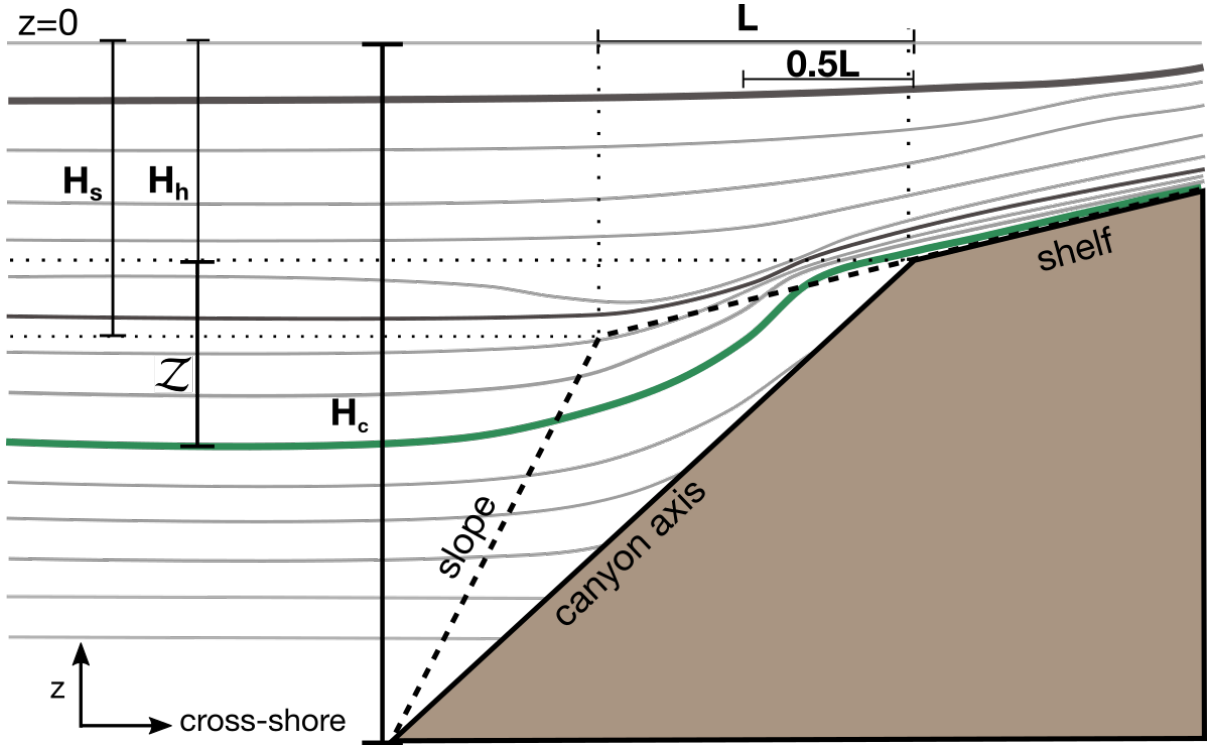
Figure 1.2: Cross-section along the axis of the canyon adapted from Ramos-Musalem and Allen (2019). The sketch shows upwelling isopycnals during a canyon-induced upwelling event and the relevant scales referred to in this thesis. The scales include the upwelling depth $\mathcal{Z}$, depth of the canyon head H_h, depth of the shelf break H_s, depth of the canyon at the mouth H_c, canyon length L, and z is the vertical coordinate. The deepest isopycnal to be upwelled is depicted by the bold, green line.
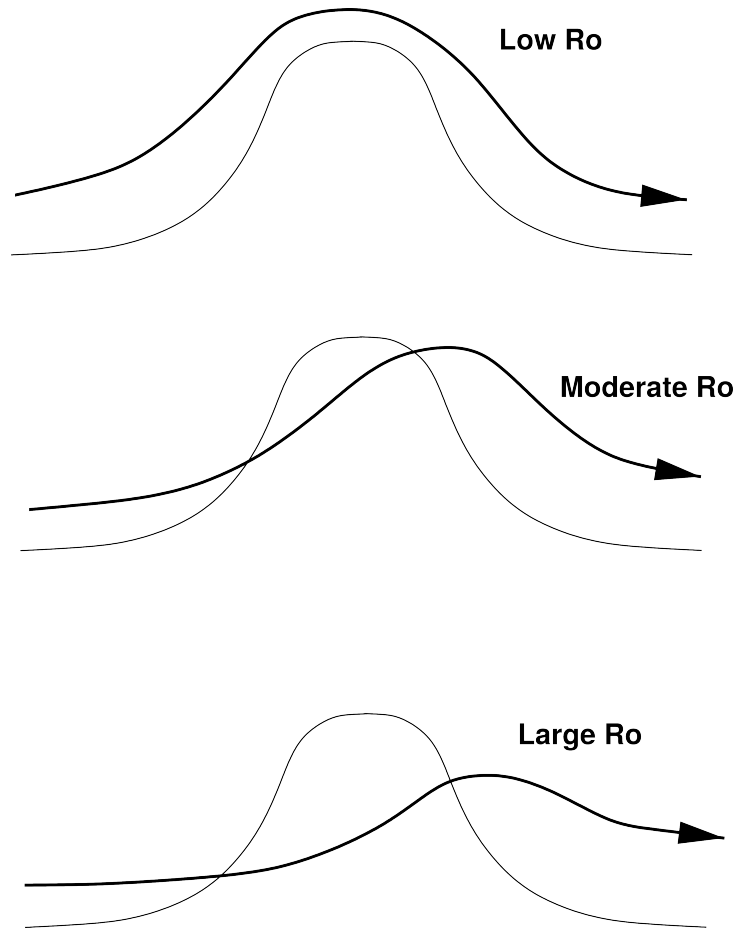
Figure 1.3: Plan view of flows over a canyon for small, moderate, and large Rossby numbers R_o (Allen, 2004, reprinted with permission of the author). This figure depicts the tendency for flows to either cross or follow the canyon topography depending on R_o (which can be defined using the turning radius of the shelf-break isobath on the upstream corner of the canyon $\mathcal{R}$ as in Allen (2004) or using the width of the canyon half-way along the canyon length $\mathcal{R}_W$ as in Howatt and Allen (2013)). The thin line represents the canyon rim, the thick line shows the flow path, and the arrow points in the direction of the flow.
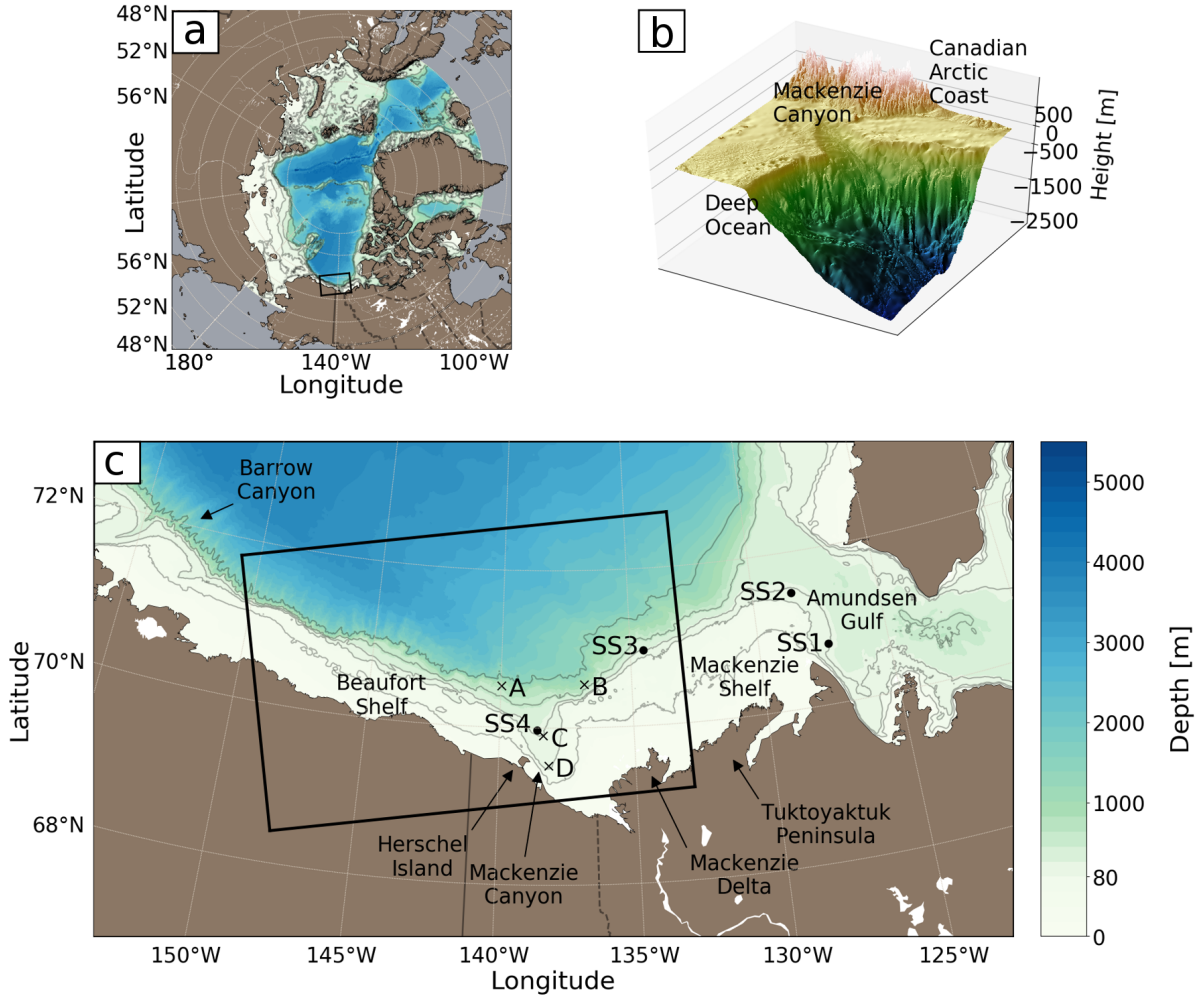
Figure 1.4: a) Bathymetry of the Arctic Ocean, b) 3-dimensional view of the bathymetry near Mackenzie Canyon, and c) local bathymetry of the southern Beaufort Sea. Panels (a) and (c) show the model domain used in this study outlined by the black rectangle. Panel (c) shows the mooring stations from past observational studies (Carmack and Kulikov, 1998; Williams et al., 2006).

Chapter 2

Methods

2.1 Model description

This study uses numerical simulations of circulation and upwelling in Mackenzie Canyon produced using a nested-grid modelling system. The modelling system is configured based on version 3.6 of the ocean component (OPA) (Madec et al., 1998) of the Nucleus for European Modelling of the Ocean (NEMO) (Madec, 2008) framework, and it uses the Adaptive Grid Refinement in Fortran (AGRIF) (Debreu et al., 2008) software to implement a nested grid. The NEMO ocean general circulation model solves the three-dimensional primitive equations (i.e. the Navier-Stokes equations under the Boussinesq and hydrostatic approximations) discretized on the Arakawa C-grid. The prognostic variables of the model are the three-dimensional velocity fields, sea surface height, conservative temperature, and absolute salinity. Furthermore, the AGRIF software is used to embed a high-resolution child model within a coarse-resolution parent model, the details of which are described below.

The coarse-resolution parent model encompasses the entire modelled region and employs a 2.26 km horizontal grid resolution and 120 s baroclinic time step. The high-resolution child model encompasses only the submarine canyon bathymetry (Figure 2.1). Implementing horizontal grid and temporal refinement by a factor of 3, the child model has a ~754 m horizontal grid resolution and 40 s baroclinic time step. The parent domain is arranged into $n_x = 270$ by $n_y = 174$ grid cells, extending 610 km and 393 km in the alongshore (x) and cross-shore (y) directions, respectively. The child domain is arranged into $n_x = 274$ by $n_y = 244$ grid cells, extending 207 km and 184 km in the alongshore (x) and cross-shore (y) directions, respectively. The full model domain covers an area extending from 150.8° W to 132.9° W

and from 68.4° N to 72.7° N (Figure 1.4). Given that the area of the Beaufort Sea is approximately $447\,000\,\mathrm{km}^2$ (Jakobsson, 2002), the parent and child model domains occupy 0.5 and 0.09 times the area of the Beaufort Sea, respectively. Both parent and child models have 80 vertical z-levels with a constant vertical resolution of 9 m between the surface and 500 m depth, increasingly coarser vertical resolution between 500 m and 790 m depth, and a constant 43 m vertical resolution from 790 m to a maximum depth of 1300 m. Partial z-levels are applied to allow the thickness of the bottom grid cells to vary for a more detailed representation of the bottom topography. The barotropic time step in both parent and child models is set to respect the Courant-Friedrichs-Lewy condition with a maximum Courant number of 0.5.

Numerical simulations were conducted using either realistic or idealized bathymetry (Figure 2.1; Table 2.1). The realistic bathymetry was extracted from a 500 m horizontal resolution, polar stereographic dataset of the International Bathymetric Chart of the Arctic Ocean (IBCAO) (Jakobsson et al., 2012), version 3.0, which is a compilation of bathymetric data for the Arctic region north of 64°N. The idealized bathymetry was constructed so as to closely resemble the realistic bathymetry. The idealized bathymetry features a simplified profile for the continental slope, a sloping continental shelf, and a secant-shaped submarine canyon with the approximate dimensions of Mackenzie Canyon (Figure 2.1 b.): length (cross-shore) $L = 98\,\mathrm{km}$, width (alongshore) $W = 62\,\mathrm{km}$, depth at the canyon mouth $H_c = 372\,\mathrm{m}$.

The AGRIF package (Debreu et al., 2008) is composed of a set of routines for adaptive mesh refinement and time integration of embedded grids (Berger and Oliger, 1984) over regions where complex dynamics require enhanced resolution for increased accuracy. The coupled NEMO-AGRIF model configuration was implemented using a set of pre-processing algorithms available at http://www.nemo-ocean. eu/Using-NEMO/SetupNewConfiguration/AGRIF-nesting-tool. In this study, the child and parent grids share a connection zone that has a width of 9 child grid cells in the realistic model and 3 child grid cells in the idealized model. This connection zone serves as both a "seam" over which the parent and child bathymetry are interpolated and a dynamical interface between parent and child models. The modelling system in this study uses two-way nesting (Debreu and Blayo, 2008; Debreu et al., 2012), which allows results from the parent model to serve as boundary conditions for the child model while updating the parent model with results from the child model at every parent time step. Additionally, a sponge layer with enhanced diffusivity ($100\,\mathrm{m}^2\,\mathrm{s}^{-1}$) and viscosity ($100\,\mathrm{m}^2\,\mathrm{s}^{-1}$) was applied at the boundaries of the

child model. Diffusivity and viscosity were set to $125\,\mathrm{m^2\,s^{-1}}$ in the parent model and $12.5\,\mathrm{m^2\,s^{-1}}$ in the child model for both realistic and idealized models.

The numerical simulations are forced with an easterly (westward) wind stress at the surface (Section 2.2), which induces a westward mean flow in the domain. In the parent model, the eastern (i.e. down-shelf/upstream) and western (i.e. up-shelf/downstream) boundaries are treated as periodic boundaries. To reduce dynamical inconsistencies between these two boundaries, the western side of the realistic model bathymetry was modified to match the bathymetry at the eastern boundary. Additionally, the realistic model domain was oriented at an angle (Figure 2.1) that allowed the coastline near the boundaries to be aligned parallel to the direction of the mean flow. At the northern (i.e. offshore) boundary, the model adopts Flather open boundary conditions (Flather, 1976) for barotropic velocities and sea surface height, Orlanski radiative open boundary conditions (Orlanski, 1976) for baroclinic velocities, and Neumann conditions for tracers. The Orlanski boundary conditions are used in conjunction with a sponge layer with a maximum viscosity of $500\,\mathrm{m^2\,s^{-1}}$ to dampen reflections from outgoing waves. Baroclinic and barotropic velocities are prescribed at the northern boundary from calculations for the Ekman and geostrophic currents produced by the given wind forcing. Sea surface height was also supplied at the northern boundary, and it was calculated using the solution (Section B.1) for the barotropic Rossby adjustment over a shelf (Allen, 1996).

At the solid lateral and bottom boundaries (i.e. the coastline and bottom topography), boundary conditions are set for the normal and tangential components of velocity. A masking array with elements set as 1 in the ocean and 0 elsewhere is used to define normal velocities at the solid boundaries as zero. The tangential component of velocity at the solid boundaries is managed by slip boundary conditions. The parent model uses partial slip boundary conditions, which allows for a dampened, non-zero tangential velocity, while the child model uses the free-slip condition, which implies no shear in tangential flows along the solid boundaries. A quadratic bottom friction parameterization with log-layer enhancement is used and initialized with a drag coefficient bounded by $C_D^{min} = 7.5 \times 10^{-3}$ and $C_D^{max} = 2$ and a bottom roughness length of $0.07\,\mathrm{m}$ in both parent and child models. The model was tested with the various built-in schemes for tracer advection available for the NEMO model (Madec, 2008). The Monotone Upstream Scheme for Conservation Laws (MUSCL) scheme was chosen for this study since it was the only scheme to not produce spurious salinity maxima in the simulations.

2.2 Model simulations

Seven numerical experiments were conducted for this study (Table 2.1). All simulations were initialized from rest with wind forcing at the surface for a run duration of 6 days. This run duration was chosen to avoid canyon-induced disturbances from propagating across the periodic boundaries and influencing the canyon circulation and upwelling in the later stages of the simulation (Figure C.1). Each simulation was run with a unique combination of bathymetry type (classified as idealized or realistic), strength of wind forcing (classified as base, half, or double), and stratification (classified as control or evaluation). This study mainly focuses on the results of the 6 simulations with the control stratification profile. The evaluation stratification case is used to evaluate model performance against observations.

The simulations are forced by wind stress at the surface with varying degrees of intensity. The forcing cases (base, half, and double) are defined by the strength of the wind event that induces upwelling in the modelled region (Figure 2.2 (a) and Table 2.2). Easterly (westward) winds were generated by modifying the analytical formulation for wind stress in the NEMO model code. The modified wind stress (Section B.2) is composed of a spatially constant but temporally variable alongshore component τ_x (Equation B.4) and zero cross-shore component τ_y (Table 2.2). The alongshore component τ_x features a strong wind pulse τ_x^{pulse} (Equation B.2) during the initial 25.5 hours of the simulation with a maximum wind stress value τ_{x-max}^{pulse} (Table 2.2). For the remainder of the run duration, τ_x features a reduced, constant wind stress τ_x^{relax} (Figure 2.2 (a) and Equation B.3) with a wind stress value of $\tau_{x-const}^{relax}$ (Table 2.2). The wind stress remains at a reduced, non-zero value until the end of the simulation in order to maintain alongshore flows in the domain at near-constant velocities, which support the quasi-steady stage of upwelling in the canyon.

The model stratification is set by using an observed vertical profile of temperature and salinity collected near Mackenzie Canyon (Figure 2.2 (c-e)). The stratification for the control experiments was derived from temperature and salinity measurements collected in August 2009 (dataset for 2009) by the Canadian research icebreaker CCGS Amundsen and made available by the Amundsen Science program, which was supported by the Canada Foundation for Innovation and Natural Sciences and Engineering Research Council of Canada, as well as by ArcticNet, a Network of Centres of Excellence of Canada (Rail et al., 2011). The stratification for the evaluation experiment (**RBE**) was derived from temperature and salinity measurements collected on a cruise in September 2015 on the American research vessel

RV Sikuliaq and funded by the National Science Foundation Division of Polar Programs. The temperature and salinity data was collected using shipboard and towed Conductivity-Temperature-Depth instruments, and the horizontal velocity data for currents was collected using a shipboard Acoustic Doppler Current Profiler. The observational data was provided by Amy Waterhouse through personal communication (Waterhouse, in prep), and readers are referred to Waterhouse et al. (2017) for details regarding data processing techniques that were also used to process the observational data collected in Mackenzie Canyon.

The performance of the model was evaluated by comparing observational data for horizontal velocity and salinity (Waterhouse, in prep) against model results for the simulation **RBE**, which uses the realistic bathymetry, base case of wind forcing, and the stratification near Mackenzie Canyon at the time when the observational data was collected. The comparisons between observations and model results are made specifically for **RBE** because the base case of wind forcing produces horizontal velocity magnitudes more similar to those in the observations compared to the other wind forcing cases. The model-observation comparisons presented in this study use observations collected over the course of three days (September 5-7, 2015) along two cross-canyon transects and one cross-shore transect at the downstream slope (Section 3.7). While this was a period of shifting winds, easterly winds dominated the first two days, likely causing the upwelling-favourable westward flows along topography.

2.3 Quantification of canyon upwelling

Canyon upwelling has been quantified by the upwelling depth in numerical and laboratory studies of idealized canyons (Allen, 2004; Allen and Hickey, 2010; Howatt and Allen, 2013; Jaramillo Uribe, 2005; Ramos-Musalem and Allen, 2019) and by the effective depth in observational studies of Mackenzie Canyon (Carmack and Kulikov, 1998; Williams et al., 2006). The upwelling depth is defined as the change in depth of the deepest isopycnal to be upwelled to the canyon rim at the head (Figure 1.2). The effective depth, as used to quantify upwelling in Mackenzie Canyon, is an estimate for the depth through which a water mass has been displaced given salinity measurements at a fixed location and depth in the upwelling region and a reference salinity profile. In the Beaufort Sea, the reference salinity profile is typically taken from an offshore location where water properties can be assumed to vary slowly. Salinity is the preferred property for estimating upwelling in the Arctic region since salinity is the primary determinant of density and salinity values typically increase monotonically with depth while temperature

values may not necessarily map onto a single depth.

In this study, canyon upwelling is quantified using a metric which we simply refer to as "vertical displacement". Similar to effective depth, vertical displacement is defined as the depth across which a water mass has been displaced during an upwelling event. In this case, however, the reference salinity profile used to estimate the original depth of a water mass is the initial salinity profile used at the start of the numerical simulation (Figure 2.2 (e)). Vertical displacement is expressed such that upward excursions of water via upwelling are represented by positive values.

This study considers the vertical displacement both at particular depths and on salinity surfaces representative of specific water masses. The salinity surfaces represent the Upper Halocline Water (UHW) and Atlantic Water (AW) water masses with characteristic salinities of $33.26\,\mathrm{g\,kg^{-1}}$ (Macdonald et al., 1989) and $34.99\,\mathrm{g\,kg^{-1}}$ (Macdonald et al., 1989), respectively. Given an initial salinity profile, these methods of visualization are beneficial in identifying areas of upwelling and downwelling and tracking the temporal and spatial evolution of these excursions.

2.4   Coastal trapped wave analysis

The model simulations show the generation and propagation of a coastal trapped wave (CTW) in Mackenzie Canyon. The wave signal has also been identified in observational studies documenting flow variability inside Mackenzie Canyon and along the Mackenzie Shelf (Carmack and Kulikov, 1998). The structure of this wave is investigated in this study using a model that searches for the free wave solutions of Boussinesq, hydrostatic, linearized CTWs along straight coastlines (Brink, 2018). The CTW model is packaged as Matlab software called Bigr∗.m available at the Woods Hole Oceanographic Institution website http://www.whoi.edu/page.do?pid=23361. The model calculates the dispersion curves and cross-shore vertical structures for pressure, along-shore and cross-shore velocities, vertical velocities, and density for wave modes possible under the specified conditions. To simulate the conditions used in the Mackenzie Canyon model, the CTW model was given the cross-shore profiles for the idealized bathymetry at the upstream side of domain away from the canyon. The CTW model also uses the same Coriolis parameter f and vertical profile for the Brunt-Väisälä buoyancy frequency squared N^2 as the Mackenzie Canyon model. The CTW model domain is discretized into 220 and 15 grid cells in the cross-shore and vertical directions, extending $280\,\mathrm{km}$ and $1300\,\mathrm{m}$, respectively. The boundaries are closed at the coast and open at the offshore edge of the domain. Wave solutions are sought in the

absence of a mean flow and with a nominal accuracy of 0.01% for the absolute value of frequency.

The wave parameters and the cross-shore structure of the vertical velocity of the coastal trapped wave observed in the Mackenzie Canyon model simulation (idealized bathymetry, base case for wind forcing) were compared to those calculated by the CTW model using the same idealized bathymetry. The alongshore propagation of the CTW in the Mackenzie Canyon model simulations was tracked between hours 24 and 36 using the vertical velocity signal averaged over all model depths to estimate the wave parameters. The wavenumber was calculated using the wavelength estimated as the distance between two consecutive crests of the simulated CTW. The frequency was calculated using the wave speed estimated using the alongshore distance travelled by the CTW between hours 24 and 36. The CTW model was then used to calculate the cross-shore structure of vertical velocity for a CTW with the wavenumber and frequency estimated for the CTW in the Mackenzie Canyon model simulations.

2.5 Calculations for model result analysis

A number of quantitative metrics were calculated using the model results to characterize the circulation and upwelling in Mackenzie Canyon and to compare the different simulation cases. These metrics are described below.

Relative vorticity

The vertical component of relative vorticity ζ is calculated as:

$$\zeta = \frac{\partial v}{\partial x} - \frac{\partial u}{\partial y} \tag{2.1}$$

where u and v are the horizontal components of velocity and x and y are the horizontal coordinates. For visualization purposes, the values for relative vorticity are normalized by the local Coriolis parameter $f = 1.37 \times 10^{-4}\,\mathrm{s}^{-1}$.

Nitrate transport

The nitrate advection in the modelled domain was estimated using the average relationship between salinity and nitrate concentration in the Mackenzie Canyon region. Geochemistry and salinity data from the Beaufort Gyre Exploration Project was obtained from the Woods Hole Oceanographic Insti-

tution website http://www.whoi.edu/page.do?pid=66521. Three stations inside and near the Mackenzie Canyon were chosen and data from September 2009 was considered. The mean relationship between salinity and nitrate concentration from this data is illustrated in Figure 2.2. To calculate the total nitrate transport in units of $\mathrm{mmol\,s^{-1}}$ in the region, the nitrate concentration in units of $\mathrm{mmol\,m^{-3}}$ is multiplied by the vertical velocity and horizontal area of each grid cell, and the product is then integrated over the canyon region defined by the child model domain.

Comparisons for wind forcing cases

Three metrics were defined to compare the response of the the flow near the canyon to the three wind forcing cases (base, half, double). The first metric describes the CTW amplitude and is defined as the mean positive vertical velocity on the slope just upstream of the canyon. The small area at the upstream slope over which the calculation was made was strategically chosen to avoid the effects of canyon upwelling on vertical velocities while still capturing the vertical velocities of the CTW as it propagates upstream along the slope. The second metric considers the maximum positive value of vertical displacement in the canyon region, thereby describing the strength of upwelling. The third metric is the total transport of nitrate in the canyon region. All metrics consider model results for the full simulation duration and all depth levels.

Simulation name	Bathymetry	Wind Forcing	Stratification
IBC	idealized	base	control
IHC	idealized	half	control
IDC	idealized	double	control
RBC	realistic	base	control
RHC	realistic	half	control
RDC	realistic	double	control
RBE	realistic	base	evaluation

Table 2.1: Bathymetry, wind forcing, and stratification cases for all simulations.

Wind forcing case	τ_{x-max}^{pulse} [N m^{-2}]	$\tau_{x-const}^{relax}$ [N m^{-2}]	τ_y [N m^{-2}]
Base	-0.8	-0.1	0
Half	-0.4	-0.05	0
Double	-1.6	-0.2	0

Table 2.2: Values for the maximum alongshore wind stress τ_{x-max}^{pulse}, reduced alongshore wind stress $\tau_{x-const}^{relax}$, and cross-shore wind stress τ_y for all wind forcing cases.
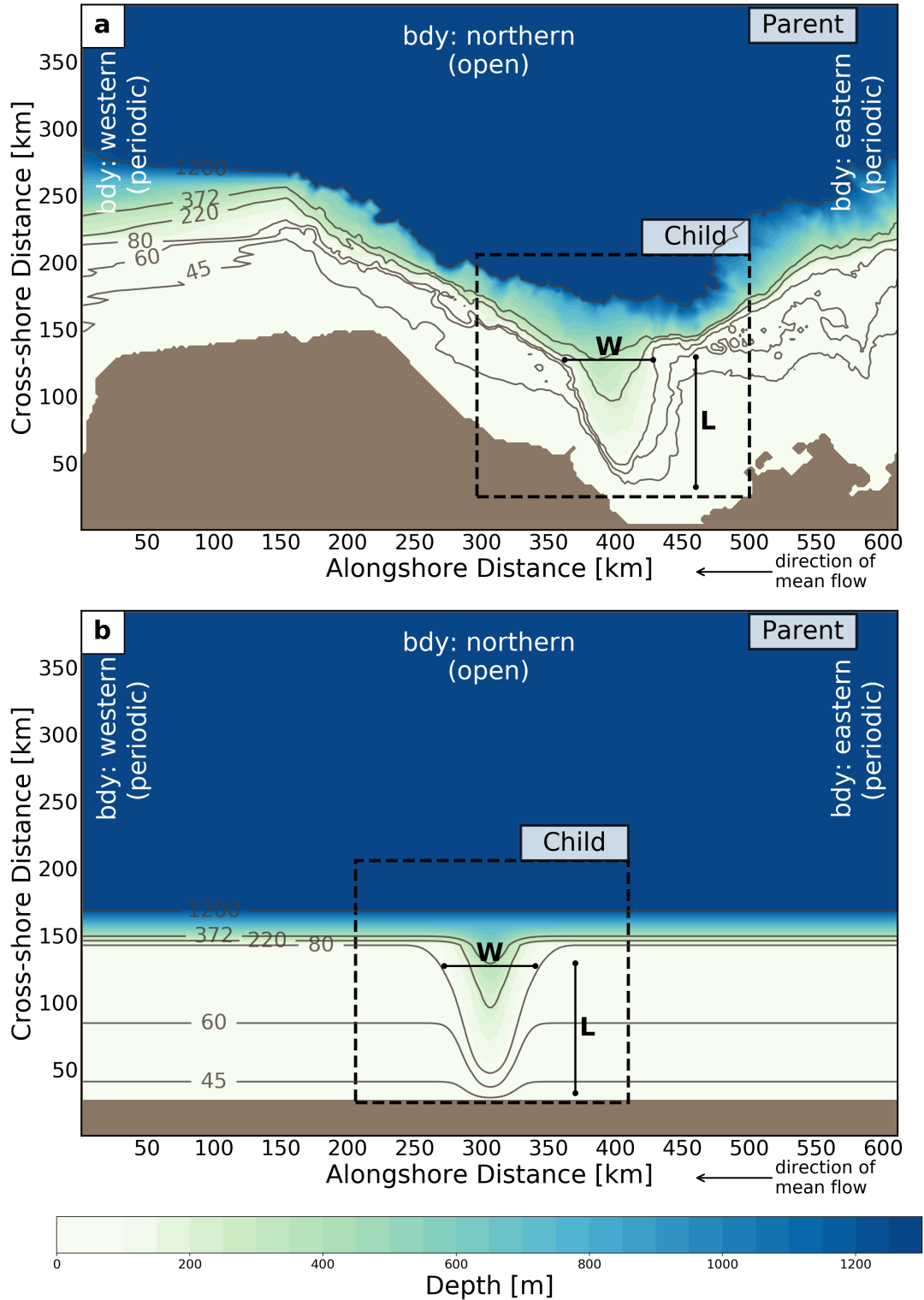
Figure 2.1: a) Realistic and b) idealized model domain and bathymetry. The parent model extends across the full model domain, and the child model covers the area outlined by the dashed-line rectangle over the canyon bathymetry. The dimensions for canyon width and length are identified by the dark, black lines, and the three open boundaries are labelled according to the corresponding boundary conditions. The direction of mean flow in the model domain is indicated by the upshelf-directed arrow.
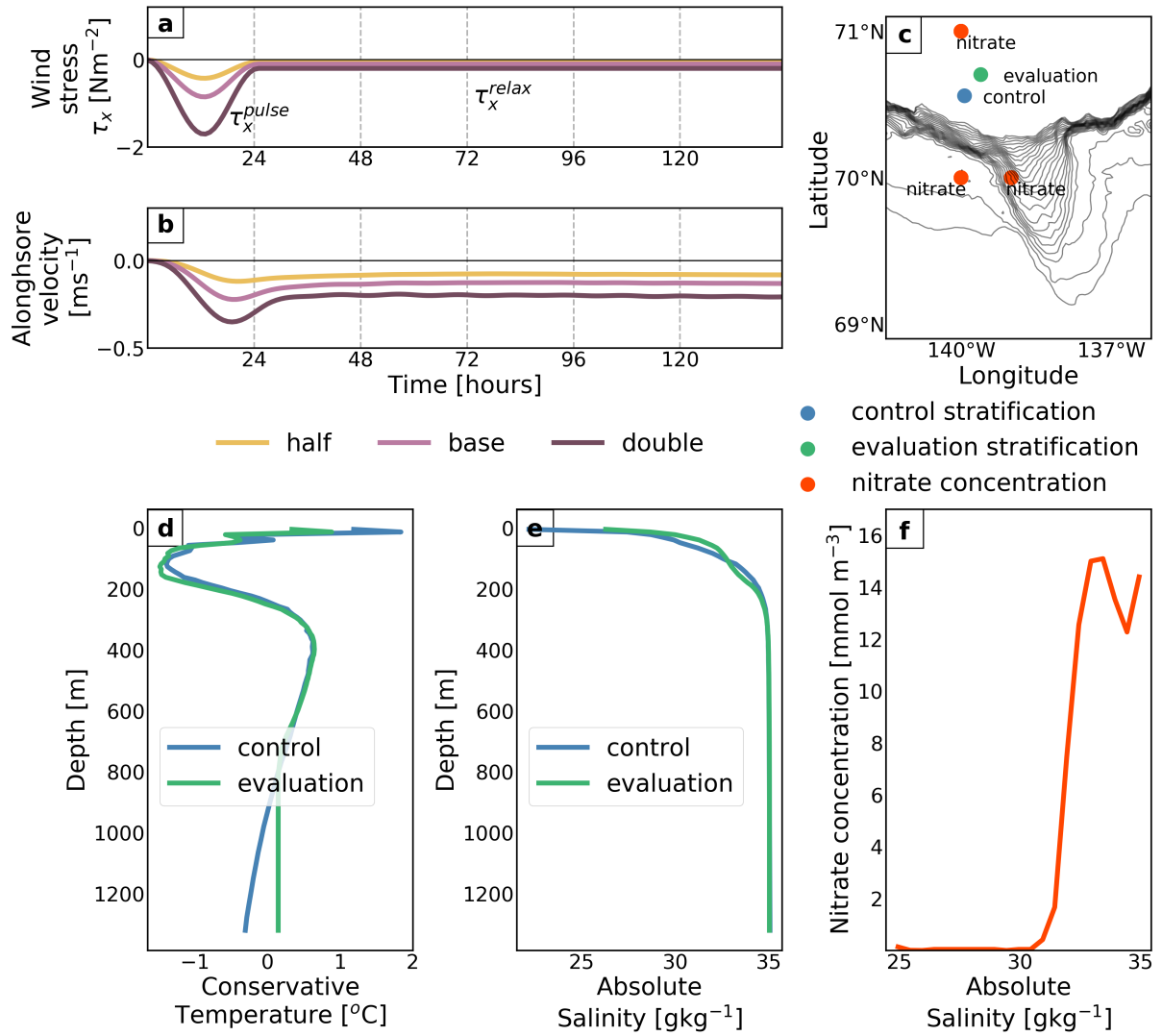
Figure 2.2: a) Alongshore wind stress τ_x and b) the resulting, alongshore velocity component of incoming shelf currents for all wind forcing cases (half, base, double). c) Realistic canyon bathymetry and stations where observation data was collected for stratification and nitrate concentration. Depth profiles for d) temperature and e) salinity used as initial conditions for the control and evaluation model runs. f) Relationship between salinity and nitrate concentration.

Chapter 3

Results

3.1 Circulation patterns influenced by topographic steering

The influence of Mackenzie Canyon on local circulation patterns is examined by tracking the evolution of horizontal and vertical flows on salinity surfaces representing two water masses, namely the Upper Halocline Water (UHW) and the Atlantic Water (AW), which have depths of 119 m and 470 m, respectively, throughout the domain when the simulation is initialized from rest. The flow patterns at depths cut by the canyon topography (between 40 m and 372 m) are largely represented by the horizontal and vertical flows on the UHW-representative surface (Figures 3.1–3.4). The few key differences in circulation at greater depths within the canyon topography are reviewed by considering flows on the AW-representative surface (Figures 3.5–3.8 and Section 3.2), especially in regards to the propagation of the coastal trapped wave (Figure 3.9).

Generally, flows in Mackenzie Canyon are steered by and around the canyon topography. During the time-dependent stage of upwelling, which occurs within the initial 36 hours of the simulation (Figures 3.1 and 3.2 (g)), high-speed alongslope currents ($\sim$0.57 m s^{-1}) slightly overshoot the upstream corner of the canyon mouth and move towards the canyon head and downstream wall (Figures 3.1 and 3.2(a)). Flows along the upstream wall reach the canyon head with high speeds ($\sim$0.25 m s^{-1}), while flows farther downstream inside the canyon reach the downstream wall with lower speeds ($\sim$0.05 m s^{-1}). Near the mid-length of the canyon along the downstream wall, low-speed flows turn offshore and exit the canyon on the downstream side of the canyon mouth. At the downstream corner of the mouth, outgoing flows slightly separate from the topography before turning westward, parallel to the downstream

slope.

The rest of the simulation represents the quasi-steady stage of upwelling since the alongshore velocity of the incoming shelf flows is near-constant (Figures 3.1 and 3.2 (g)). Two distinct circulation features related to the canyon topography develop during the advection-driven stage of upwelling. The first feature is a high-speed onshore jet that moves along the upstream wall from the mouth to the head of the canyon (Figures 3.1 and 3.2 (b-c)). At the canyon head, high-speed flows from the jet encounter the topography, and the water mass experiences a strong upward excursion (Figures 3.3 and 3.4 (d-f) and Section 3.4). The UHW-representative surface extends farther onshore as it is upwelled, and flows closest to the shore are redirected westward (Section 3.2). Concurrently, flows inside the canyon continue to turn offshore along the downstream wall and exit the canyon on the downstream side of the mouth.

The second circulation feature that develops during the advection-driven stage of upwelling is a region of strong cyclonic vorticity on the upstream corner of the canyon mouth in both idealized and realistic models (Figures 3.1 and 3.2 (d-f)). This vorticity anomaly evolves into a closed cyclonic eddy more readily in the realistic simulations than in the idealized simulations (Figure 3.2 (d-f)). Throughout the simulation, the flow separation at the upstream side of the canyon mouth gradually increases (Figures 3.1 and 3.2 (a-c)) and allows for strong cyclonic vorticity to develop at this location (Figures 3.1 and 3.2 (d-f)). The highest speeds on the UHW-representative surface always occur near the upstream corner of the canyon mouth where incoming flows turn into the canyon (Figures 3.1 and 3.2 (a-c)). These speeds are higher in the idealized model ($\sim 0.7 \, \mathrm{m\,s^{-1}}$) than in the realistic model ($\sim 0.5 \, \mathrm{m\,s^{-1}}$). The average magnitude for relative vorticity on the upstream side of the canyon mouth, whether positive or negative, is higher in the idealized model ($4 \times 10^{-4} \, \mathrm{s^{-1}}$ and $-1 \times 10^{-4} \, \mathrm{s^{-1}}$) than in the realistic model ($3 \times 10^{-4} \, \mathrm{s^{-1}}$ and $-8 \times 10^{-5} \, \mathrm{s^{-1}}$). The formation of a closed cyclonic eddy thus appears to be dependent on the interaction between incoming flows and the shape of the topography at the upstream corner of the canyon mouth. Reminiscent of rotational flows around headlands, the incoming currents along the upstream slope separate from the topography at the upstream corner of the canyon mouth, resulting in the generation of high vorticity flows and the subsequent formation of a cyclonic eddy on the lee side of the topography, especially in the realistic bathymetry case which resembles a sharp cape.

32

3.2 Circulation patterns influenced by coastal trapped wave propagation

In addition to being influenced by topographic steering, the circulation patterns near Mackenzie Canyon are also influenced by the generation and propagation of a coastal trapped wave. This wave feature, which is most clearly seen in the vertical velocity results, is induced by the interaction of the alongshore flows with the canyon topography. The CTW is generated on the downstream side of the canyon mouth within the first day of the simulation (Figure 3.10), and it propagates in the upstream direction around the canyon topography (Figure 3.9 (e-h)) and along the upstream slope (Figure 3.9 (a-d)). The CTW is bottom-intensified, exhibiting a stronger vertical velocity signal on the AW-representative surface (Figures 3.7 and 3.8 (a-c)) compared to the UHW-representative surface (Figures 3.3 and 3.4 (a-c)). Throughout the simulation, the CTW is scattered by the bathymetry, especially in the realistic model (Figures 3.4 and 3.8 (c)). On the UHW-representative surface, the signal has mostly degenerated as a consequence of this scattering by the end of day 2 in the realistic model and by the end of day 4 in the idealized model (Figure 3.10). On the AW-representative surface, the signal in the idealized model is more persistent and reaches the eastern edge of the domain by the end of day 4 (Figure C.1), whereas the signal in the realistic model has significantly dissipated before reaching the edge of the domain (not shown).

The horizontal velocity field on both UHW- and AW-representative surfaces is affected by the passage of the CTW along the canyon and slope topography. Anticyclonic and cyclonic vorticity develops at the CTW wave nodes leading troughs and crests, respectively (Figure 3.9 (i-l), Figure 3.10). Given that both the size of the canyon topography and the strength of the propagating wave signal differ between the UHW- and AW-representative surfaces, the influence of the CTW on the circulation for each surface is described separately.

On the UHW-representative surface, incoming currents induce a region of positive vertical velocities (upwelling) at the downstream side of the canyon head during the initial stage of the upwelling event (Figures 3.3 and 3.4 (a)). Throughout the simulation, strong upward currents persist at the downstream side and centre of the canyon head (Figures 3.3 and 3.4 (b-c)). The generation of the CTW is evident at $\sim$ hour 18 of the simulation by a region of negative vertical velocities (representing the wave trough) extending from the mouth to the mid-length of the canyon along the downstream wall (Figure 3.10 (a,

d)). As this signal propagates towards the head, the wavelength of the CTW decreases. By the second day of the simulation, multiple wave troughs and crests can be observed along the downstream wall of the canyon (Figure 3.9 (i, k), Figure 3.10 (b, e)). The CTW signal is mostly suppressed along the upstream wall of the canyon by the strong onshore jet (Figure 3.9 (e, g)), and only a weak signal can be observed propagating along the upstream slope outside of the canyon (Figure 3.9 (a, c)).

During the first two days of the simulation, before the CTW has been significantly scattered, strong vorticity is generated at the nodes of the wave. For the UHW-representative surface in the idealized model, an anticyclonic eddy forms near the canyon head and cyclonic vorticity develops near the mid-length of the canyon (Figure 3.9 (i), Figure 3.10 (a-b)). The CTW-induced anticylonic eddy interacts with the onshore jet to support onshore and westward flows at the canyon head. Concurrently, the CTW-induced cyclonic vorticity near the mid-length of the canyon contributes to the steering of outgoing flows. The generation of vorticity at the wave nodes is much less pronounced in the realistic model due to higher levels of wave scattering (Figure 3.9 (k), Figure 3.10 (d-e)).

On the AW-representative surface, the CTW signal has a stronger influence than topographic steering on the local circulation since the size of the canyon is much smaller at the depths occupied by this water mass. In both idealized and realistic model simulations, incoming currents flow around the canyon topography during the first day of the simulation (Figures 3.5 and 3.6 (a)), similar to currents on the UHW-representative surface. At the same time, the CTW propagates upstream along the canyon walls and exits the canyon on the upstream side of the mouth (Figure 3.7 (a), Figure C.3). During the second and third days of the simulation, the structure of the CTW is modified (Section 3.3), likely as a consequence of the difference in bottom slope within the canyon topography compared to that offshore of the canyon and along the upstream slope. As the CTW propagates along the topography in both idealized and realistic models, it distorts the horizontal velocity field and induces an eddy at the wave node which travels upstream with the CTW (Figure 3.9 (j, l)). After the third day of the simulation, the wave signal has degenerated and no longer produces pronounced distortions in the horizontal velocity field (Figure 3.10 (c, f)).

3.3 Coastal trapped wave characterization

The propagation of the CTW in the Mackenzie Canyon model simulation was tracked from hour 24 to hour 36 using the depth-averaged vertical velocity signal to estimate the wave parameters (Figure 3.11

(a), Section 2.4). The wavelength, wavenumber, speed, and frequency of the CTW estimated from the Mackenzie Canyon model results are 81 km, 7.8×10^{-5} rad m^{-1}, 0.78 m s^{-1}, and 6.1×10^{-5} rad s^{-1} (Figure 3.11 (c)), respectively. The modal structure of a wave with the approximate frequency and wavenumber estimated from the Mackenzie Canyon model simulation was calculated using the CTW model (Brink, 2018). The wavelength, wavenumber, speed, and frequency calculated by the CTW model are 81 km, 7.8×10^{-5} rad m^{-1}, 0.77 m s^{-1}, and 6.0×10^{-5} rad s^{-1} (Figure 3.11 (c)), respectively. The cross-shore structure for vertical velocity of the wave in the Mackenzie Canyon model results (Figure 3.11 (b)) is well represented by that of the lowest wave mode computed by the CTW model (Figure 3.11 (d)). However, a few differences in the wave structure for vertical velocity do exist between the results of the Mackenzie Canyon model and CTW model, such as a band of negative velocity approximately 250 km offshore (Figure 3.11 (b)). Further work using the CTW model could investigate the contribution of higher wave modes in producing the more complex cross-shore structure for vertical velocity observed in the Mackenzie Canyon model simulations, especially as the wave structure is modified and becomes more complex throughout the simulation (Figure C.5). Overall, the results of the CTW model for the lowest wave mode can be used to understand the general structure of the CTW in the Mackenzie Canyon model results.

The dispersion curve and cross-shore structure of the lowest wave mode calculated by the CTW model are used to determine if the CTW exhibits gravity wave characteristics, as would be the case for Kelvin waves, or topographic Rossby wave characteristics, as would be the case for shelf waves. The CTW in the Mackenzie Canyon model results can be characterized as a shelf wave. Shelf waves are right-bounded coastal trapped waves which require both rotation and depth variations along the shelf. The dispersion curve of a shelf wave shows that frequency increases monotonically for small wave numbers, and the group speed tends to zero for high wavenumbers (Mysak, 1980). The dispersion curve calculated by the CTW model (Figure 3.11 (c)) is, therefore, consistent with that of a shelf wave. Furthermore, the modal structure calculated by the CTW model shows that alongshore and cross-shore velocity components have similar magnitudes (Figure C.4), which is also consistent with the structure of a shelf wave as opposed to that of a Kelvin wave. Finally, the ratio of the wave kinetic and potential energies, which is also provided by the CTW model, could be used as a diagnostic of whether the nature of a wave is more similar to that of a Kelvin wave or a shelf wave (Brink, 1982). The energy ratio for the CTW is 1.1, which indicates that the CTW could exhibit attributes of both Kelvin and shelf waves.

Given the dispersion curve and modal structure of the wave, however, the nature of the CTW appears to be more similar to that of a shelf wave. Further work is required to definitely determine the nature of this CTW and build a comprehensive understanding of its dynamics. Altogether, the characterization of the CTW observed in the Mackenzie Canyon model results supports future investigation regarding the influence the CTW on the propagation of the upwelling signal observed along the Mackenzie Shelf after an upwelling event.

The structure of the CTW in the Mackenzie model simulations is modified as it propagates along the canyon walls and, eventually, along the upstream slope. The evolution of the wave is examined further using the AW-representative surface in the idealized model since the amplitude of the wave is larger at greater depths (and, therefore, the signal is more distinct) and scattering is considerably lower than that in the realistic model. The average phase speed of the CTW throughout the simulation is estimated from the Hovmöller diagrams showing the wave signal inside (Figure 3.9 (f)) and offshore of (Figure 3.9 (b)) the canyon. The average phase speed of the CTW is $\sim 0.14\,\mathrm{m\,s}^{-1}$ inside the canyon topography (i.e. along Section B) and $0.49\,\mathrm{m\,s}^{-1}$ offshore of the canyon (i.e. along Section A). Further work using the CTW model (Brink, 2018) is required to examine changes to the wave characteristics as a consequence of differences in bottom slope between the canyon and upstream slope.

3.4 Distribution and propagation of the canyon upwelling signal

Mackenzie Canyon shows enhanced upwelling compared to the adjacent shelf and slope. The strongest upwelling induced by the canyon displaces water upward by 175 m in the idealized model and 248 m in the realistic model compared to less than 40 m on the downstream slope away from the canyon in the idealized and realistic models (Figures 3.12 and 3.13). The spatial distribution of upwelling in Mackenzie Canyon is influenced by the interaction between the onshore jet and the canyon topography, the cyclonic eddy on the upstream side of the canyon mouth, and the propagation of the CTW along the canyon walls and upstream slope.

The UHW-representative surface in the idealized model (Figure 3.3 (d-f)) demonstrates the influence of the onshore jet, upstream cyclonic eddy, and CTW on upwelling. During the initial, time-dependent stage of upwelling, the strongest upward displacement occurs near the head and along the downstream wall of the canyon. Flows turning into the canyon travel to the head and downstream wall of the canyon (Figure 3.1 (a)), resulting in upward excursions as this water encounters the topography. During the

quasi-steady stage of upwelling, however, the strongest upwelling occurs near the head and along the upstream wall of the canyon. At the head, the onshore jet reaches the topography with high speeds (Figure 3.1 (b-c)), generating upwelling that extends the coverage of the water mass farther onshore. Upwelled flows at the head are directed downstream by a combination of topographic steering and the influence of the anticyclonic eddy induced by the CTW (Figure 3.9 (i)). Additionally, the strong upwelling observed along the upstream wall is likely a consequence of the upwelling signal propagating along the canyon walls with the CTW (Figure 3.3 (a-c)). Notably, the strongest upwelling along the upstream wall occurs in the region of high cyclonic vorticity (Figure 3.1 (d-f)). The influence of the upstream cyclonic eddy on upwelling is more apparent in the realistic model, as described below.

The UHW-representative surface in the realistic model shows the the influence of the shape of the topography on the distribution of upwelling throughout the canyon. Topographic steering around the canyon walls is relatively unaffected by the propagation of a CTW (Figure 3.2 (a-c)) in the realistic model, resulting in an upwelling signal that is mostly balanced around the canyon walls (Figure 3.4 (d-f)). Generally, the spatial distribution of upwelling and the values for vertical displacement are comparable between the upstream and downstream sides of the canyon, with two exceptions. First, the water mass exhibits strong upwelling at the centre and downstream side of the canyon head (Figure 3.4 (d-f)), which is induced by onshore flows inside the canyon flowing over the topography instead of turning in the offshore direction to exit the canyon (Figure 3.2 (a-c)). Second, the strongest upwelling along the upstream wall is centred over the closed cyclonic eddy nestled on the lee side of the topography at canyon mouth (Figure 3.4 (a-c)). Notably, the region of strong upwelling expands as the cyclonic eddy widens throughout the simulation (Figure 3.2 (d-f)).

In both idealized and realistic models, the upwelling signal on the AW-representative surface propagates along the slope topography with the CTW (Figures 3.7 and 3.8 (d-f)). The strongest upwelling occurs immediately adjacent to the slope topography, and some downwelling occurs farther offshore. Notably, downwelling coincides with regions with cyclonic vorticity, including the cyclonic eddy induced by the CTW (Figure 3.9 (j, l)). This is in stark contrast with the strong upwelling observed at the cyclonic eddy generated by flow separation on the UHW-representative surface (Figures 3.3 and 3.4 (d-f)).

Upwelling at specific depths shows the main features observed on the UHW- and AW-representative surface (Figures 3.12 and 3.13). The strongest upwelling is initially focused at the canyon head and

37

downstream wall, but it shifts toward the upstream wall, especially around the cyclonic eddy at the upstream side of the mouth, throughout the simulation. As expected, the upwelling signal is stronger along the upstream slope at greater depths due to the propagation of the CTW. Additionally, strong upwelling is also evident near the surface (Figures 3.12 and 3.13 (a-c)). Throughout the simulation, upwelling is typically stronger at greater depths and occurs within the initial 2.5 days of the upwelling event (Figures 3.12 and 3.13 (f)).

3.5   Nitrate transport across the nitracline depth

In the Beaufort Sea, the nitracline occurs at $\sim 50\,\mathrm{m}$ depth (Ardyna et al., 2017; Monier et al., 2015). In this study, the nitrate transport across this depth (henceforth referred to as the nitracline depth) is estimated using both nitrate concentrations and vertical velocities at this depth ($\sim 50\,\mathrm{m}$). The highest values, whether positive or negative, of nitrate transport either occur within the canyon topography at the nitracline depth or show the influence of the topography at greater depths. In the idealized model (Figure 3.14 (a-c)), upward transport occurs at the canyon head and downward transport occurs over the downstream wall of the canyon. In the realistic model (Figure 3.14 (d-f)), upward transport mostly occurs along the downstream wall of the canyon and covers a smaller region compared to the idealized model.

Throughout the simulation, the nitrate transport integrated over the child domain is positive, indicating canyon-induced upwelling of nitrate across the nitracline depth (Figure 3.14 (g)). The time series for total nitrate transport (Figure 3.14 (g)) shows a sharp increase just after the peak in wind stress is applied at the surface and around the same time as the maximum alongshore velocities of shelf currents. For the remainder of the simulation, the total transport remains fairly steady at a reduced value. Notably, even though the idealized model shows higher downward transport than the realistic model, it also produces upward transport over a larger area (Figure 3.14 (a, d)), resulting in overall higher upward transport throughout the simulation (Figure 3.14 (g)).

During the initial 36 hours of the simulation, when the strongest transport is observed, the total transport across the nitracline depth is $1.65 \times 10^8\,\mathrm{mmol\,s^{-1}}$ in the idealized model and $1.02 \times 10^8\,\mathrm{mmol\,s^{-1}}$. Additionally, the maximum transport estimated for any given hour during the initial 36 hours of the simulation is $1.11 \times 10^7\,\mathrm{mmol\,s^{-1}}$ in the idealized model and $7.59 \times 10^6\,\mathrm{mmol\,s^{-1}}$ in the realistic model.

3.6 Effects of wind forcing on circulation and upwelling

The response of Mackenzie Canyon to wind forcing was examined by comparing metrics representing key features in the canyon across the three wind forcing cases ('half', 'base', and 'double'). It is important to note that these metrics have been normalized relative to the respective 'base' case. Therefore, linear processes are considered to be dominant for a given metric if the response of the canyon is represented by a 2:1 ratio between **base:half** and/or **double:base** wind cases.

For all metrics (Figures 3.15–3.17), the ratio between the base and half cases is approximately 2:1, indicating a linear response of the canyon to wind forcing. Non-linear processes, however, appear to take a more dominant role with increasing wind forcing given that the ratio between the double and base cases is not precisely 2:1 for any of the features represented. The effect of increased wind forcing is especially pronounced for processes contributing to the estimate for CTW amplitude in the realistic model (Figure 3.15). A closer look at the model results (Figures 3.4 and 3.8) shows small, isolated regions of anomalous vertical velocities in areas with high bottom roughness along the upstream slope in the realistic model that do not appear to correspond with the CTW propagation. Unlike vertical displacement (Figure 3.16), nitrate transport (Figure 3.17) shows a distinct deviation from linearity due in part to the non-linear relationship between salinity and nitrate concentration (Figure 2.2 (f)).

3.7 Model evaluation

The model's ability to reproduce key circulation features and upwelling patterns in Mackenzie Canyon was evaluated by conducting a simulation using realistic bathymetry and a stratification profile collected near the canyon (i.e. model run **RBE**). This study benefitted from access to observational data (Waterhouse, in prep) for currents, salinity, temperature, and winds in Mackenzie Canyon. The model results show remarkable qualitative agreement with both current (Figure 3.18) and salinity (Figure 3.19) observations. The general circulation inside the canyon and cyclonic eddy feature on the upstream side of the canyon mouth are well represented in both model results and observations. The model appears to underestimate the velocities of the high-speed jet separating from the topography on the upstream side of the canyon (as represented by the length of the arrows in Figure 3.18), indicating that future work should consider intentionally adjusting the wind stress applied to the surface in order to reproduce matching velocities for the incoming along-slope flows for evaluation simulations. Salinity

measurements in the canyon show that the model reproduces the site of upwelled, high-salinity water on the upstream side of the canyon. The observational data also corroborates the unexpected finding that upwelling is stronger on the upstream side of the canyon compared to the downstream side.
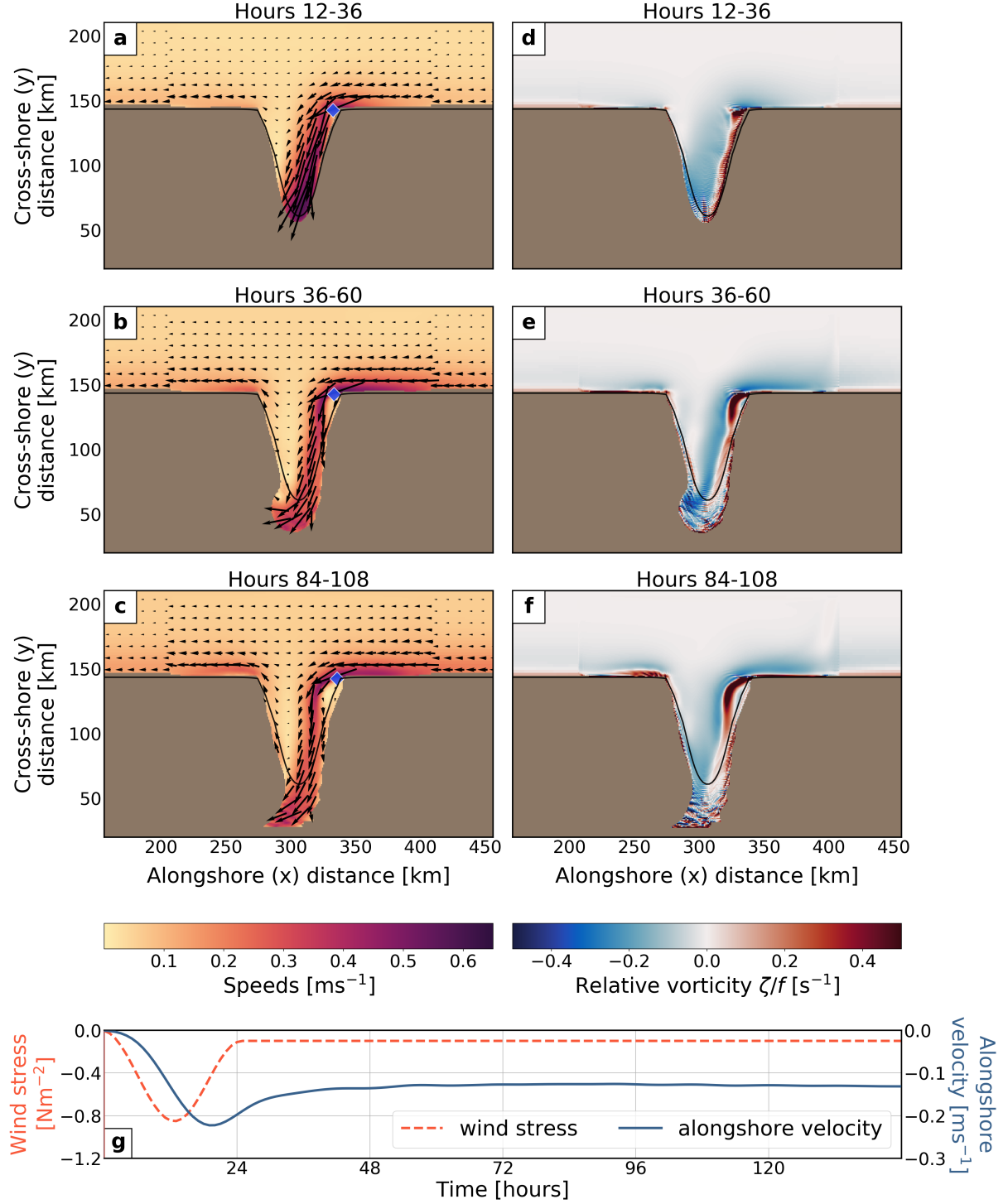
Figure 3.1: Characterization of the horizontal circulation on the UHW-representative surface in the idealized model: Plan views of a-c) flow speed and direction [m s^{-1}] and d-f) relative vorticity [s^{-1}] averaged over three separate days (top row: hours 12-36, middle row: hours 36-60, bottom row: hours 84-108); g) time series of wind stress and average alongshore velocity of incoming currents over the upstream side of the shelf. The blue diamond in plan views (a-c) shows the location of maximum speeds. The solid, black line outlines the canyon bathymetry at the initial depth of the UHW-representative surface.
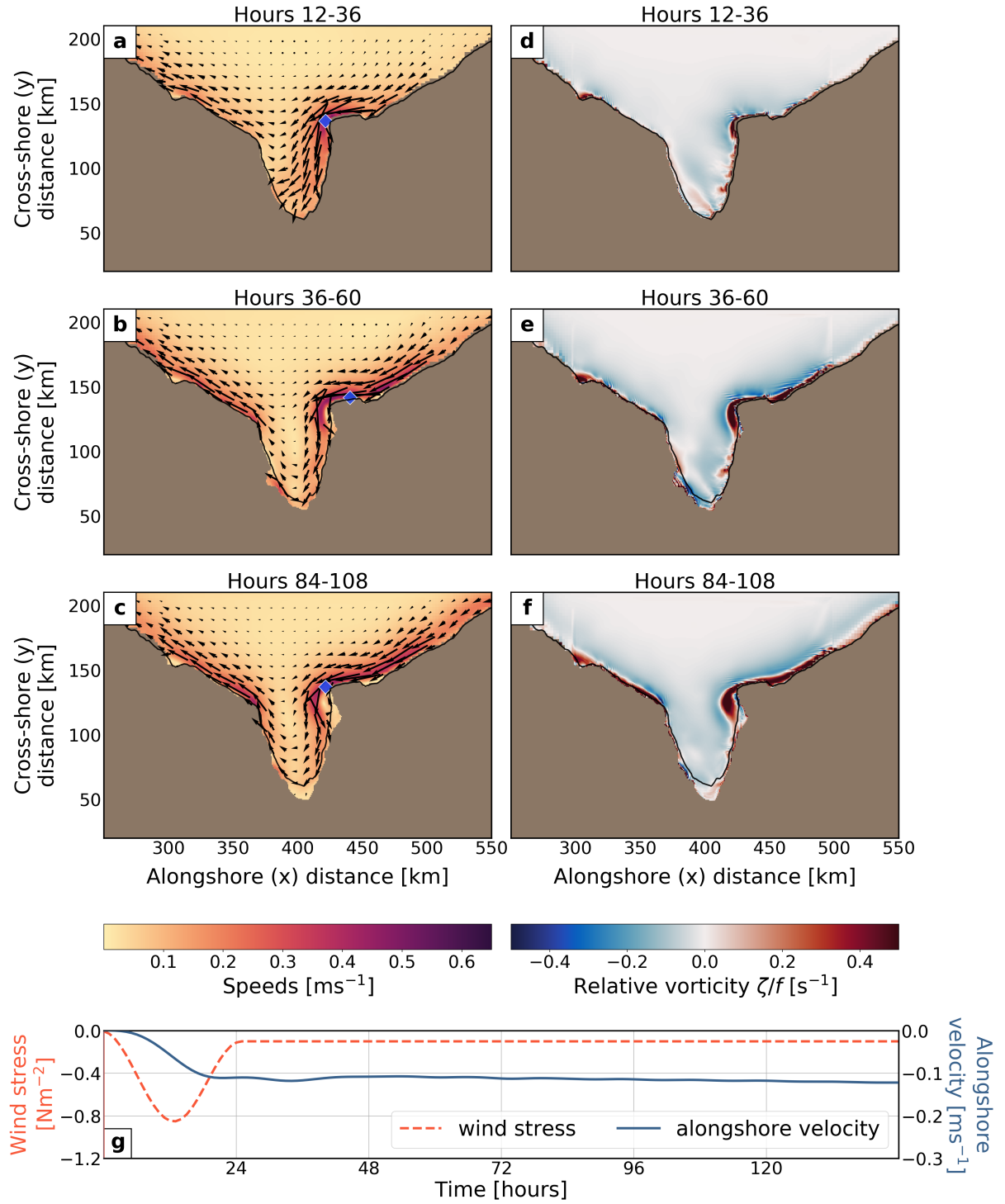
Figure 3.2: Characterization of the horizontal circulation on the UHW-representative surface in the realistic model: Format follows Figure 3.1.
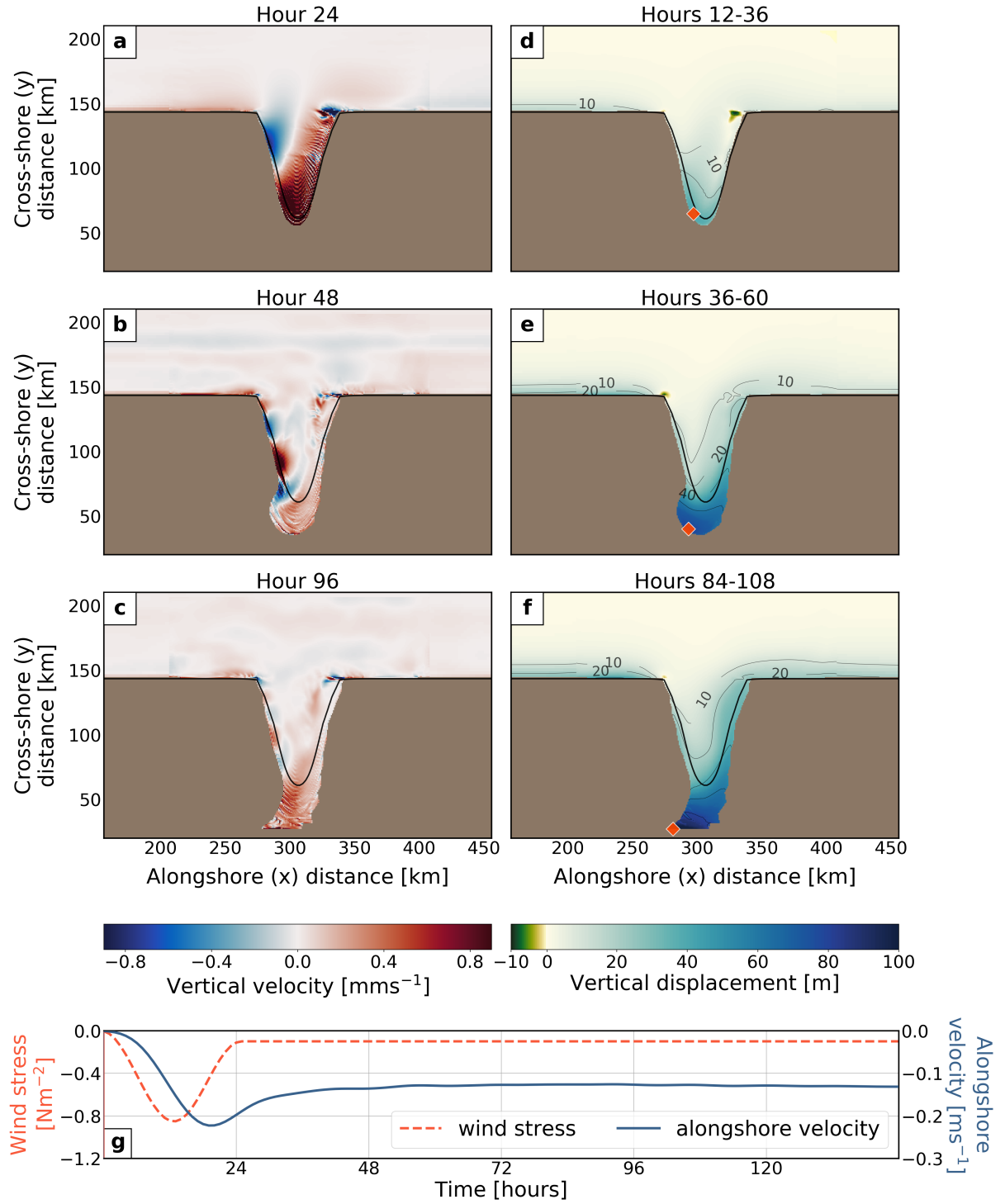
Figure 3.3: Characterization of the vertical velocity on and vertical displacement of the UHW-representative surface in the idealized model: Plan views of a-c) vertical velocity [mm s^{-1}] 1-hour averages and d-f) vertical displacement [m] averaged over three separate days (top row: hours 12-36, middle row: hours 36-60, bottom row: hours 84-108); g) time series of wind stress and average alongshore velocity of incoming currents over the upstream side of the shelf. The red diamond in plan views (a-c) shows the location of maximum upward displacement. The solid, black line outlines the canyon bathymetry at the initial depth of the water mass. Small scale oscillations in vertical velocity correspond to the steps in the model bathymetry.

43

Figure 3.4: Characterization of the vertical velocity on and vertical displacement of the UHW-representative surface in the realistic model: Format follows Figure 3.3.
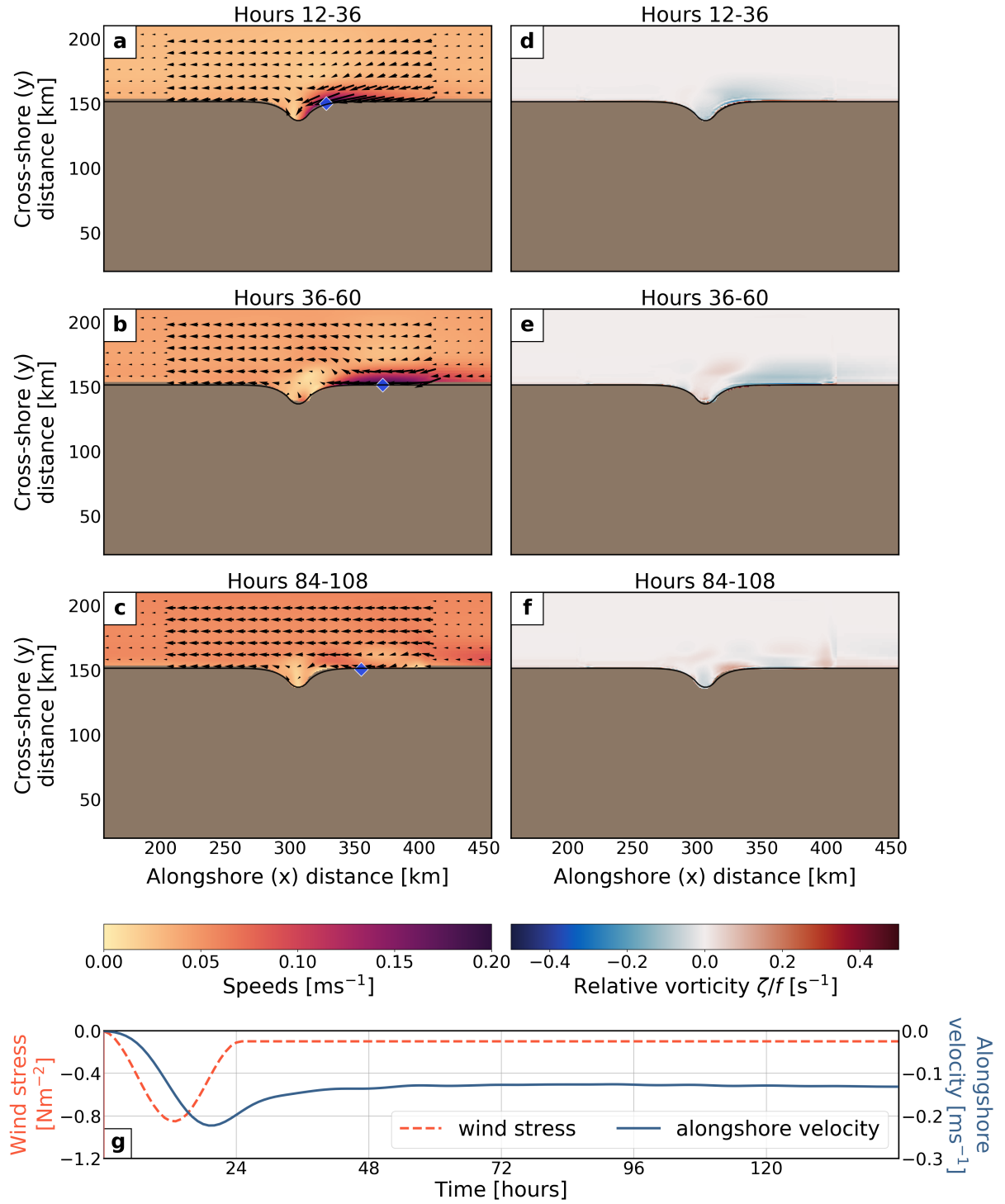
Figure 3.5: Characterization of the horizontal circulation on the AW-representative surface in the idealized model: Plan views of a-c) flow speed and direction [m s^{-1}] and d-f) relative vorticity [s^{-1}] averaged over three separate days (top row: hours 12-36, middle row: hours 36-60, bottom row: hours 84-108); g) time series of wind stress and average alongshore velocity of incoming currents over the upstream side of the shelf. The blue diamond in plan views (d-f) shows the location of maximum speeds. The solid, black line outlines the canyon bathymetry at the initial depth of the AW-representative surface.

45
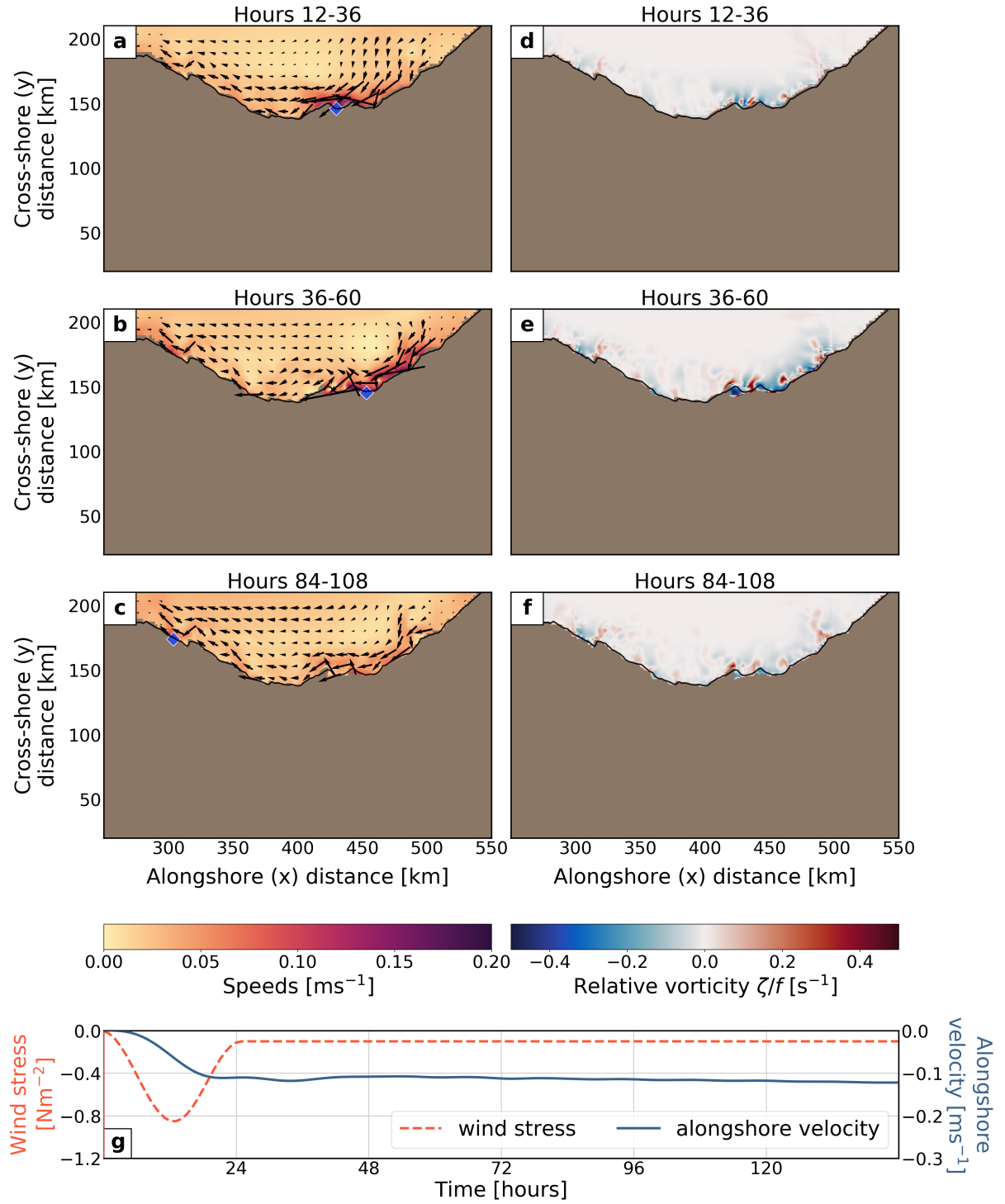
Figure 3.6: Characterization of the horizontal circulation on the AW-representative surface in the realistic model: Format follows Figure 3.5.
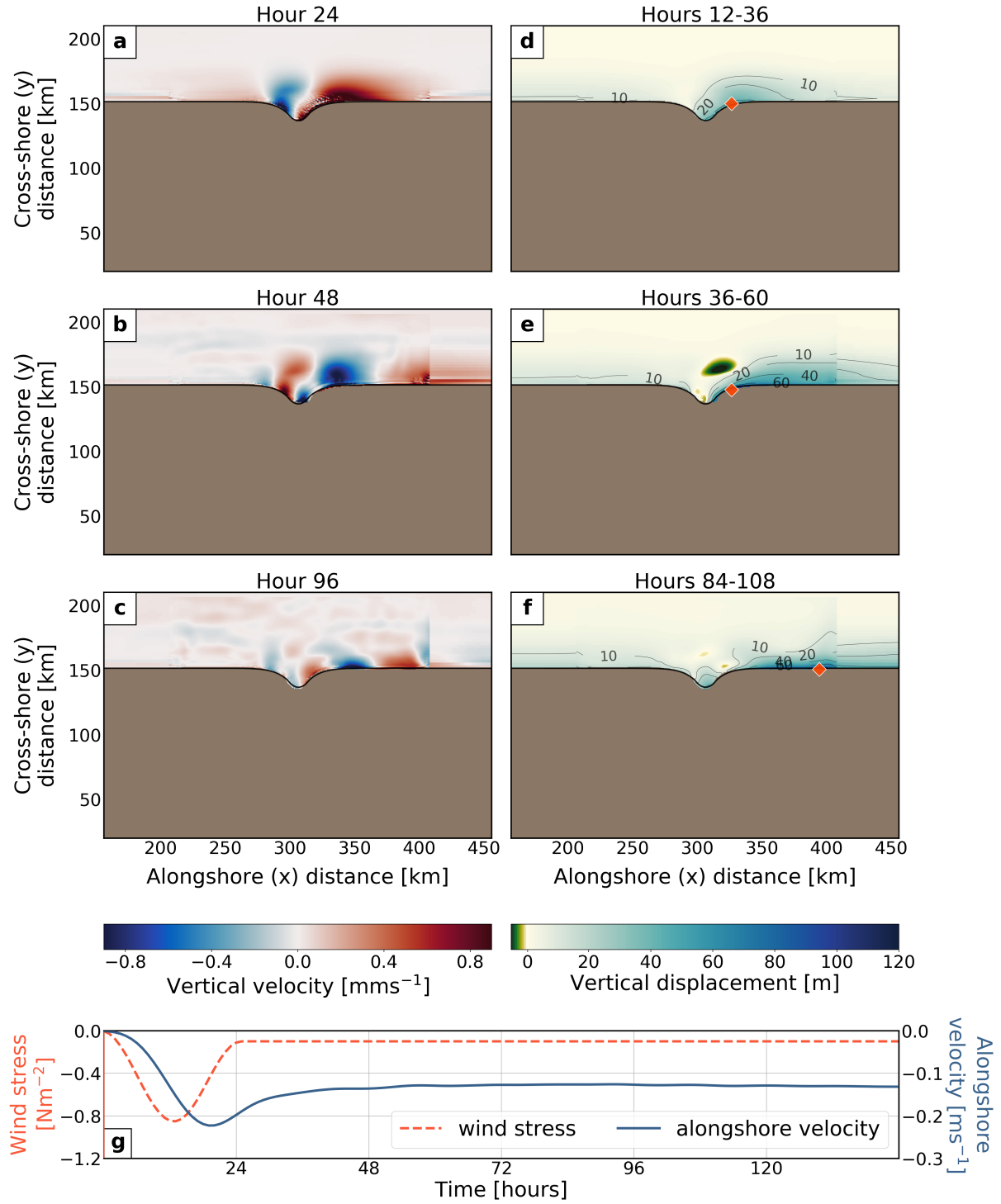
Figure 3.7: Characterization of the vertical velocity on and vertical displacement of the AW-representative surface in the idealized model: Plan views of a-c) vertical velocity [mm s⁻¹] 1-hour averages and d-f) vertical displacement [m] averaged over three separate days (top row: hours 12-36, middle row: hours 36-60, bottom row: hours 84-108); g) time series of wind stress and average alongshore velocity of incoming currents over the upstream side of the shelf. The red diamond in plan views (d-f) shows the location of maximum upward displacement. The solid, black line outlines the canyon bathymetry at the initial depth of the water mass. Small scale oscillations in vertical velocity correspond to the steps in the model bathymetry.

47

Figure 3.8: Characterization of the vertical velocity on and vertical displacement of the AW-representative surface in the realistic model: Format follows Figure 3.7.
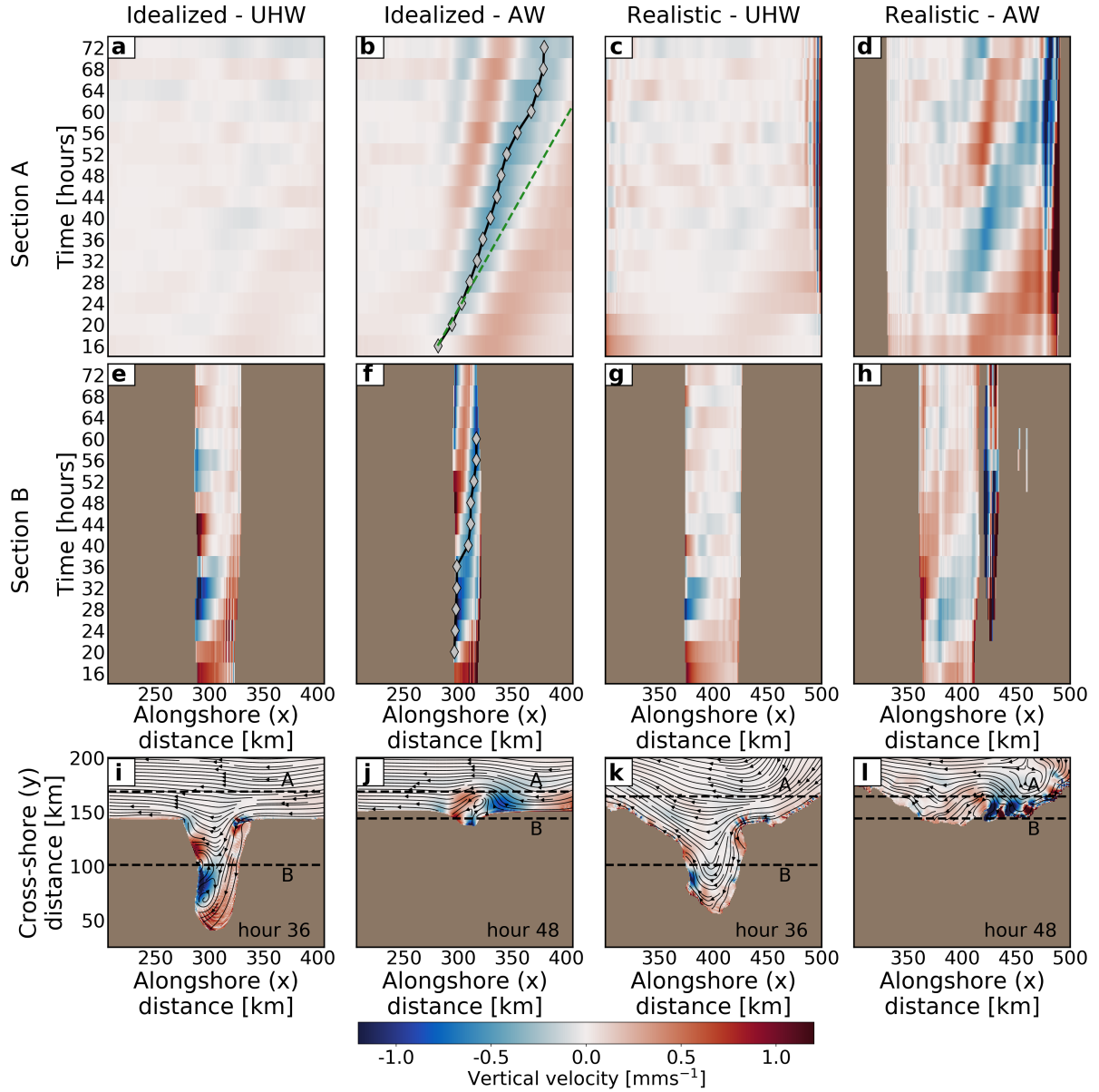
Figure 3.9: Hovmöller diagrams showing the propagation of the CTW along (a-d) Section A and (e-h) Section B and (i-l) plan views of vertical velocity [$mm\,s^{-1}$] on the UHW- and AW-representative surfaces in both idealized and realistic models. The transects for Section A and B are outlined by dashed, black lines in the plan views for the corresponding model and water mass surface. The speed of the CTW as it propagates (b) outside and (f) inside the canyon topography is estimated by tracking the path of the wave trough (solid, black line with gray diamond markers) on the Hovmöller plots for the AW-representative surface in the idealized model. The green, dashed line in panel (b) has a slope of $0.77\,m\,s^{-1}$, which is the speed of the CTW computed by the CTW model based on the wave parameters estimated for the CTW in the Mackenzie Canyon model simulations between hours 24 and 36 (Figure 3.11). The plan views (i-l) show average vertical velocities at hour 36 for UHW-representative surfaces and at hour 48 for AW-representative surfaces. The shape of the Hovmöller diagram changes according to the space occupied by the water mass during the upwelling event.
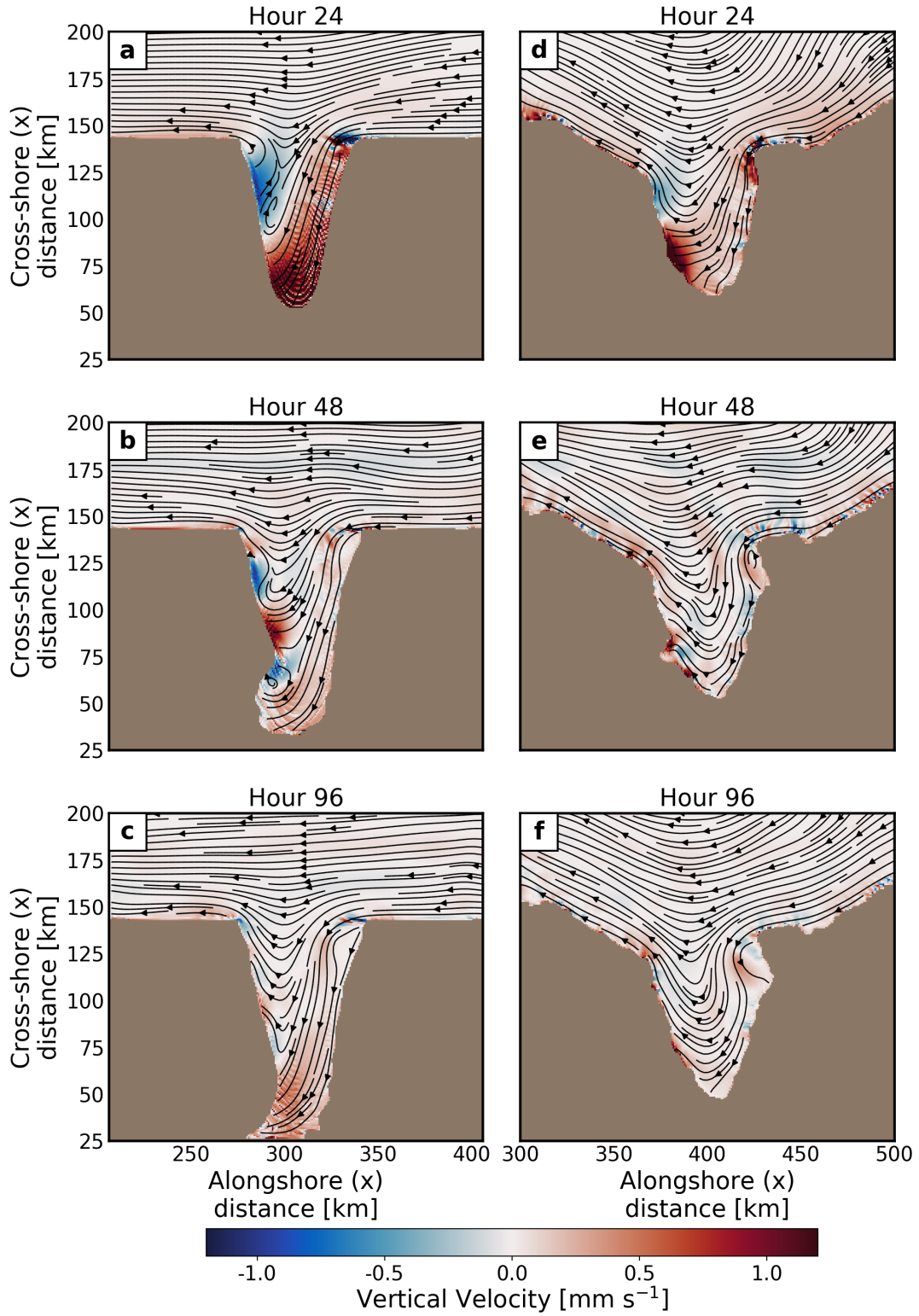
Figure 3.10: Plan views of vertical velocity $[\mathrm{mm\,s^{-1}}]$ on the UHW-representative surface at hours 24, 48, and 96 in the (a-c) idealized and (d-f) realistic models.
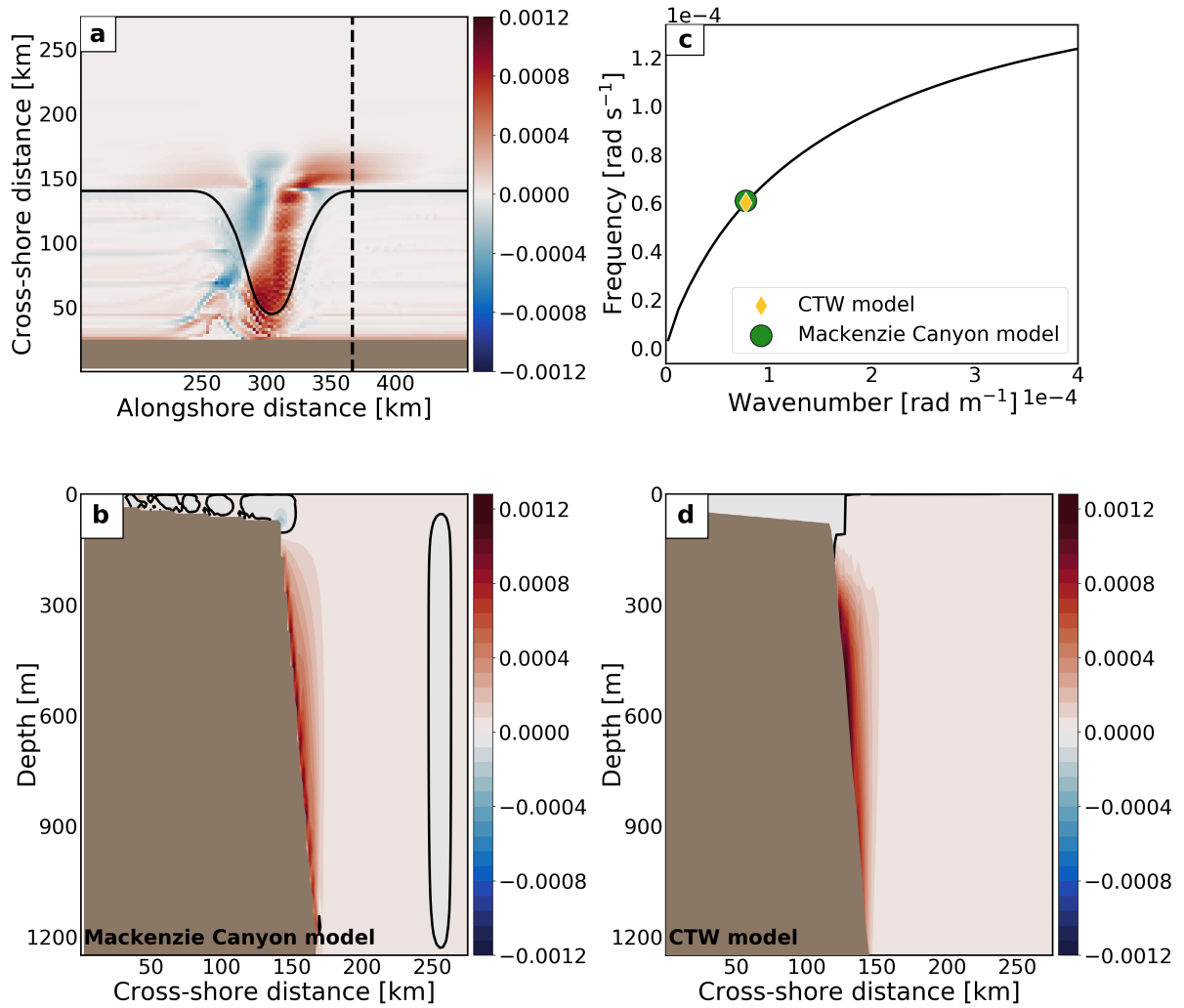
Figure 3.11: Characterization of the CTW in the Mackenzie Canyon model as the lowest wave mode calculated by the CTW model. a) Plan view and b) vertical cross-section along the dashed line in (a) of the Mackenzie Canyon model results for vertical velocity $[\mathrm{m\,s^{-1}}]$ at hour 24; c) dispersion curve of the lowest wave mode calculated by the CTW model for the cross-shore bathymetry profile outlined by the dashed, black line in (a); d) vertical, cross-shore structure for vertical velocity $[\mathrm{ms^{-1}}]$ of the lowest wave mode calculated by the CTW model. In panel (c), the green circle marks the wavenumber and frequency estimated between hours 24 and 36 for the CTW observed in the Mackenzie Canyon model simulations; the yellow diamond marks the wavenumber and frequency of the lowest wave mode computed by the CTW model. The solid, black line in (a) outlines the canyon bathymetry at the shelf-break depth (80 m). The solid, black contours in (b) and (d) outline wave nodes. The vertical velocity magnitudes calculated by the CTW model (d) have been normalized for comparison with the Mackenzie Canyon model results.

51
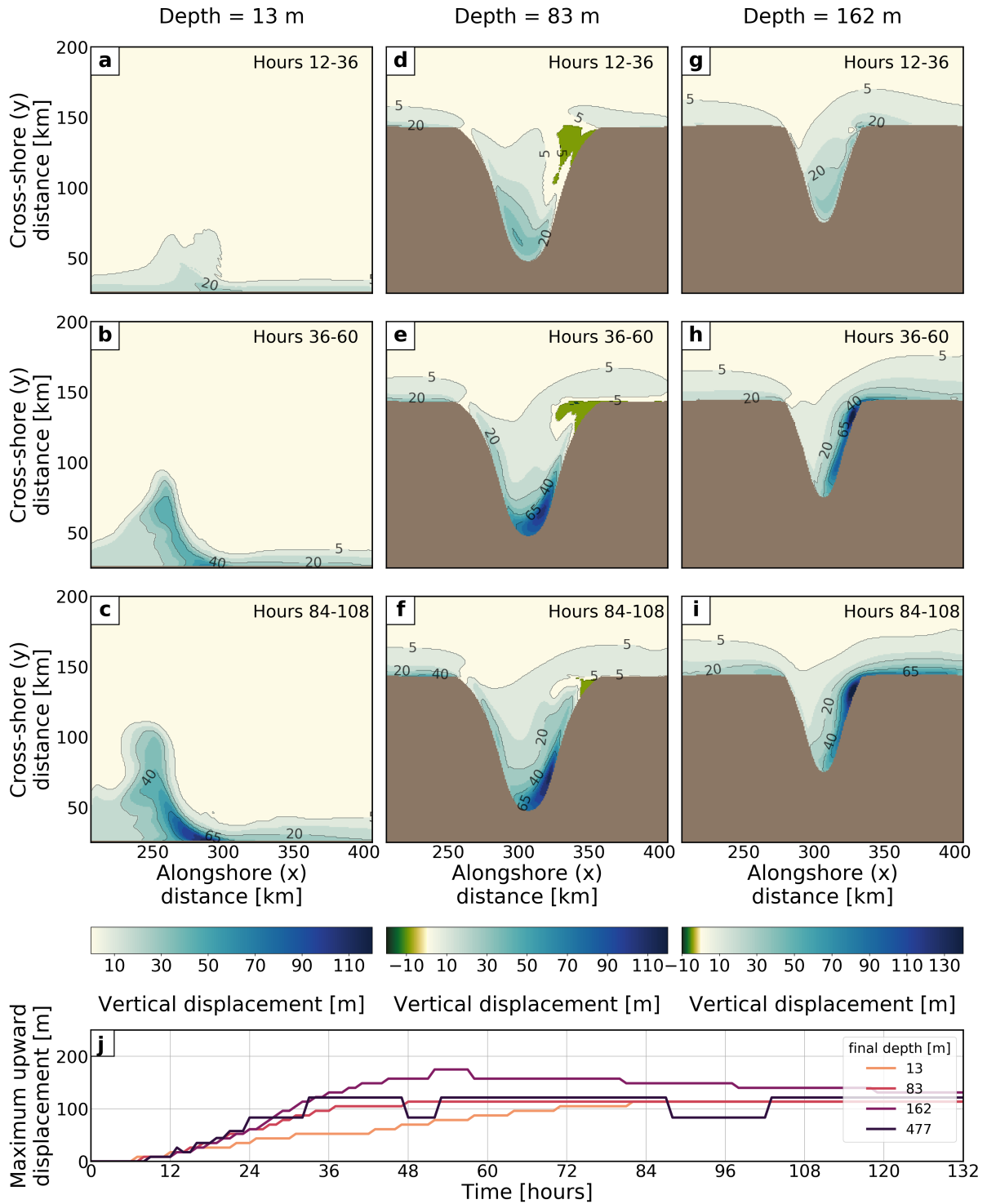
Figure 3.12: Vertical displacement [m] in the idealized model: Plan views at specific depths a-c) 13 m, d-f) 83 m, and g-i) 162 m averaged over three separate days (top row: hours 12-36, middle row: hours 36-60, bottom row: hours 84-108); j) time series of maximum vertical displacement values at depths 13 m, 83 m, 162 m, and 477 m.
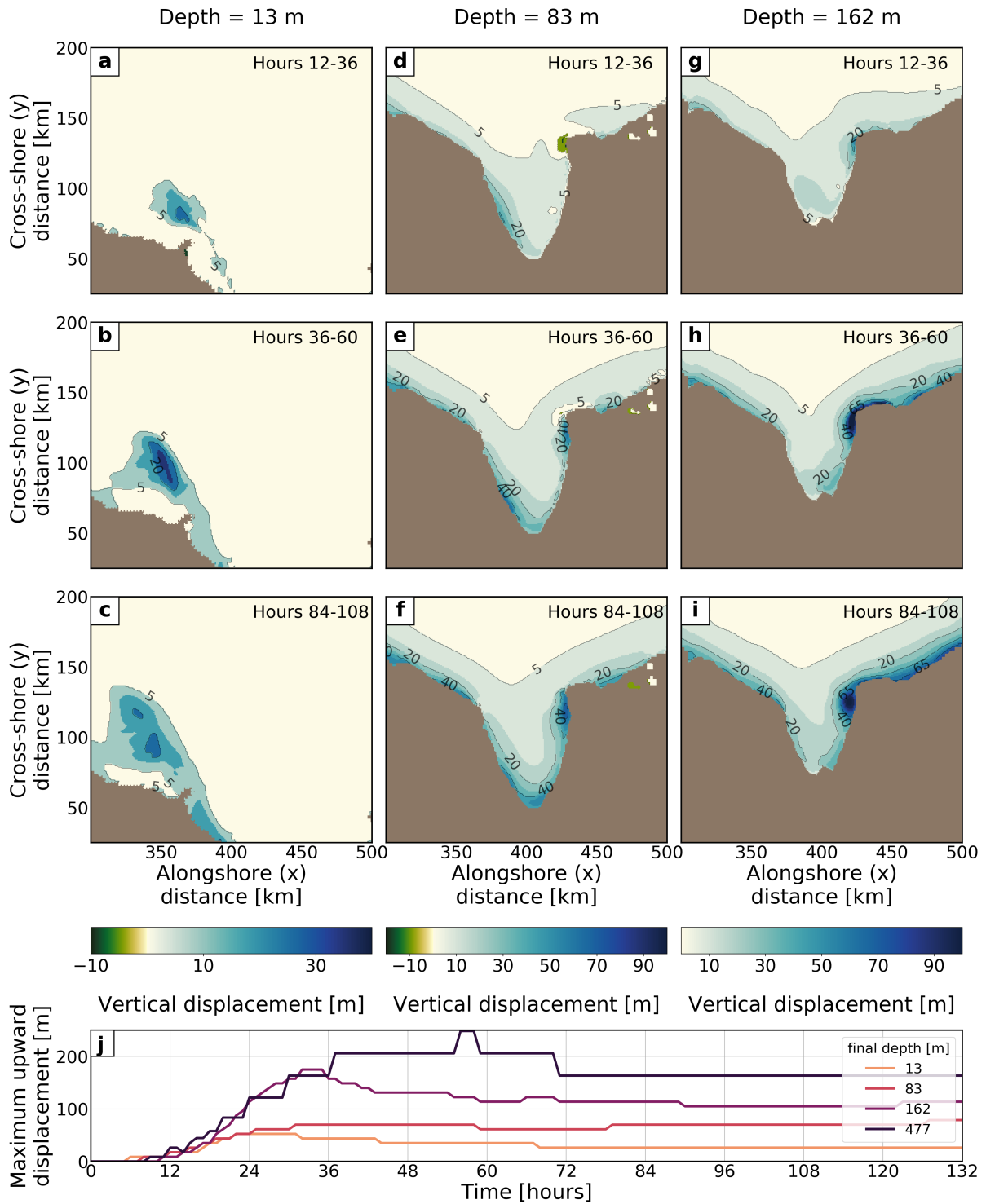
Figure 3.13: Vertical displacement [m] in the realistic model: Format follows Figure 3.12.
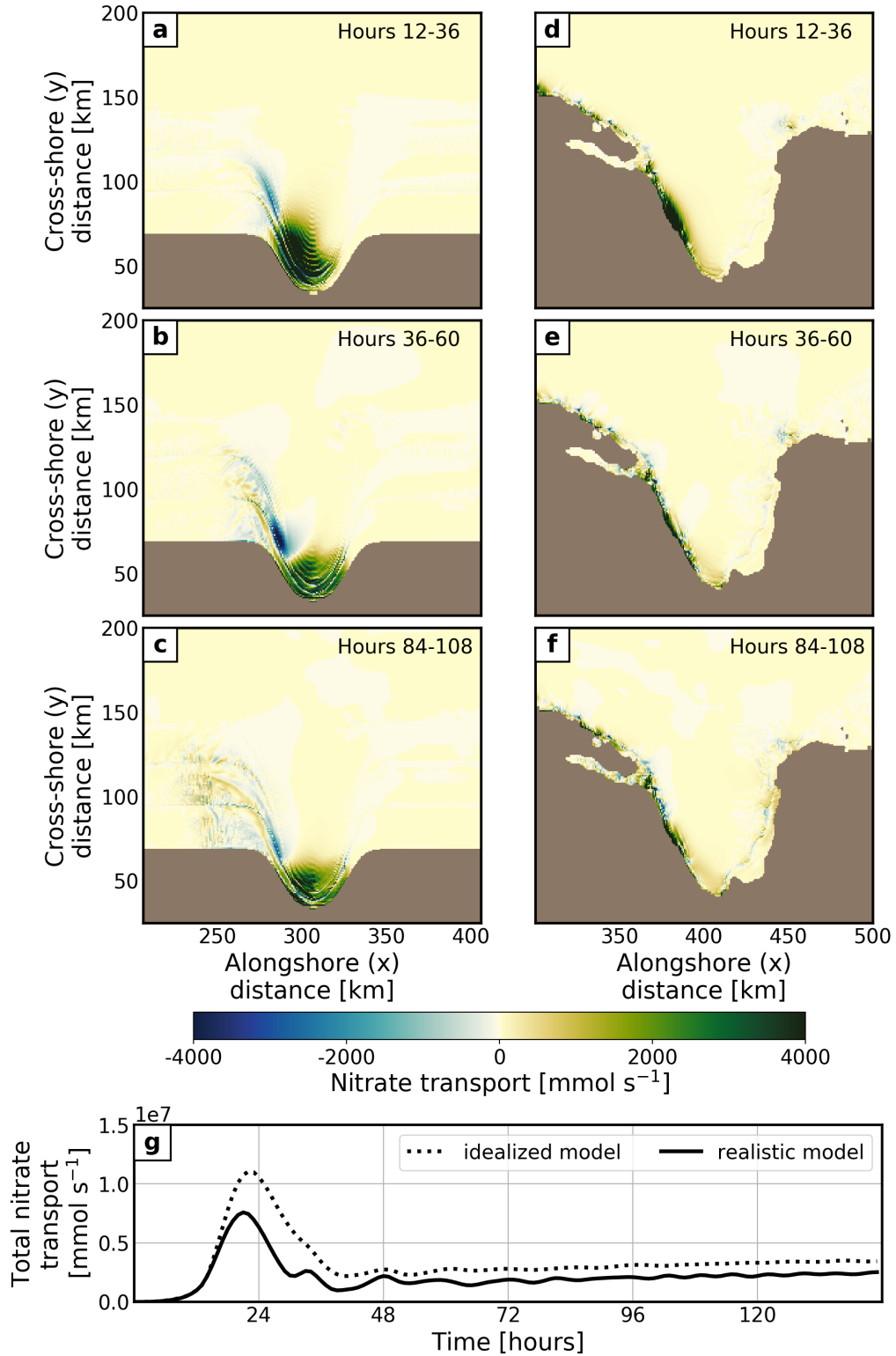
Figure 3.14: Plan views of a-c) idealized and d-f) realistic model results for nitrate transport across nitracline depth ($\sim$ 50 m) as estimated from salinity; g) time series of the total nitrate transport in the child model domain depicted in panels (a-f). Small scale structures in nitrate transport correspond to the steps in the model bathymetry.
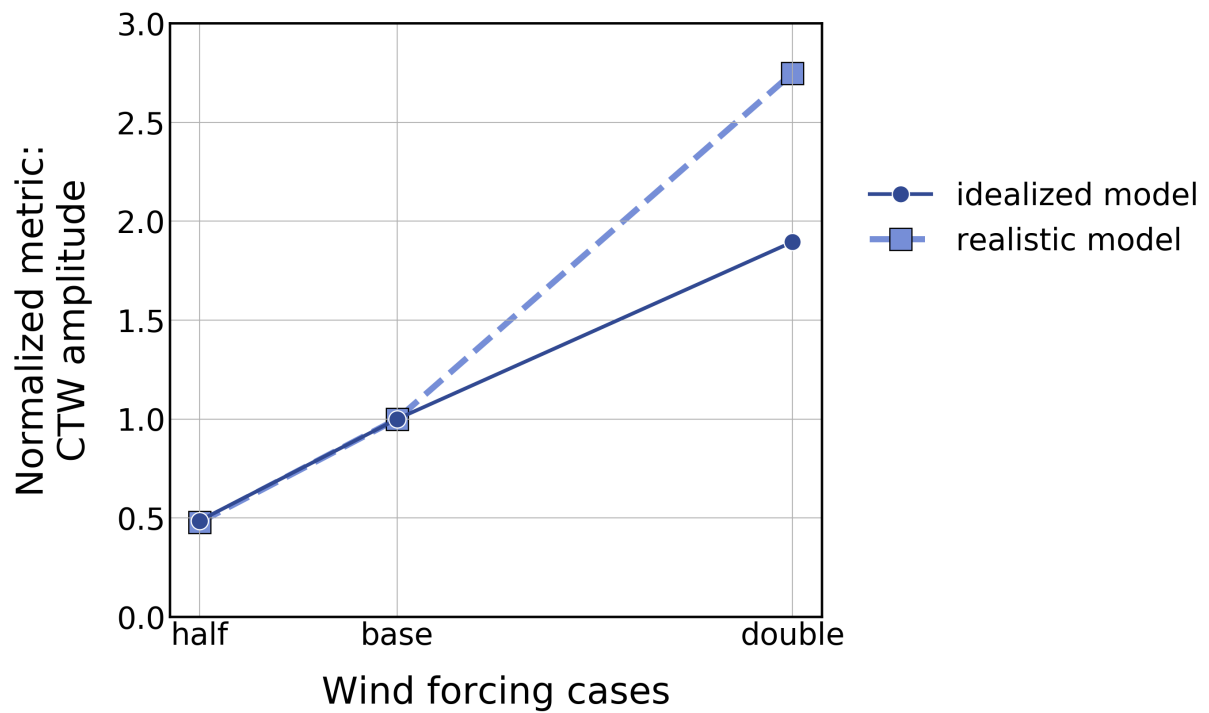
Figure 3.15: Comparison metric representing the response of CTW amplitude (through vertical velocity) to wind forcing for idealized and realistic models and normalized with respect to the 'base' wind forcing case. The metric is the mean positive vertical velocity on the slope just upstream of the canyon.
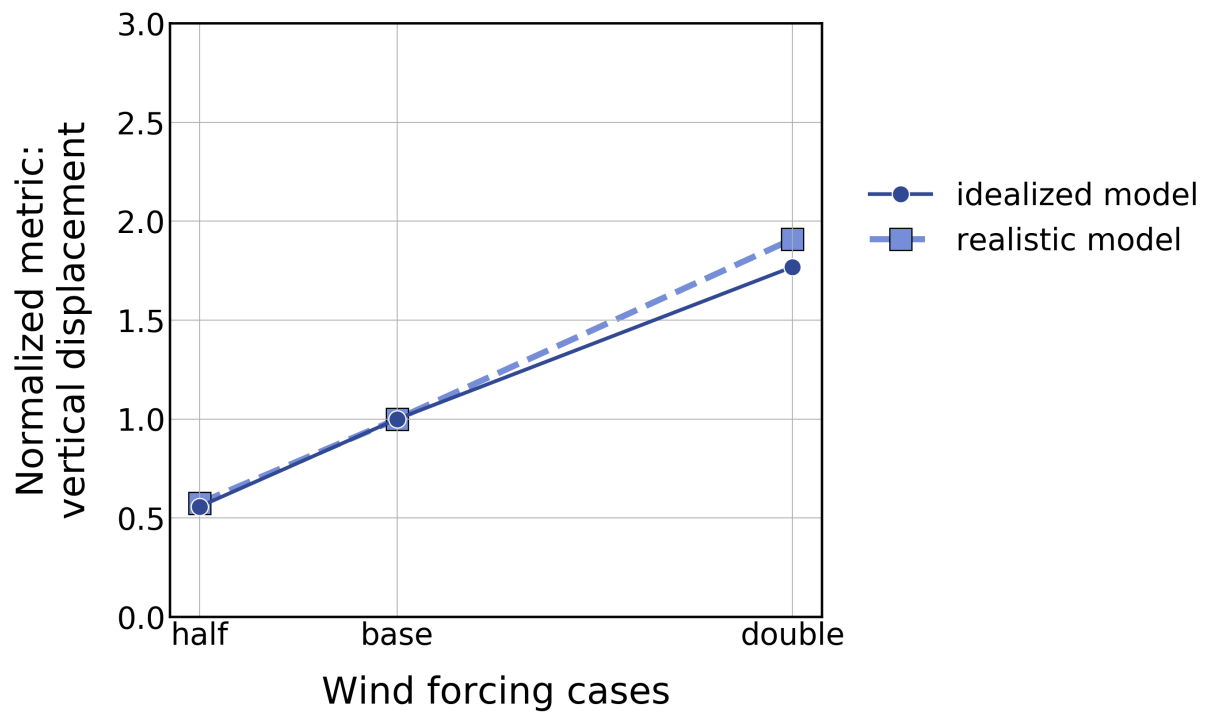
Figure 3.16: Comparison metric representing the response of upwelling (through vertical displacement) to wind forcing for idealized and realistic models and normalized with respect to the 'base' wind forcing case. The metric is the maximum positive value of vertical displacement in the canyon region.
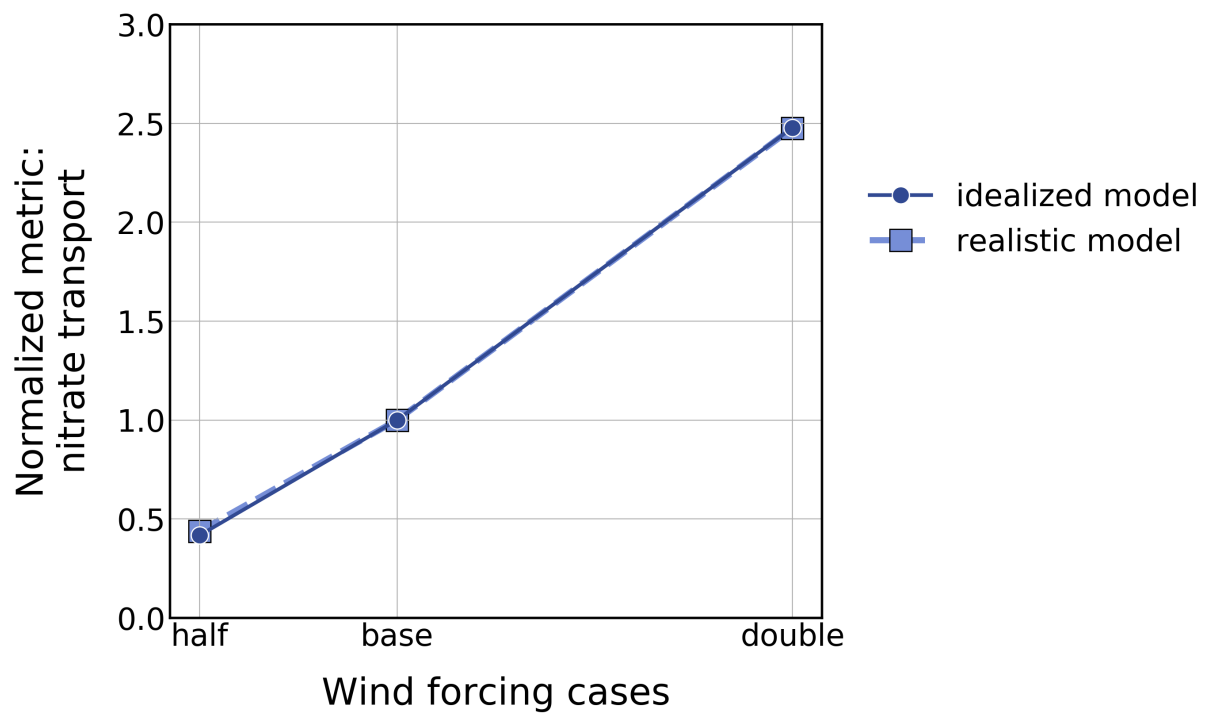
Figure 3.17: Comparison metric representing the response of nitrate transport for idealized and realistic models and normalized with respect to the 'base' wind forcing case. The metric is the total transport of nitrate in the child model domain.
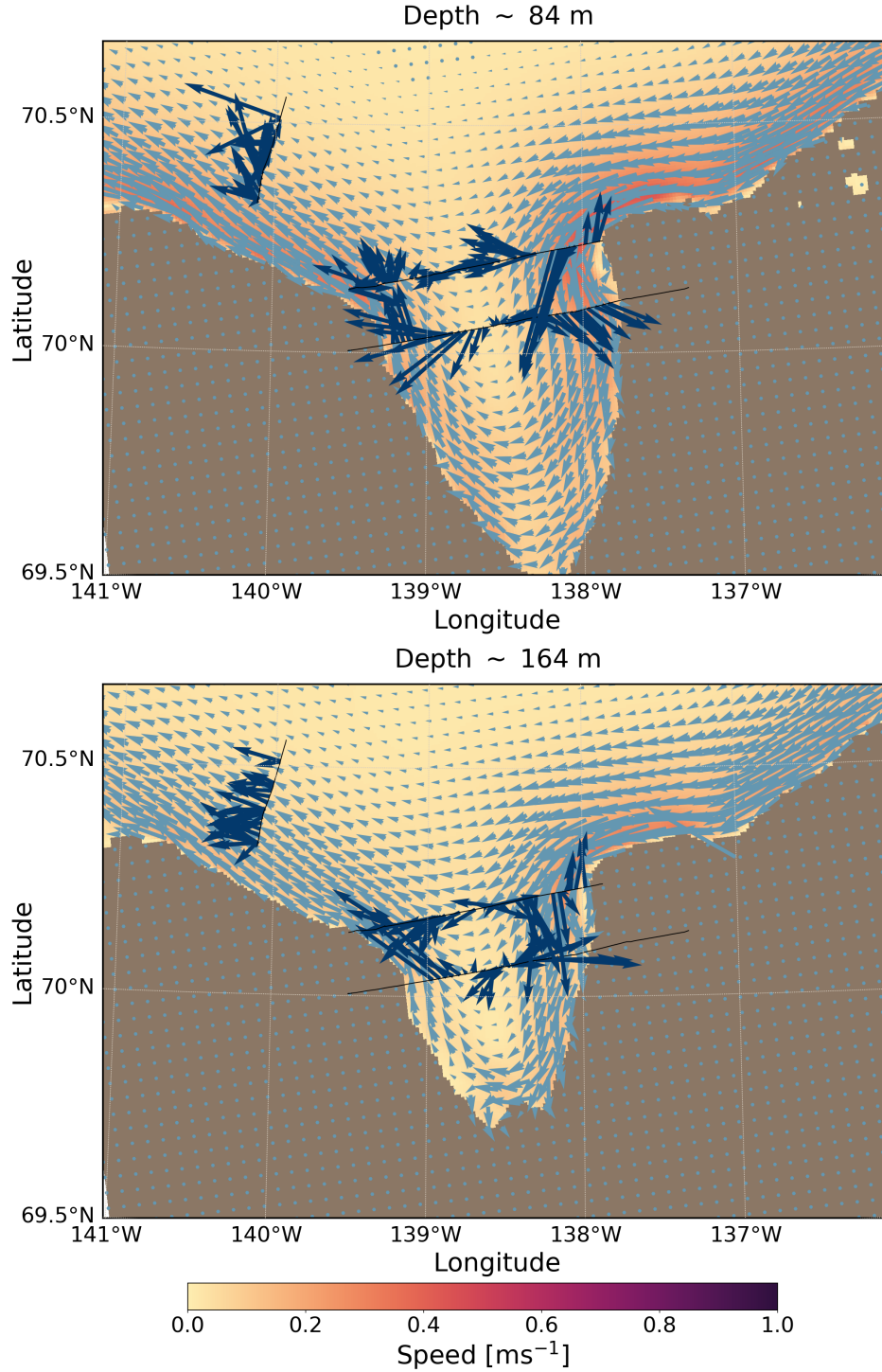
Figure 3.18: Model-to-observations comparison for currents in Mackenzie Canyon. Model results for flow speed and direction are represented by the coloured background and the light blue arrows populating the domain. Observational data for flow speed and direction are represented by dark blue arrows along three transects indicated by thin, black lines: 1) across the canyon mouth, 2) across the canyon near mid-length, and 3) cross-shore at the downstream slope. The length and angle of the arrows represent the horizontal components of velocity for both model results and observational measurements.
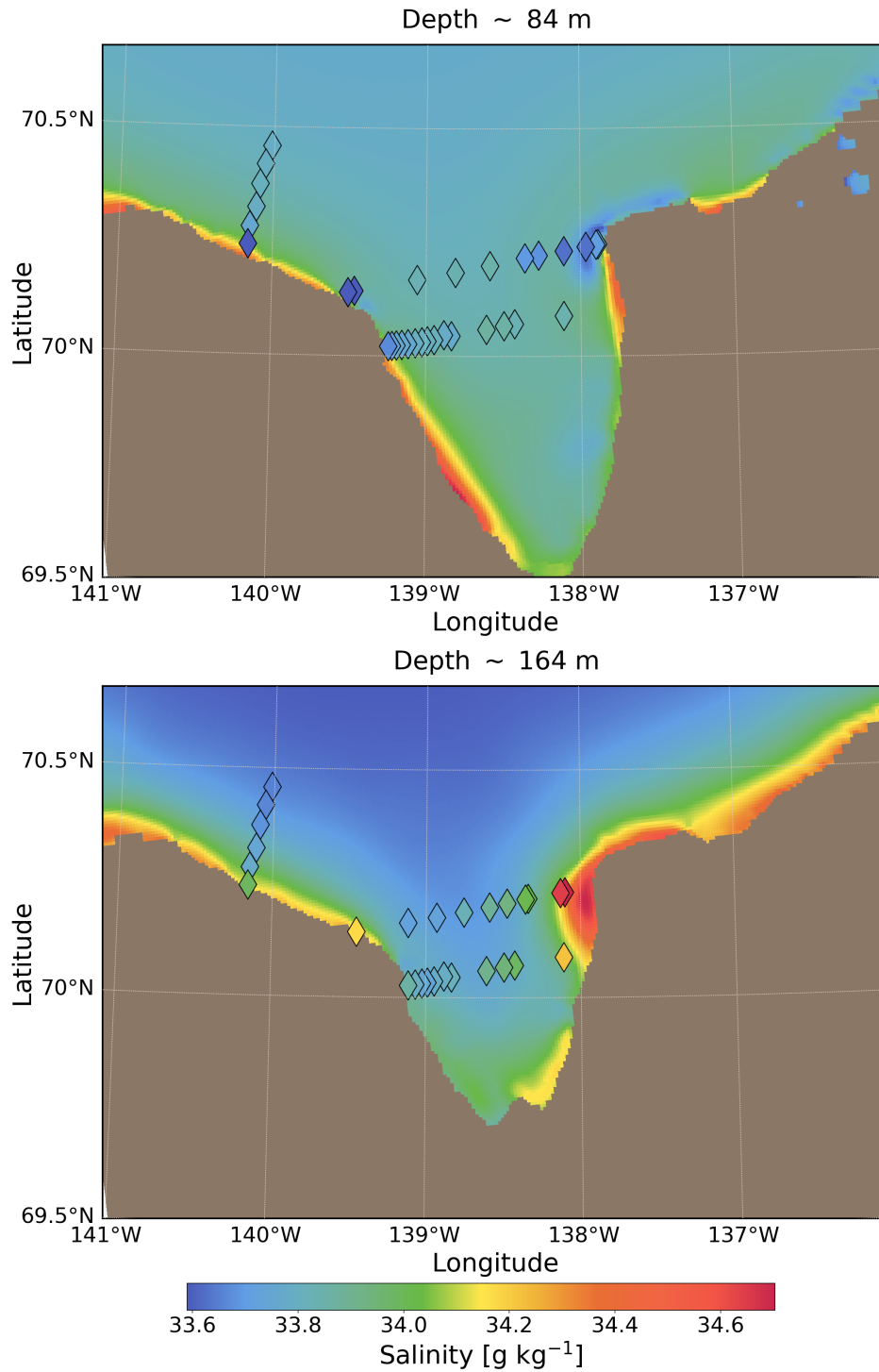
Figure 3.19: Model-to-observations comparison for salinity in Mackenzie Canyon. Model results for salinity are represented by the coloured background. Observational data for salinity is represented by the coloured diamonds along three transects: 1) across the canyon mouth, 2) across the canyon near mid-length, and 3) cross-shore at the downstream slope.

Chapter 4

Discussion

This study aims to describe the circulation and upwelling patterns in Mackenzie Canyon during an upwelling event, identify the flow features that act as significant modifiers of upwelling, compare the results of idealized and realistic simulations, and quantify the flux of nitrate across the nitracline depth induced by canyon upwelling. This section provides a review of the modelled patterns and time evolution of circulation and upwelling in Mackenzie Canyon and compares these findings to those for narrow, intermediate, and wide canyons from previous numerical, scaling, and observational studies. The effects of CTW propagation on the distribution of the upwelling signal in Mackenzie Canyon is also discussed. This section also provides further context on the influence of canyon upwelling on the transport and flux of nitrate across the nitracline depth, specifically as it relates to the seasonal draw-down in the Beaufort Sea. Finally, this section discusses the significance of having used both idealized and realistic models in this study and outlines the limitations of the model.

4.1 General circulation patterns and key features

Flows are topographically steered around Mackenzie Canyon. In stark contrast to the circulation around narrow canyons (with widths less than twice the radius of deformation), incoming, along-slope flows (between the depth of the canyon head $H_h = 40\,\mathrm{m}$ and the maximum depth of the canyon $H_c = 372\,\mathrm{m}$) turn into Mackenzie Canyon near the upstream side of the mouth, move along the canyon walls, and exit the canyon on the downstream side of the mouth. Flows above the head of Mackenzie Canyon, up to a depth of $\sim 4\,\mathrm{m}$, are also deflected over the canyon, showing a similar pattern as the circulation inside the canyon. In narrow canyons, near-surface, along-slope, and shelf flows cross the canyon with

little onshore deflection and support a cross-shore pressure gradient between the canyon head and mouth. The model results for Mackenzie Canyon, however, show lower pressure values around the canyon walls compared to the centre of the canyon (not shown), which is consistent with near-geostrophic flows following the canyon walls.

During the initial, transient stage of upwelling (within ∼36 hours from the start of the simulation), flows crossing Mackenzie Canyon encounter the downstream wall near the canyon mid-length. During the quasi-steady stage of upwelling (the remainder of the simulation), flows inside the canyon are more strongly steered around the topography and turn offshore closer to the canyon head. A stagnation (Hyun, 2004) or separation (Waterhouse et al., 2009) point is defined as the location where currents crossing the canyon reach the downstream wall and either turn onshore and flow around the canyon head or turn offshore and exit the canyon topography. The separation point is expected to be located closer to the canyon head for wider canyons and farther offshore for narrow canyons (Hyun, 2004). If the ratio between the canyon width W and radius of deformation a is used to define the dynamical width of a canyon, Mackenzie Canyon would be classified as marginally wide (or intermediate) with $W/a \sim 2.6$. The separation point in Mackenzie Canyon is near the canyon mid-length, as expected for intermediate canyons, only during the initial stage of upwelling when incoming currents are accelerating. For the remainder of the simulation, however, the separation point is at the canyon head like that expected for wider canyons.

The average alongshore velocity of shelf currents upstream of Mackenzie Canyon (between depths 13 m and 56 m) is $\sim 0.1\,\mathrm{m\,s^{-1}}$, and the Rossby number $R_{W*} = U/f\mathcal{R}_W$ (Howatt and Allen, 2013), which uses the width of the canyon taken half-way along the canyon length and measured across the shelf break isobath, is ∼0.02. As expected for canyons with low Rossby number R_{W*} (Allen, 2004; Howatt and Allen, 2013), flows inside Mackenzie Canyon follow the topography. In contrast, flows in narrow canyons with higher Rossby numbers R_{W*}, such as Astoria ($R_{W*}\sim0.21$) and Barkley canyons ($R_{W*}\sim0.11$), cross the canyon and form a cyclonic eddy over the canyon (Allen et al., 2001; Allen and Hickey, 2010; Hickey, 1997).

Along-slope flows turning into Mackenzie Canyon separate from the topography and, in the case of realistic bathymetry, readily form a closed cyclonic eddy on the upstream corner of the canyon mouth. In narrow canyons, a cyclonic eddy forms at rim depth and spans the canyon width as along-slope currents cross the canyon and turn onshore at the downstream wall near the mouth and flows above the

rim descend into the canyon, generating vortex stretching (Allen et al., 2001; She and Klinck, 2000; Waterhouse et al., 2009). Interestingly, however, previous experiments with intermediate and wide canyons (Hyun, 2004) show the formation of a cyclonic eddy with a width of approximately twice the deformation radius and extending across the length of the canyon. In Mackenzie Canyon, however, and specifically in the realistic model, the canyon eddy is approximately 10-15 km wide for the simulation with base wind forcing, and the region with strong cyclonic vorticity does not extend farther onshore than the mid-length of the canyon. In the idealized model, the region with strong cyclonic vorticity extends farther onshore, and the upstream eddy only forms at greater depths. Even when the cyclonic eddy forms in the idealized model, however, it only occupies a small area on the upstream side of the canyon like in the realistic model but unlike previous studies.

The conceptual model proposed for processes associated with the flow patterns around headlands may be partially analogous to the development of the cyclonic eddy attached to the upstream side of Mackenzie Canyon. The separation of alongshore flows and formation of a cyclonic eddy on the lee side of headlands have been attributed to friction associated with complex bottom topography and variations in vorticity resulting from the curvature of the topography (Castelao and Barth, 2007; Penven et al., 2000). Granted, other factors, such as orographic effects on wind stress, that have also been attributed to these circulation patterns (Castelao and Barth, 2007) are not applicable to those in submarine canyons, at least within the scope of this project. Conditions favourable to the formation of a headland eddy have been related to the Burger number $Bu = \left(NH/fL_{char}\right)^2$, where N is the Brunt-Väisälä frequency, H is the water depth, f is the Coriolis parameter, and L_{char} is a characteristic length scale, such as the size of the cape (Penven et al., 2000). Using the maximum canyon depth H_c=372 m and canyon width at the mouth W=62.7 km as the characteristic length scale, the Burger number of Mackenzie Canyon is ∼0.14. The low Burger number for Mackenzie Canyon indicates that the flow is expected to generate an attached cyclonic eddy (Penven et al., 2000) as advection and bottom friction become more dominant in this region compared to the adjacent slope where flows are more geostrophic.

4.2 Distribution and propagation of upwelling signal

Similar to narrow canyons, the location of the strongest upwelling in Mackenzie Canyon during the initial, transient pulse is associated with the interaction of accelerating, onshore flows inside the canyon with the topography. Like narrow canyons, the strongest upwelling in Mackenzie Canyon dur-

ing the initial stage of upwelling occurs near the canyon head and downstream wall. For the remainder of the simulation, however, the strongest upwelling in Mackenzie Canyon shifts to the upstream wall, while it typically remains along the downstream wall in narrow canyons. Notably, at greater depths, the upwelling signal initially near the canyon head clearly shifts upstream, exits the canyon topography, and propagates along the upstream slope with the canyon-induced CTW. The upstream (northeastward) propagation of the upwelling signal has been identified in observations along the Mackenzie Shelf (Carmack and Kulikov, 1998). While the dynamics involved in the propagation of a canyon-driven upwelling signal by a canyon-induced CTW have not yet been studied, strong upwelling events in canyons have previously been associated with the passage of remotely-forced CTWs (Sobarzo et al., 2016). The current existing literature on upwelling generated in canyons as a result of CTWs focuses on stationary, lee waves that are induced by the canyon bathymetric perturbation and arrested by incoming flows (Zhang and Lentz, 2017). These stationary, canyon-induced waves have been linked to the formation of isolated, alternating zones of upwelling and downwelling (Kaempf, 2012). In Mackenzie Canyon, and specifically on the AW-representative surface, temporary, localized zones of upwelling and downwelling are indeed observed, but these regions occur at the nodes of the CTW and move upstream with the CTW. With a phase speed of $\sim 0.78\,\mathrm{m\,s^{-1}}$ (as estimated between hours 24 and 36, Section 3.3), the CTW in Mackenzie Canyon propagates upstream since it is not arrested by incoming slope currents, which reach a maximum speed of only $\sim 0.2\,\mathrm{m\,s^{-1}}$ on the AW-representative surface in the idealized model during the initial stage of upwelling (Figure 3.5 (a)).

Model results showing the strongest upwelling near the head and along the upstream wall are corroborated by observational studies in Mackenzie Canyon (Macdonald et al., 1987; Williams et al., 2006) and numerical experiments with intermediate and wide canyons (Hyun, 2004). Compared to field measurements in Mackenzie Canyon (Carmack and Kulikov, 1998), the realistic model produces a slightly stronger upwelling signal in the canyon compared to adjacent slopes. Between $\sim 30\,\mathrm{m}$ and $\sim 214\,\mathrm{m}$, the model results for vertical displacement and field observations show that upwelling inside the canyon is approximately 3-4.5 times and 2-3 times as strong as the upwelling along the adjacent slope, respectively. Near the canyon head at a depth of $\sim 90\,\mathrm{m}$, the realistic model results for vertical displacement show water upwelled from a depth of ~ 171 m, which is similar to that measured in Mackenzie Canyon, $\sim 180\,\mathrm{m}$, for the same depth (Williams et al., 2006). The upwelling depth $\mathcal{Z}$, which is defined as the change in depth of the deepest water to be upwelled onto the shelf, is estimated to be ~ 37.3 m for

Mackenzie Canyon using the scaling in Howatt and Allen (2013).The model results for depths between the canyon head ($\sim$40 m) and shelf break ($\sim$80 m) show a maximum vertical displacement of $\sim$88 m, which is higher than that predicted by the scaling for upwelling depth $\mathcal{Z}$. Since Mackenzie Canyon is neither short nor narrow, this scaling is not likely to be appropriate. Indeed, model results for vertical displacement show a linear dependence on incoming velocity, which is inconsistent with the non-linear, advection processes considered for the scaling of $\mathcal{Z}$.

4.3 Canyon-induced nitrate flux and draw-down

In the Beaufort Sea, the base of the euphotic zone is typically below the nitracline, where the former is located between 60-70 m depth and the latter occurs at ~ 50 m depth (Ardyna et al., 2017; Monier et al., 2015). The model results for Mackenzie Canyon show sustained transport of nitrate across the nitracline depth and significant upwelling to the shelf. This finding supports previous suggestions that canyon-induced upwelling is likely to produce a flux of nutrient-rich water to the shelf that may support increased productivity (Macdonald et al., 1987; Williams et al., 2006).

The total nitrate flux across the nitracline depth in the model can be estimated using the diagnosed nitrate transport (Figure 3.14 and Section 3.5) over the canyon region (encompassed by the child domain, which extends 207 km and 184 km in the alongshore and cross-shore directions) and compared to the seasonal nitrate draw-down in the Beaufort Sea. For the canyon region in the realistic model, the total nitrate flux for the initial 36 hours is $\sim 348\,\mathrm{mmol\,m^{-2}}$. In the southern Beaufort Sea, the seasonal draw-down of nitrate is $\sim 5 \times 10^{-3}\,\mathrm{mol\,m^{-3}}$ over a depth of $\sim$30 m (Codispoti et al., 2013), resulting in a total draw-down of $\sim 150\,\mathrm{mmol\,m^{-2}}$. Therefore, the total nitrate supplied by Mackenzie Canyon over the first 36 hours of the upwelling event per unit area is $\sim$232% the seasonal draw-down. Considering that the area of the child domain is 0.09 times the area of the Beaufort Sea, this is a contribution of $\sim$21% of the seasonal drawdown in one canyon upwelling event. Approximately 6-7 upwelling events occur in Mackenzie Canyon over the course of a year (Carmack and Kulikov, 1998; Williams et al., 2006). Since draw-down (or net nutrient consumption) can be used to characterize net community production (Bergeron and Tremblay, 2014), Mackenzie Canyon can be considered a region of significant nutrient supply, which indicates the potential for high primary production.

The nitrate flux presented in this study accounts for the advection processes affecting the distribution of nitrate in the region. Submarine canyons, however, are regions of enhanced mixing due to the fo-

cusing of internal waves and tides. The effect of locally-enhanced mixing inside canyons on tracer flux has previously been studied with numerical experiments prescribing higher values for diffusivity to the model grid cells inside the canyon topography (Ramos-Musalem and Allen, 2019). Locally-enhanced diffusivity in canyons has been found to increase the tracer flux via upwelling by a maximum of 27%, and it results in larger tracer concentrations near the canyon rim (Ramos-Musalem and Allen, 2019).

4.4 Modelling with idealized and realistic bathymetry

The general circulation and upwelling patterns are similar in the idealized and realistic models. In both models, incoming along-slope currents separate from the topography and generate cyclonic vorticity on the upstream corner of the canyon mouth. The cyclonic eddy on the upstream side of the canyon mouth develops more readily and is more persistent in the realistic canyon. As a consequence, the onshore jet arrives at the canyon head with lower speeds, and therefore produces weaker upwelling, in the realistic model compared to the idealized model. The propagating signal of the CTW is more persistent in the idealized model since there is less scattering by the topography compared to the realistic model. As such, the propagation of the upwelling signal by the CTW is more distinct in the idealized model.

At present, only a few studies have conducted numerical experiments with both idealized and realistic bathymetry (Connolly and Hickey, 2014; Liu and Gan, 2015). Studies that have conducted numerical experiments with realistic canyon bathymetry have evaluated model performance using either observational data from the same canyon when data is available (Ardhuin et al., 1999) or results of previous laboratory and numerical experiments (Skliris et al., 2002). Other studies have noted that special care should be taken when considering open boundary conditions since models using realistic canyon bathymetry may produce unstable solutions (Dinniman and Klinck, 2002). This study finds that 1) a stable, numerical model with realistic bathymetry and stratification can largely reproduce the circulation and upwelling features observed in a real canyon and 2) idealized models capture the main circulation and upwelling features that develop in realistic models.

4.5 Model considerations and limitations

The numerical simulations conducted in this study are forced with a simplified analytical formulation for wind stress. Upwelling events in Mackenzie Canyon have been associated with the cumulative

effect of a series of brief, but intense, wind pulses (Carmack and Kulikov, 1998). Therefore, while the model provides results suitable for a process study, it does not necessarily exhibit all elements of an upwelling event in Mackenzie Canyon induced by realistic winds. Additionally, this project focuses solely on upwelling driven by wind stress at the surface, even though studies have found that ice-related stress at the surface not only produces but also amplifies the upwelling response in Mackenzie Canyon (Williams et al., 2006). Furthermore, the numerical model was not configured to include tides. This decision was made since diurnal and semidiurnal tidal currents reach a maximum of $\sim 0.3\,\mathrm{cm\,s^{-1}}$ and $\sim 0.7\,\mathrm{cm\,s^{-1}}$ (Kulikov et al., 2004), respectively, while alongshore currents upstream of the canyon have been observed with velocities of up to $\sim 40\,\mathrm{cm\,s^{-1}}$ during an upwelling event (Williams et al., 2006). Finally, the results presented in this study typically show larger horizontal and vertical velocities in the child model compared to the parent model. Future studies using nested modelling grids should carefully consider the values used for diffusivity, viscosity, and slip boundary conditions in the parent and child models in order to reduce differences in horizontal and vertical velocities between nested domains.

Chapter 5

Conclusions

Submarine canyons are sites for enhanced upwelling and distinct flow patterns compared to adjacent continental slopes and are associated with high biological productivity and nutrient and sediment cycling. Generally, currents in geostrophic balance over the shelf and slope are constrained to follow isobaths, inhibiting transport up the steep topography along coastlines. Ageostrophic flow dynamics in submarine canyons, however, permit strong deep ocean to shelf exchange. Numerical experiments offer a medium through which the various complex elements involved in the dynamics of canyon upwelling can be individually and systematically explored. Numerical models have significantly contributed to our understanding of flows over and near submarine canyons under both steady and transient forcing, as well as of the effects of stratification and canyon width on upwelling dynamics. Great strides have been made towards an ultimate goal of understanding and simulating the response of temporally and spatially variable flows with realistic stratification over realistic canyon topography with complex bottom roughness. Despite this progress, however, most numerical studies to date have employed idealized canyon bathymetry, and our current understanding of upwelling dynamics is largely limited to dynamically narrow canyons. As such, the goal of this study was to improve our understanding of the circulation patterns and upwelling mechanisms in a dynamically wide submarine canyon using numerical models with idealized and realistic bathymetry and to evaluate the model results with real-world observations. The following research questions were addressed.

1. *What are the circulation patterns inside and near Mackenzie Canyon during an upwelling event?*

    Flows are topographically steered around Mackenzie Canyon. Along-slope, incoming currents

turn into the canyon on the upstream side of the mouth, move along the canyon walls, exit the canyon on the downstream side of the mouth, and continue downstream along the slope. At the upstream corner of the canyon mouth, incoming currents turning into the canyon separate from the topography. This produces strong cyclonic vorticity on the lee side of the topography at the upstream side of the canyon and eventually generates a closed, cyclonic eddy in the realistic model. Furthermore, a coastal trapped wave is induced as incident flows interact with the canyon topography. The nature of this wave was examined using a model that calculates the modal structure and dispersion curve of coastal trapped waves possible for a given topographic profile and stratification. The results of the CTW model for the vertical velocity structure of the wave strongly resembled that of the wave produced in the Mackenzie Canyon model. As such, the results of the CTW model were used to identify the wave in the Mackenzie Canyon model simulations as a shelf wave.

2. *What flow features are significant modifiers of the upwelling in Mackenzie Canyon?*

During the initial, transient stage of the upwelling event, the strongest upwelling occurs at the centre and downstream side of the canyon head. Throughout the remainder of the simulation under steady forcing, the strongest upwelling occurs at the canyon head and along the upstream wall, especially over the region with strong cyclonic vorticity near the corner of the canyon mouth. Pressure values are higher closer to the centre of the canyon than along the walls, indicating that the enhanced upwelling observed in Mackenzie Canyon occurs under near-geostrophic conditions. The upwelling at the head and downstream wall of the canyon, especially during the initial stage of upwelling is likely a response to high-speed, accelerating flows encountering the canyon topography. As the CTW propagates upstream along the canyon walls, the upwelling signal shifts to the upstream side of the canyon. The influence of the CTW is especially evident along the salinity surface representative of the Atlantic Water, for which a strong upwelling signal clearly propagates upstream, exits the canyon, and continues along the upstream slope. The propagation of an upwelling signal has been identified by observational studies along the Mackenzie Shelf. Furthermore, upwelling over the area with strong cyclonic vorticity on the upstream side of the canyon is strongest for cases where the closed, cyclonic eddy forms.

3. *What differences in upwelling are caused by smoothing the topography to make an idealized canyon?*

There are three key differences between the idealized and realistic modelled results for circulation features that act as significant modifiers of upwelling in Mackenzie Canyon. While the flow separation of incoming currents and resulting cyclonic vorticity is simulated by the idealized model, the sharp topographic change on the upstream side of the realistic canyon facilitates the formation of a closed, cyclonic eddy. The realistic model, therefore, shows stronger eddy-induced upwelling than the idealized model. Additionally, flows that separate from the canyon topography in the idealized model maintain the high speeds required to support a strong onshore jet that produces strong upwelling at the canyon head. Therefore, upwelling at the canyon head is stronger in the idealized model compared to the realistic model. Finally, the rougher topography of the realistic model dissipates the signal of the CTW as it propagates upstream. As a result, the upwelling signal on the upstream side of the canyon and along the upstream slope is more persistent in the idealized model.

4. *Are the model results for circulation and upwelling in Mackenzie Canyon supported by observational evidence?*

The numerical model configured for this project successfully reproduces the key circulation and upwelling features of an observed upwelling event in Mackenzie Canyon. In-situ observations of flow speed and direction in the canyon corroborate the general anticyclonic circulation simulated by the realistic model. On the upstream side of the observational velocity transects, high-speed onshore-directed flows adjacent to low-speed outgoing flows corroborate model findings of the generation of a cyclonic eddy in that region of the canyon. Additionally, a strong upwelling signal is observed on the upstream side of the canyon near the mouth in both salinity observations and model results. While observations for currents and salinity were not available near the canyon head, previous observational studies in Mackenzie Canyon support the patterns simulated by the Mackenzie Canyon model.

5. *Does upwelling in Mackenzie Canyon produce significant upward transport of nitrate across the nitracline depth and, if so, how much?*

   Model results show that upwelling in Mackenzie Canyon produces significant upward transport of nitrate, especially near the head and on the downstream side of the canyon. In a single hour during an upwelling event, Mackenzie Canyon can supply one fifth of the seasonal nitrate draw-down in the Beaufort Sea. Over the initial 36 hours of an upwelling event, the total nitrate flux induced by Mackenzie Canyon is twice the seasonal draw-down in the Beaufort Sea.

This study makes three significant contributions to the scientific landscape of coastal oceanography research. The first and most critical contribution of this work is to the field of submarine canyons research, especially as it relates to physical processes in these coastal regions. Research of the upwelling dynamics in submarine canyons has been focused on canyons that are dynamically narrow (Figure D.1). This study is, in essence, a case study improving the current understanding of the circulation patterns and upwelling dynamics in wide canyons (Figure D.2). Such differences include topographic steering of flows under near-geostrophic conditions, the formation of a cyclonic eddy, the generation and propagation of a coastal trapped wave, and strong upwelling at the head and along the upstream side of the canyon. Future efforts in modelling, laboratory, or observational research should consider further characterizing the key circulation features explored in this study in order to develop our understanding on wide canyons further. Additionally, while previous studies show that the transport per unit width is larger in narrow canyons compared to wide canyons (Hyun, 2004), this study shows that the vertical displacement in Mackenzie Canyon is higher than that predicted using the established scaling for upwelling depth in narrow canyons. Future comparisons of upwelling metrics, such as upwelling depth and transport, should account for the aforementioned circulation features acting as significant upwelling modifiers in order to determine if either narrow or wide canyons produce more efficient upwelling.

The second key contribution of this study is to modelling efforts of the physical processes in submarine canyon regions. Previous studies on the upwelling dynamics in submarine canyons have mostly used idealized bathymetry. This study, however, finds that the mechanisms supporting enhanced upwelling in Mackenzie Canyon can be heavily impacted by the nature of the topography. Future work should continue to explore the differences in circulation and upwelling patterns between idealized and realistic models, especially for canyons with more complex geomorphology. Additionally, this work

shows value in comparing model results with in-situ observations.

Finally, this study investigates one of the many hydrodynamic mechanisms that modulate primary productivity, and by extension, impact the food supply that supports biological populations in the southeastern Beaufort Sea. In this region, nutrient (and specifically nitrate) supply controls the magnitude of phytoplankton productivity, while irradiance levels determine its timing (Carmack and Macdonald, 2002; Carmack et al., 2004; Macdonald et al., 1987). The strong stratification maintained by sea-ice meltwater in this region, however, hampers the vertical exchange of nutrients and limits primary production. Consequently, increased phytoplankton biomass is associated with the delivery of nitrate to the euphotic zone by shelf-break upwelling, mixing, advection from adjacent shelves, and riverine outflow (Carmack and Chapman, 2003; Pickart et al., 2013b; Tremblay et al., 2011, 2014). Therefore, and especially in view of the environmental stressors associated with climate change, continual research efforts are required for a comprehensive understanding of the physical mechanisms and biological pathways supporting coastal communities.

Future work is required to evaluate the response of the physical mechanisms studied here to the rapidly changing environmental conditions in the Arctic Ocean. For example, the ongoing trend of receding sea-ice (Ardyna et al., 2017; Carmack and Chapman, 2003; Carmack and Macdonald, 2002; Carmack et al., 2004; McLaughlin and Carmack, 2010; Williams and Carmack, 2015) results in increased meltwater, which supports a stronger stratification and further curtails the vertical transport of nutrients to the euphotic zone. Additionally, increased sea-ice melt intensifies aragonite undersaturation and acidity in the Arctic Ocean by enhancing carbon dioxide uptake as a result of increased open waters and decreasing the alkalinity and concentration of dissolved inorganic carbon in the water column through mixing with meltwater (Yamamoto-kawai, 2009). Increased aragonite undersaturation has been found to impair ability of calcifying organisms in high-latitude oceans to form calcium carbonate shells. On the other hand, longer periods of open water allow for increased wind-driven upwelling and higher light availability, both of which support primary productivity. Still, increased upwelling could bring aragonite undersaturated water to the shelves. In view of the numerous interlinked processes involved in this complex system, further physical-biological modelling efforts could be focused on systematically assessing the response of upwelling in Mackenzie Canyon to specific scenarios involving the expected changes to stratification and surface forcing (wind and ice) due to increasing sea-ice melt and the consequent impacts on local ecology.

Bibliography

Amundsen Science Data Collection, 2009. URL www.polardata.ca. CTD-Rosette data collected by the CCGS Amundsen in the Canadian Arctic. ArcticNet Inc., Quebec, Canada. Processed data. Version 1. → page 22

S. Allen. Topographically Generated, Subinertial Flows within A Finite Length Canyon. *Journal of Physical Oceanography*, 26:1608–1632, 1996. → pages 5, 7, 8, 21, 82

S. Allen, C. Vindeirinho, R. Thomson, M. Foreman, and D. Mackas. Physical and biological processes over a submarine canyon during an upwelling event. *Canadian Journal of Fisheries and Aquatic Sciences*, 58:671–684, 2001. ISSN 12057533. doi:10.1139/cjfas-58-4-671. → pages 4, 8, 61, 62

S. E. Allen. On subinertial flow in submarine canyons: Effect of geometry. *Journal of Geophysical Research*, 105(C1):1285–1297, 2000. ISSN 01480227. doi:10.1029/1999JC900240. → page 5

S. E. Allen. Restrictions on deep flow across the shelf-break and the role of submarine canyons in facilitating such flow. *Surveys in Geophysics*, 25:221–247, 2004. ISSN 01693298. doi:10.1007/s10712-004-1275-0. → pages xi, 5, 6, 7, 8, 17, 23, 61

S. E. Allen and X. Durrieu De Madron. A review of the role of submarine canyons in deep-ocean exchange with the shelf. *Ocean Science*, 5:607–620, 2009. ISSN 18120792. doi:10.5194/os-5-607-2009. → pages 4, 7, 8

S. E. Allen and B. M. Hickey. Dynamics of advection-driven upwelling over a shelf break submarine canyon. *Journal of Geophysical Research*, 115(C08018), 2010. ISSN 21699291. doi:10.1029/2009JC005731. → pages 5, 6, 7, 23, 61

F. Ardhuin, J.-M. Pinot, and J. Tintore. Numerical study of the circulation in a steep canyon off the Catalan coast (western Mediterranean). *Journal of Geophysical Research*, 104(C5):11115–11135, 1999. → page 65

M. Ardyna, M. Babin, E. Devred, A. Forest, M. Gosselin, P. Raimbault, and J. Tremblay. Shelf-basin gradients shape ecological phytoplankton niches and community composition in the coastal Arctic Ocean (Beaufort Sea). *Limnology and Oceanography*, 2017. ISSN 19395590. doi:10.1002/lno.10554. → pages 38, 64, 71

M. J. Berger and J. Oliger. Adaptive mesh refinement for hyperbolic partial differential equations. *Journal of Computational Physics*, 53:484–512, 1984. ISSN 10902716. doi:10.1016/0021-9991(84)90073-1. → page 20

M. Bergeron and J. Tremblay. Shifts in biological productivity inferred from nutrient drawdown in the southern Beaufort Sea (20032011) and northern BaffinBay (19972011), Canadian Arctic.

Geophysical Research Letters, 41:3979–3987, 2014. ISSN 00195499. doi:doi:10.1002/2014GL059649. → page 64

K. L. Bosley, J. W. Lavelle, R. D. Brodeur, W. W. Wakefield, R. L. Emmett, E. T. Baker, and K. M. Rehmke. Biological and physical processes in and around Astoria submarine Canyon, Oregon, USA. *Journal of Marine Systems*, 50:21–37, 2004. ISSN 09247963. doi:10.1016/j.jmarsys.2003.06.006. → page 4

A. H. Bouma. Naming of undersea features. *Geo-Marine Letters*, 10(3):119–125, 1990. ISSN 02760460. doi:10.1007/BF02085926. → page 1

K. H. Brink. A Comparison of Long Coastal Trapped Wave Theory with Observations off Peru. *Journal of Physical Oceanography*, 12:897–913, 1982. doi:10.1175/1520-0485(1982)012⟨0897:ACOLCT⟩2.0.CO;2. → page 35

K. H. Brink. Stable coastal-trapped waves with stratification, topography and mean flow, 2018. URL https://hdl.handle.net/1912/10527. → pages 24, 35, 36

R. D. Brodeur. Habitat-specific distribution of Pacific ocean perch (Sebastes alutus) in Pribilof Canyon, Bering Sea. *Continental Shelf Research*, 21:207–224, 2001. ISSN 02784343. doi:10.1016/S0278-4343(00)00083-2. → page 4

M. Canals, P. Puig, X. D. De Madron, S. Heussner, A. Palanques, and J. Fabres. Flushing submarine canyons. *Nature*, 444:354–357, 2006. ISSN 14764687. doi:10.1038/nature05271. → page 3

M. Canals, J. B. Company, D. Martín, A. Sànchez-Vidal, and E. Ramírez-Llodrà. Integrated study of Mediterranean deep canyons: Novel results and future challenges. *Progress in Oceanography*, 118: 1–27, 2013. ISSN 00796611. doi:10.1016/j.pocean.2013.09.004. → page 4

E. Carmack and D. C. Chapman. Wind-driven shelf/basin exchange on an Arctic shelf: The joint roles of ice cover extent and shelf-break bathymetry. *Geophysical Research Letters*, 2003. ISSN 00948276. doi:10.1029/2003GL017526. → page 71

E. C. Carmack and E. A. Kulikov. Wind-forced upwelling and internal Kelvin wave generation in Mackenzie Canyon, Beaufort Sea. *Journal of Geophysical Research: Oceans*, 103(C9): 18447–18458, 1998. ISSN 21699291. doi:10.1029/98JC00113. → pages xii, 9, 11, 12, 13, 18, 23, 24, 63, 64, 66

E. C. Carmack and R. W. Macdonald. Oceanography of the Canadian shelf of the Beaufort Sea: A setting for marine life. *Arctic*, 55:29–45, 2002. ISSN 00040843. doi:10.1126/science.100.2596.291. → pages 10, 11, 71

E. C. Carmack, R. W. Macdonald, and J. E. Papadakis. Water mass structure and boundaries in the Mackenzie shelf estuary. *Journal of Geophysical Research*, 94(C12):18043–18055, 1989. ISSN 0148-0227. doi:10.1029/JC094iC12p18043. → pages 9, 10

E. C. Carmack, R. W. Macdonald, and S. Jasper. Phytoplankton productivity on the Canadian Shelf of the Beaufort Sea. *Marine Ecology Progress Series*, 277:37–50, 2004. → pages 10, 11, 71

R. M. Castelao and J. A. Barth. The Role of Wind Stress Curl in Jet Separation at a Cape. *Journal of Physical Oceanography*, 37(11), 2007. → page 62

L. A. Codispoti, V. Kelly, A. Thessen, P. Matrai, S. Suttles, V. Hill, M. Steele, and B. Light. Synthesis of primary production in the Arctic Ocean: III. Nitrate and phosphate based estimates of net community production. *Progress in Oceanography*, 110:126–150, 2013. ISSN 0079-6611. doi:10.1016/j.pocean.2012.11.006. URL http://dx.doi.org/10.1016/j.pocean.2012.11.006. → page 64

T. P. Connolly and B. M. Hickey. Regional impact of submarine canyons during seasonal upwelling. *Journal of Geophysical Research: Oceans*, 119:953–975, 2014. doi:10.1002/2013JC009452.Received. → page 65

F. C. De Leo, J. C. Drazen, E. W. Vetter, A. A. Rowden, and C. R. Smith. The effects of submarine canyons and the oxygen minimum zone on deep-sea fish assemblages off Hawai'i. *Deep-Sea Research Part I: Oceanographic Research Papers*, 64:54–70, 2012. ISSN 09670637. doi:10.1016/j.dsr.2012.01.014. → page 4

L. Debreu and E. Blayo. Two-way embedding algorithms: a review. *Ocean Dynamics*, 58:415–428, 2008. ISSN 16167341. doi:10.1007/s10236-008-0150-9. → page 20

L. Debreu, C. Vouland, and E. Blayo. AGRIF: Adaptive grid refinement in Fortran. *Computers and Geosciences*, 34:8–13, 2008. ISSN 00983004. doi:10.1016/j.cageo.2007.01.009. → pages 19, 20

L. Debreu, P. Marchesiello, P. Penven, and G. Cambon. Two-way nesting in split-explicit ocean models: Algorithms, implementation and validation. *Ocean Modelling*, 49-50:1–21, 2012. ISSN 14635003. doi:10.1016/j.ocemod.2012.03.003. URL http://dx.doi.org/10.1016/j.ocemod.2012.03.003. → page 20

M. S. Dinniman and J. M. Klinck. The Influence of Open versus Periodic Alongshore Boundaries on Circulation near Submarine Canyons. *Journal of Atmospheric and Oceanic Technology*, 19: 1722–1737, 2002. → page 65

K. H. Dunton, T. Weingartner, and E. C. Carmack. The nearshore western Beaufort Sea ecosystem: Circulation and importance of terrestrial carbon in arctic coastal food webs. *Progress in Oceanography*, 71:362–378, 2006. ISSN 00796611. doi:10.1016/j.pocean.2006.09.011. → page 10

U. Fernandez-Arcaya, E. Ramirez-Llodra, J. Aguzzi, A. L. Allcock, J. S. Davies, A. Dissanayake, P. Harris, K. Howell, V. A. I. Huvenne, M. Macmillan-Lawler, J. Martín, L. Menot, M. Nizinski, P. Puig, A. A. Rowden, F. Sanchez, and I. M. J. Van den Beld. Ecological Role of Submarine Canyons and Need for Canyon Conservation: A Review. *Frontiers in Marine Science*, 4, 2017. ISSN 2296-7745. doi:10.3389/fmars.2017.00005. → page 3

R. A. Flather. A Tidal Model of the North-West European Continental Shelf. *Memoires Société Royale des Sciences de Liège*, 1976. → page 21

A. Forest, M. Sampei, H. Hattori, R. Makabe, H. Sasaki, M. Fukuchi, P. Wassmann, and L. Fortier. Particulate organic carbon fluxes on the slope of the Mackenzie Shelf (Beaufort Sea): Physical and biological forcing of shelf-basin exchanges. *Journal of Marine Systems*, 68:39–54, 2007. ISSN 09247963. doi:10.1016/j.jmarsys.2006.10.008. → pages 9, 10

H. J. Freeland and K. L. Denman. A topographically controlled upwelling center off southern Vancouver Island. *Journal of Marine Research*, 40:1069–1093, 1982. → pages 4, 5

W. D. Gardner. Periodic resuspension in Baltimore canyon by focusing of internal waves. *Journal of Geophysical Research*, 49(C12):18185–19194, 1989. ISSN 0148-0227. doi:10.1029/JC094iC12p18185. → page 4

R. L. Gordon and N. F. Marshall. Submarine canyons: internal wave traps? *Geophysical Research Letters*, 3(10):622–624, 1976. → page 4

R. A. Hall, T. Aslam, and V. A. Huvenne. Partly standing internal tides in a dendritic submarine canyon observed by an ocean glider. *Deep-Sea Research Part I: Oceanographic Research Papers*, 126:73–84, 2017. ISSN 09670637. doi:10.1016/j.dsr.2017.05.015. → page 4

P. T. Harris and T. Whiteway. Global distribution of large submarine canyons: Geomorphic differences between active and passive continental margins. *Marine Geology*, 285:69–86, 2011. ISSN 00253227. doi:10.1016/j.margeo.2011.05.008. → pages 1, 2

B. Hickey and N. Banas. Why is the Northern End of the California Current System So Productive? *Oceanography*, 21(4):90–107, 2008. ISSN 10428275. doi:10.5670/oceanog.2008.07. URL https://tos.org/oceanography/article/ why-is-the-northern-end-of-the-california-current-system-so-productive. → page 4

B. M. Hickey. The Response of a Steep-Sided, Narrow Canyon to Time-Variable Wind Forcing. *Journal of Physical Oceanography*, 27:697–726, 1997. → pages 5, 8, 61

P. R. Hill, S. M. Blasco, J. R. Harper, and D. B. Fissel. Sedimentation on the Canadian Beaufort Shelf. *Continental Shelf Research*, 11:821–863, 1991. → pages 9, 10

S. K. Hooker, H. Whitehead, and S. Gowans. Marine protected area design and the spatial and temporal distribution of cetaceans in a submarine canyon. *Conservation Biology*, 13(3):592–602, 1999. ISSN 08888892. doi:10.1046/j.1523-1739.1999.98099.x. → pages 3, 4

T. M. Howatt and S. E. Allen. Impact of the continental shelf slope on upwelling through submarine canyons. *Journal of Geophysical Research: Oceans*, 118:5814–5828, 2013. ISSN 21699291. doi:10.1002/jgrc.20401. → pages xi, 6, 7, 17, 23, 61, 64, 81

V. A. Huvenne, P. A. Tyler, D. G. Masson, E. H. Fisher, C. Hauton, V. Hühnerbach, T. P. Bas, and G. A. Wolff. A picture on the wall: Innovative mapping reveals cold-water coral refuge in submarine canyon. *PLoS ONE*, 6(12), 2011. ISSN 19326203. doi:10.1371/journal.pone.0028755. → page 3

K.-H. Hyun. *The effect of submarine canyon width and stratification on coastal circulation and across shelf exchange*. PhD thesis, Old Dominion University, 2004. → pages 5, 7, 9, 61, 62, 63, 70

M. Jakobsson. Hypsometry and volume of the Arctic Ocean and its constituent seas. *Geochemistry Geophysics Geosystems*, 3(5):1–18, 2002. doi:10.1029/2001GC000302. → page 20

M. Jakobsson, L. Mayer, B. Coakley, J. A. Dowdeswell, S. Forbes, B. Fridman, H. Hodnesdal, R. Noormets, R. Pedersen, M. Rebesco, H. W. Schenke, Y. Zarayskaya, D. Accettella, A. Armstrong, R. M. Anderson, P. Bienhoff, A. Camerlenghi, I. Church, M. Edwards, J. V. Gardner, J. K. Hall, B. Hell, O. Hestvik, Y. Kristoffersen, C. Marcussen, R. Mohammad, D. Mosher, S. V. Nghiem, M. T. Pedrosa, P. G. Travaglini, and P. Weatherall. The International Bathymetric Chart of the Arctic Ocean (IBCAO) Version 3.0. *Geophysical Research Letters*, 39(L12609), 2012. ISSN 00440477. doi:10.1029/2012GL052219. → page 20

S. Jaramillo Uribe. *Numerical simulation of flow in a laboratory tank using a z-coordinate numerical model*. PhD thesis, The University of British Columbia, 2005. → page 23

N. Jobstvogt, M. Townsend, U. Witte, and N. Hanley. How can we identify and communicate the ecological value of deep-sea ecosystem services? *PLoS ONE*, 9(7), 2014. ISSN 19326203. doi:10.1371/journal.pone.0100646. → page 3

M. P. Johnson, M. White, A. Wilson, L. Würzberg, E. Schwabe, H. Folch, and A. L. Allcock. A vertical wall dominated by Acesta excavata and Neopycnodonte zibrowii, part of an undersampled group of deep-sea habitats. *PLoS ONE*, 8(11), 2013. ISSN 19326203. doi:10.1371/journal.pone.0079917. → page 3

J. Kaempf. Lee effects of localized upwelling in a shelf-break canyon. *Continental Shelf Research*, 42: 78–88, 2012. doi:10.1016/j.csr.2012.05.005. → page 63

J. M. Klinck. The influence of a narrow transverse canyon on initially geostrophic flow. *Journal of Geophysical Research*, 93(C1):509–515, 1988. ISSN 0148-0227. doi:10.1029/JC093iC01p00509. → pages 5, 7

J. M. Klinck. Geostrophic adjustment over submarine canyons. *Journal of Geophysical Research*, 94 (C5):6133–6144, 1989. ISSN 01480227. doi:10.1029/JC094iC05p06133. → pages 5, 7

J. M. Klinck. Circulation near submarine canyons: A modeling study. *Journal of Geophysical Research*, 101(C1):1211–1223, 1996. ISSN 01480227. doi:10.1029/95JC02901. → pages 5, 6, 8

E. A. Kulikov, A. B. Rabinovich, and E. C. Carmack. Barotropic and baroclinic tidal currents on the Mackenzie shelf break in the southeastern Beaufort Sea. *Journal of Geophysical Research*, 109 (C05020), 2004. ISSN 0148-0227. doi:10.1029/2003JC001986. → pages 10, 66

B. Lansard, A. Mucci, L. A. Miller, R. W. MacDonald, and Y. Gratton. Seasonal variability of water mass distribution in the southeastern Beaufort Sea determined by total alkalinity and δ18O. *Journal of Geophysical Research: Oceans*, 117(C03003), 2012. ISSN 21699291. doi:10.1029/2011JC007299. → page 10

D. Leduc, A. A. Rowden, S. D. Nodder, K. Berkenbusch, P. K. Probert, and M. G. Hadfield. Unusually high food availability in Kaikoura Canyon linked to distinct deep-sea nematode community. *Deep-Sea Research Part II: Topical Studies in Oceanography*, 104:310–318, 2014. ISSN 09670645. doi:10.1016/j.dsr2.2013.06.003. → page 3

C. Lique, H. L. Johnson, and P. E. D. Davis. On the Interplay between the Circulation in the Surface and the Intermediate Layers of the Arctic Ocean. *Journal of Physical Oceanography*, 45: 1393–1409, 2015. ISSN 0022-3670. doi:10.1175/JPO-D-14-0183.1. → page 10

J. T. Liu, J. J. Hung, H. L. Lin, C. A. Huh, C. L. Lee, R. T. Hsu, Y. W. Huang, and J. C. Chu. From suspended particles to strata: The fate of terrestrial substances in the Gaoping (Kaoping) submarine canyon. *Journal of Marine Systems*, 76(4):417–432, 2009. ISSN 09247963. doi:10.1016/j.jmarsys.2008.01.010. URL http://dx.doi.org/10.1016/j.jmarsys.2008.01.010. → page 3

Z. Liu and J. Gan. Upwelling induced by the frictional stress curl and vertical squeezing of the vortex tube over a submerged valley in the East China Sea. *Journal of Geophysical Research: Oceans*, 120: 2571–2587, 2015. doi:10.1002/2015JC010715.Received. → page 65

R. W. Macdonald, C. S. Wong, and P. E. Erickson. The distribution of nutrients in the southeastern Beaufort Sea: Implications for water circulation and primary production. *Journal of Geophysical Research: Oceans*, 92(C3):2939–2952, 1987. ISSN 21699291. doi:10.1029/JC092iC03p02939. → pages 11, 63, 64, 71

R. W. Macdonald, E. C. Carmack, F. A. Mclaughlin, K. Iseki, D. M. Macdonald, and M. C. O'brien. Composition and Modification of Water Masses in the Mackenzie Shelf Estuary. *Journal of Geophysical Research*, 94(C12):18057–18070, 1989. doi:10.1029/JC094iC12p18057. → pages 10, 11, 24

G. Madec. NEMO ocean engine. Technical report, Institut Pierre-Simon Laplace (IPSL), France, 2008. → pages 19, 21

G. Madec, P. Delecluse, M. Imbard, and C. Levy. OPA 8 Ocean General Circulation Model - Reference Manual. Technical report, Institut Pierre-Simon Laplace (IPSL), 1998. → page 19

J. Martin, J. É. Tremblay, J. Gagnon, G. Tremblay, A. Lapoussière, C. Jose, M. Poulin, M. Gosselin, Y. Gratton, and C. Michel. Prevalence, structure and properties of subsurface chlorophyll maxima in Canadian Arctic waters. *Marine Ecology Progress Series*, 412:69–84, 2010. ISSN 01718630. doi:10.3354/meps08666. → page 11

J. Martín, P. Puig, A. Palanques, and M. Ribó. Trawling-induced daily sediment resuspension in the flank of a Mediterranean submarine canyon. *Deep-Sea Research Part II: Topical Studies in Oceanography*, 104:174–183, 2014. ISSN 09670645. doi:10.1016/j.dsr2.2013.05.036. → page 3

D. G. Masson, V. A. I. Huvenne, H. C. de Stigter, G. A. Wolff, K. Kiriakoulakis, R. G. Arzola, and S. Blackbird. Efficient burial of carbon in a submarine canyon. *Geology*, 38(9):831–834, 2010. ISSN 00917613. doi:10.1130/G30895.1. → page 4

F. L. Matos, S. W. Ross, V. A. Huvenne, J. S. Davies, and M. R. Cunha. Canyons pride and prejudice: Exploring the submarine canyon research landscape, a history of geographic and thematic bias, 2018. ISSN 00796611. → pages 1, 2

F. A. McLaughlin and E. C. Carmack. Deepening of the nutricline and chlorophyll maximum in the Canada Basin interior, 2003-2009. *Geophysical Research Letters*, 37(L24602):1–5, 2010. ISSN 00948276. doi:10.1029/2010GL045459. → page 71

A. Monier, J. Comte, M. Babin, A. Forest, A. Matsuoka, and C. Lovejoy. Oceanographic structure drives the assembly processes of microbial eukaryotic communities. *The ISME Journal*, 9: 990–1002, 2015. ISSN 17517370. doi:10.1038/ismej.2014.197. → pages 38, 64

H. B. Moors-Murphy. Submarine canyons as important habitat for cetaceans, with special reference to the Gully: A review. *Deep-Sea Research Part II: Topical Studies in Oceanography*, 104:6–19, 2014. ISSN 09670645. doi:10.1016/j.dsr2.2013.12.016. → pages 3, 4, 10

L. A. Mysak. Recent advances in shelf wave dynamics. *Reviews of Geophysics ans Space Physics*, 18 (1):211–241, 1980. ISSN 19449208. doi:10.1029/RG018i001p00211. → page 35

I. Orlanski. A simple boundary condition for unbounded hyperbolic flows. *Journal of Computational Physics*, 1976. ISSN 10902716. doi:10.1016/0021-9991(76)90023-1. → page 21

C. Pasqual, A. Sanchez-Vidal, D. Zúñiga, A. Calafat, M. Canals, X. Durrieu De Madron, P. Puig, S. Heussner, A. Palanques, and N. Delsaut. Flux and composition of settling particles across the continental margin of the Gulf of Lion: The role of dense shelf water cascading. *Biogeosciences*, 7: 217–231, 2010. ISSN 17264189. doi:10.5194/bg-7-217-2010. → page 4

P. Penven, C. Roy, A. de VERDIÈRE, and J. Largier. Simulation of a coastal jet retention process using a barotropic model. *Oceanologica Acta*, 23:615–634, 2000. doi:10.1016/S0399-1784(00)01106-3. → page 62

N. Pérenne, J. W. Lavelle, D. C. Smith IV, and D. L. Boyer. Impulsively started flow in a submarine canyon: Comparison of results from laboratory and numerical models. *Journal of Atmospheric and Oceanic Technology*, 18:1698–1718, 2001. ISSN 07390572. doi:10.1175/1520-0426(2001)018⟨1699:ISFIAS⟩2.0.CO;2. → page 8

R. S. Pickart. Shelfbreak circulation in the Alaskan Beaufort Sea: Mean structure and variability. *Journal of Geophysical Research C: Oceans*, 109(C04024), 2004. ISSN 01480227. doi:10.1029/2003JC001912. → page 10

R. S. Pickart, L. M. Schulze, G. W. K. Moore, M. A. Charette, K. R. Arrigo, G. Van Dijken, and S. L. Danielson. Long-term trends of upwelling and impacts on primary productivity in the Alaskan Beaufort Sea. *Deep-Sea Research I*, 79:106–121, 2013a. ISSN 0967-0637. doi:10.1016/j.dsr.2013.05.003. URL http://dx.doi.org/10.1016/j.dsr.2013.05.003. → page 12

R. S. Pickart, M. A. Spall, and J. T. Mathis. Dynamics of upwelling in the Alaskan Beaufort Sea and associated shelf-basin fluxes. *Deep-Sea Research I*, 76:35–51, 2013b. ISSN 09670637. doi:10.1016/j.dsr.2013.01.007. → page 71

P. Puig, M. Canals, J. B. Company, J. Martín, D. Amblas, G. Lastras, A. Palanques, and A. M. Calafat. Ploughing the deep sea floor. *Nature*, 489, 2012. ISSN 00280836. doi:10.1038/nature11410. → page 3

P. Puig, A. Palanques, and J. Martín. Contemporary Sediment-Transport Processes in Submarine Canyons. *Annual Review of Marine Science*, 6:53–77, 2014. ISSN 1941-1405. doi:10.1146/annurev-marine-010213-135037. → page 3

M. Rail, Y. Gratton, and L. Prieur. Distribution of temperature and salinity in the Canadian Arctic Archipelago during the 2009 ArcticNet sampling expedition. Report No R1248. Technical report, INRS-ETE, 2011. → page 22

K. Ramos-Musalem and S. E. Allen. The Impact of Locally Enhanced Vertical Diffusivity on the Cross-Shelf Transport of Tracers Induced by a Submarine Canyon. *Journal of Physical Oceanography*, 49:561–584, 2019. doi:10.1175/JPO-D-18-0174.1. → pages xi, 16, 23, 65

S. Rennie, C. E. Hanson, R. D. McCauley, C. Pattiaratchi, C. Burton, J. Bannister, C. Jenner, and M. N. Jenner. Physical properties and processes in the Perth Canyon, Western Australia: Links to water column production and seasonal pygmy blue whale abundance. *Journal of Marine Systems*, 77: 21–44, 2009. ISSN 09247963. doi:10.1016/j.jmarsys.2008.11.008. → page 4

J. P. Ryan, F. P. Chavez, and J. G. Bellingham. Physical-biological coupling in Monterey Bay, California: Topographic influences on phytoplankton ecology. *Marine Ecology Progress Series*, 287:23–32, 2005. ISSN 01718630. doi:10.3354/meps287023. → page 4

F. Sanchez, G. Morandeau, N. Bru, and M. Lissardy. A restricted fishing area as a tool for fisheries management: Example of the Capbreton Canyon, southern Bay of Biscay. *Marine Policy*, 42: 180–189, 2013. ISSN 0308597X. doi:10.1016/j.marpol.2013.02.009. → page 3

A. Sanchez-Vidal, M. Canals, A. M. Calafat, G. Lastras, and R. Pedrosa-Pàmies. Impacts on the Deep-Sea Ecosystem by a Severe Coastal Storm. *PLoS ONE*, 7(1):30395, 2012. doi:10.1371/journal.pone.0030395. URL www.plosone.org. → page 3

F. Sardà, J. E. Cartes, and J. B. Company. Spatio-temporal variations in megabenthos abundance in three different habitats of the Catalan deep-sea (Western Mediterranean). *Marine Biology*, 120: 211–219, 1994. ISSN 00253162. doi:10.1007/BF00349681. → page 3

M. C. Serreze and A. P. Barrett. Characteristics of the Beaufort Sea high. *Journal of Climate*, 24: 159–182, 2011. ISSN 08948755. doi:10.1175/2010JCLI3636.1. → page 10

J. She and J. M. Klinck. Flow near submarine canyons driven by constant winds. *Journal of Geophysical Research: Oceans*, 105(C12):28671–28694, 2000. ISSN 01480227. doi:10.1029/2000JC900126. → pages 5, 6, 8, 62

N. Skliris, J. H. Hecq, and S. Djenidi. Water fluxes at an ocean margin in the presence of a submarine canyon. *Journal of Marine Systems*, 32:239–251, 2002. ISSN 09247963. doi:10.1016/S0924-7963(02)00036-2. → page 65

M. Sobarzo, G. S. Saldías, F. J. Tapia, L. Bravo, C. Moffat, and J. L. Largier. On subsurface cooling associated with the Biobio River Canyon (Chile). *Journal of Geophysical Research: Oceans*, 2016. ISSN 21699291. doi:10.1002/2016JC011796. → page 63

J. É. Tremblay, S. Bélanger, D. G. Barber, M. Asplin, J. Martin, G. Darnis, L. Fortier, Y. Gratton, H. Link, P. Archambault, A. Sallon, C. Michel, W. J. Williams, B. Philippe, and M. Gosselin. Climate forcing multiplies biological productivity in the coastal Arctic Ocean. *Geophysical Research Letters*, 38, 2011. doi:10.1029/2011GL048825. → page 71

J. E. Tremblay, P. Raimbault, N. Garcia, B. Lansard, M. Babin, and J. Gagnon. Impact of river discharge, upwelling and vertical mixing on the nutrient loading and productivity of the Canadian Beaufort Shelf. *Biogeosciences*, 2014. ISSN 17264189. doi:10.5194/bg-11-4853-2014. → page 71

E. W. Vetter, C. R. Smith, and F. C. De Leo. Hawaiian hotspots: Enhanced megafaunal abundance and diversity in submarine canyons on the oceanic islands of Hawaii. *Marine Ecology*, 2010. ISSN 01739565. doi:10.1111/j.1439-0485.2009.00351.x. → pages 3, 4

A. F. Waterhouse. Influence of Mackenzie Canyon on water mass transformation in the Beaufort Continental Slope. → pages 23, 39

A. F. Waterhouse, S. E. Allen, and A. W. Bowie. Upwelling flow dynamics in long canyons at low Rossby number. *Journal of Geophysical Research*, 114(C05004), 2009. ISSN 21699291. doi:10.1029/2008JC004956. → pages 7, 8, 61, 62

A. F. Waterhouse, J. A. Mackinnon, R. C. Musgrave, S. M. Kelly, A. Pickering, and J. Nash. Internal Tide Convergence and Mixing in a Submarine Canyon. *Journal of Physical Oceanography*, 47: 303–322, 2017. ISSN 0022-3670. doi:10.1175/JPO-D-16-0073.1. → page 23

W. J. Williams and E. C. Carmack. Combined effect of wind-forcing and isobath divergence on upwelling at Cape Bathurst, Beaufort Sea. *Journal of Marine Research*, 66:645–663, 2008. ISSN 00222402. doi:10.1357/002224008787536808. URL http://www.ingentaconnect.com/content/jmr/jmr/2008/00000066/00000005/art00004. → page 10

W. J. Williams and E. C. Carmack. The 'interior' shelves of the Arctic Ocean: Physical oceanographic setting, climatology and effects of sea-ice retreat on cross-shelf exchange. *Progress in Oceanography*, 2015. ISSN 00796611. doi:10.1016/j.pocean.2015.07.008. → page 71

W. J. Williams, E. C. Carmack, K. Shimada, H. Melling, K. Aagaard, R. W. Macdonald, and R. Grant Ingram. Joint effects of wind and ice motion in forcing upwelling in Mackenzie Trough, Beaufort Sea. *Continental Shelf Research*, 26:2352–2366, 2006. ISSN 02784343. doi:10.1016/j.csr.2006.06.012. → pages xii, 5, 9, 10, 11, 12, 13, 18, 23, 63, 64, 66

M. Yamamoto-kawai. Aragonite Undersaturation in the Arctic Ocean : Effects of Ocean Acidification and Sea Ice Melt. *Science*, 326:1098–1100, 2009. doi:10.1126/science.1174190. → page 71

W. G. Zhang and S. J. Lentz. Wind-driven circulation in a shelf valley. Part I: Mechanism of the asymmetrical response to along-shelf winds in opposite directions. *Journal of Physical Oceanography*, 47:2927–2947, 2017. ISSN 0022-3670. doi:10.1175/JPO-D-17-0083.1. → pages 13, 63

D. Zúñiga, M. M. Flexas, A. Sanchez-Vidal, J. Coenjaerts, A. Calafat, G. Jordà, J. García-Orellana, J. Puigdefàbregas, M. Canals, M. Espino, F. Sardà, and J. B. Company. Particle fluxes dynamics in Blanes submarine canyon (Northwestern Mediterranean). *Progress in Oceanography*, 82:239–251, 2009. ISSN 00796611. doi:10.1016/j.pocean.2009.07.002. → page 4

Appendix A

Relevant variables and numbers

Notation	Definition	Value
a	radius of deformation ($a = \frac{NH_c}{f}$)	2.38×10^4 m
Bu	Burger number $Bu = \left(\frac{NH_c}{fW}\right)^2$	0.144
D_h	depth scale Howatt and Allen (2013) ($D_h = \frac{fL}{N_s}$)	5.19×10^2 m
f	Coriolis parameter	1.37×10^{-4} s^{-1}
$\mathcal{F}_{W*}$	function of R_{W*} ($\mathcal{F}_{W*} = \frac{R_{W*}}{(0.9 + R_{W*})}$)	0.0193
H_c	depth of the canyon at the mouth	372 m
H_h	depth of the canyon at the head	40 m
H_s	depth at shelf break	79.6 m
H_w	depth of the coast	39.6 m
L	length of the canyon	9.87×10^4 m
L_{sw}	distance between the coast and shelf break	1.15×10^5 m
N	Brunt-Väisälä frequency (averaged from surface to 500 m depth)	8.76×10^{-3} s^{-1}
N_s	Brunt-Väisälä frequency (averaged from surface to shelf break depth)	2.61×10^{-2} s^{-1}
R_{W*}	Rossby number ($R_{W*} = \frac{U}{f\mathcal{R}_W}$)	0.0177
R_L	canyon length-based Rossby Number ($R_L = \frac{U}{fL}$)	0.00836
$\mathcal{R}_W$	width of the canyon at half-length	4.65×10^4 m
s	continental shelf slope ($s = \frac{H_s - H_w}{L_{sw}}$)	3.48×10^{-4}
S_E	slope effect ($\frac{sN_s}{f}\left(\frac{\mathcal{F}_{W*}}{R_L}\right)^{1/2}$)	0.101
U	upstream (along-slope) velocity	0.113 m s^{-1}
W	width of the canyon at the mouth	6.27×10^4 m
$\mathcal{Z}$	upwelling depth of the deepest isopycnal to reach the canyon head Howatt and Allen (2013) ($\mathcal{Z} = D_h[1.8(\mathcal{F}_{W*}R_L)^{1/2}(1 - 0.42S_E) + 0.05]$)	37.3 m

Table A.1: Values of relevant variables and numbers for the base wind forcing case.

Appendix B

Additional details of methodology

B.1 Sea surface elevation calculation

The solution for the barotropic Rossby adjustment over a shelf Allen (1996) referred to in Section 2.1 is:

$$\eta = -\frac{\int_{t_0}^{t_f} \tau dt}{f \rho a_s} \left(\frac{1}{\alpha \sinh(S/a_s) + \cosh(S/a_s)} \right) \exp\left[\frac{-(y-S)}{a_d} \right] \tag{B.1}$$

where η is the surface elevation, τ is a steady and uniform wind stress in the alongshore direction, f is the Coriolis frequency, g is the gravitational acceleration, ρ is density, S is the distance to the shelf break, H_S is the depth of the shelf break, H_D is the maximum depth of the domain, $a_S = \frac{\sqrt{gH_S}}{f}$ is the barotropic Rossby number over the shelf, $a_D = \frac{\sqrt{gH_D}}{f}$ is the barotropic Rossby radius off the shelf, and $\alpha = \sqrt{H_S/H_D}$.

B.2 Wind stress formulation

The modified formulation for wind stress used to force the model referred to in Section 2.2 is:

$$\tau_x^{pulse} = \tau_{x-max}^{pulse} \times \frac{1}{2}\left(1 - \cos\left(\frac{f \times k \times \Delta t}{2}\right)\right) \tag{B.2}$$

$$\tau_x^{relax} = \tau_{x-const}^{relax} \times \frac{1}{2}\left(1 + \tanh\left(\frac{k - k_{relax}/2}{k_{relax}/6}\right)\right) \tag{B.3}$$

$$\tau_x = \begin{cases} \tau_x^{pulse} + \tau_x^{relax}, & \text{if } k \leq k_{relax} \\ \tau_x^{relax}, & \text{otherwise} \end{cases} \tag{B.4}$$

$$k_{relax} = \frac{t_{relax}}{\Delta t} \tag{B.5}$$

where τ_x is the alongshore component for wind stress, τ_x^{pulse} is a strong wind pulse with a maximum wind stress value τ_{x-max}^{pulse}, τ_x^{relax} is a reduced constant wind stress with a wind stress value $\tau_{x-const}^{relax}$, f is the Coriolis parameter, k is the model time step counter, Δt is the baroclinic time step in seconds, t_{relax} is the time in seconds when τ_x^{pulse} switches to τ_x^{relax}, and k_{relax} is the time step that corresponds to the time t_{relax}.
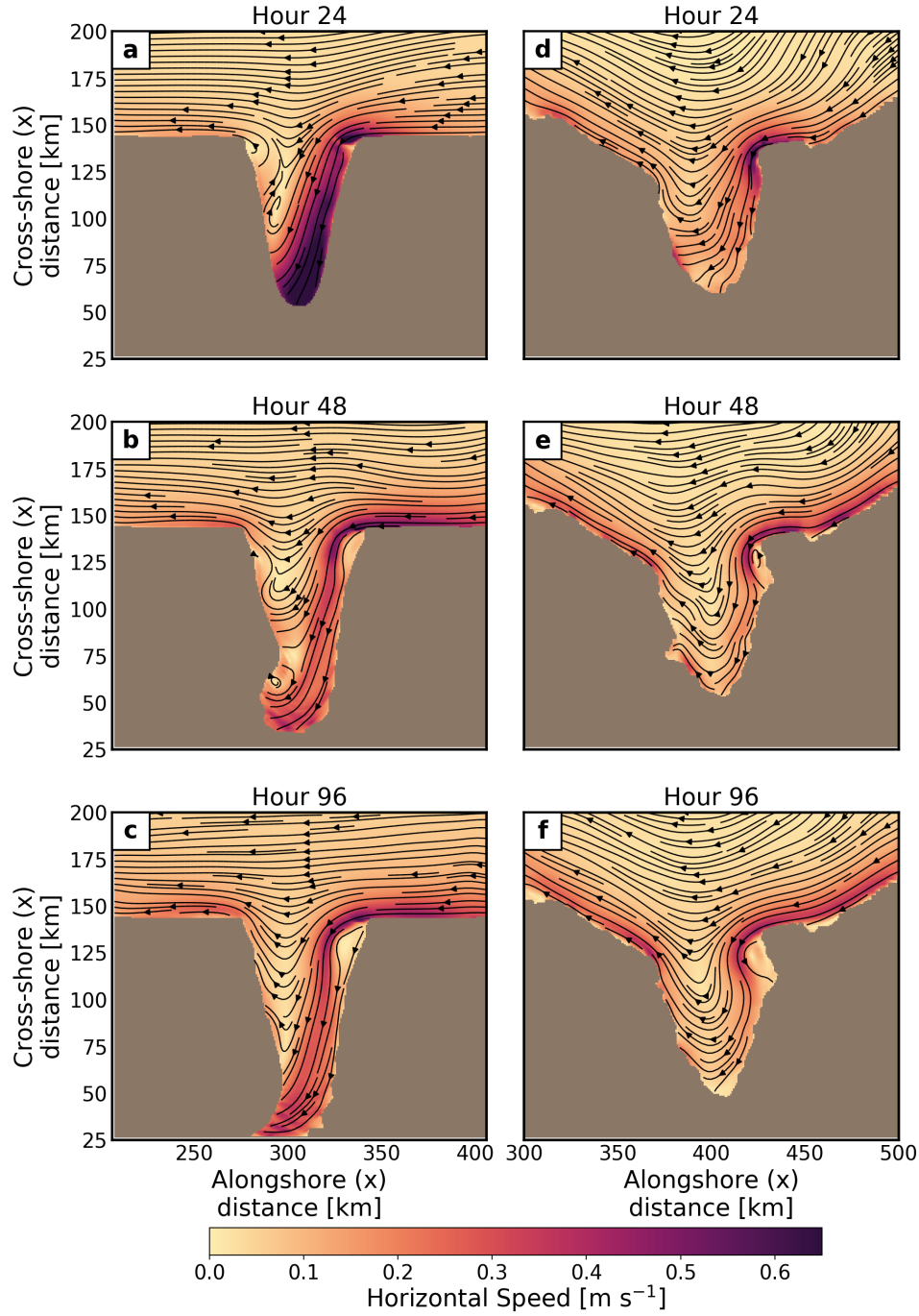
Appendix C

Additional figures

## C.1 Wave signal at the eastern edge of the model domain
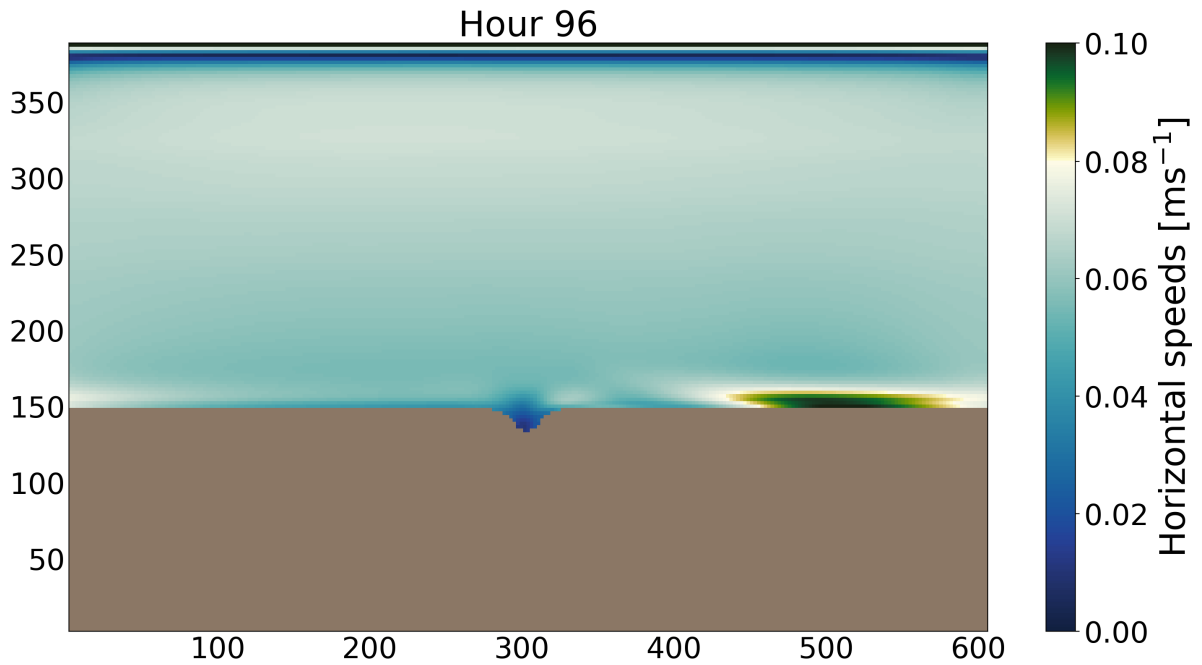
Figure C.1: Plan view of horizontal speeds $[\mathrm{m\,s^{-1}}]$ on the AW-representative surface at hour 96 in the idealized model.

C.2 Flow speed and direction as 1-hour averages


Figure C.2: Plan views depicting horizontal speed [m s^{-1}] and direction of flows on the UHW-representative surface at hours 24, 48, and 96 in the (a-c) idealized and (d-f) realistic models. Speed is depicted by the colouring and direction is depicted by the flow lines on the surface. The flow lines shown in this figure are not streamlines. The flow lines show flow direction only; these do not show flow speed.

C.3 Wave propagation on the salinity surface representative of the Atlantic Water
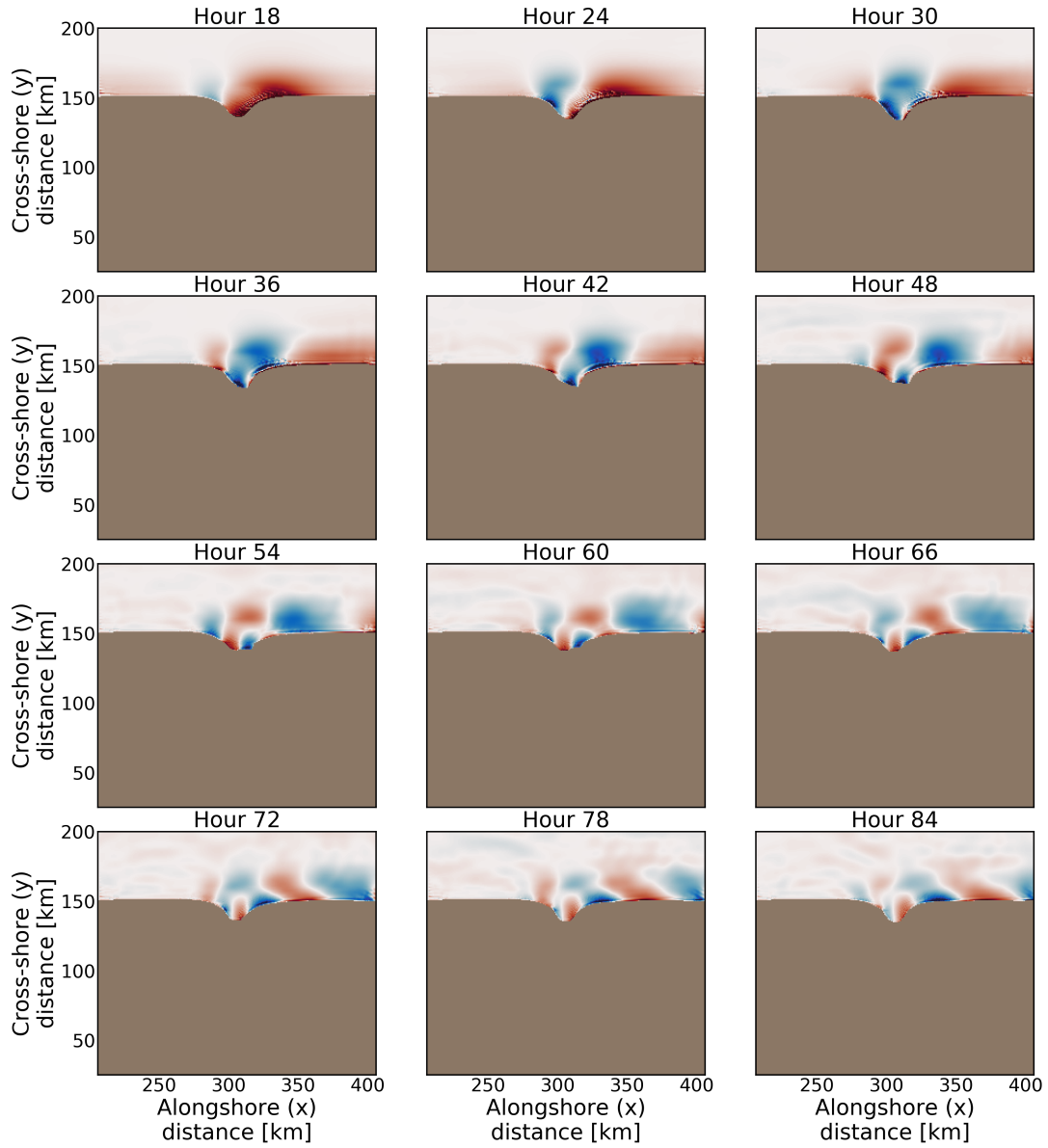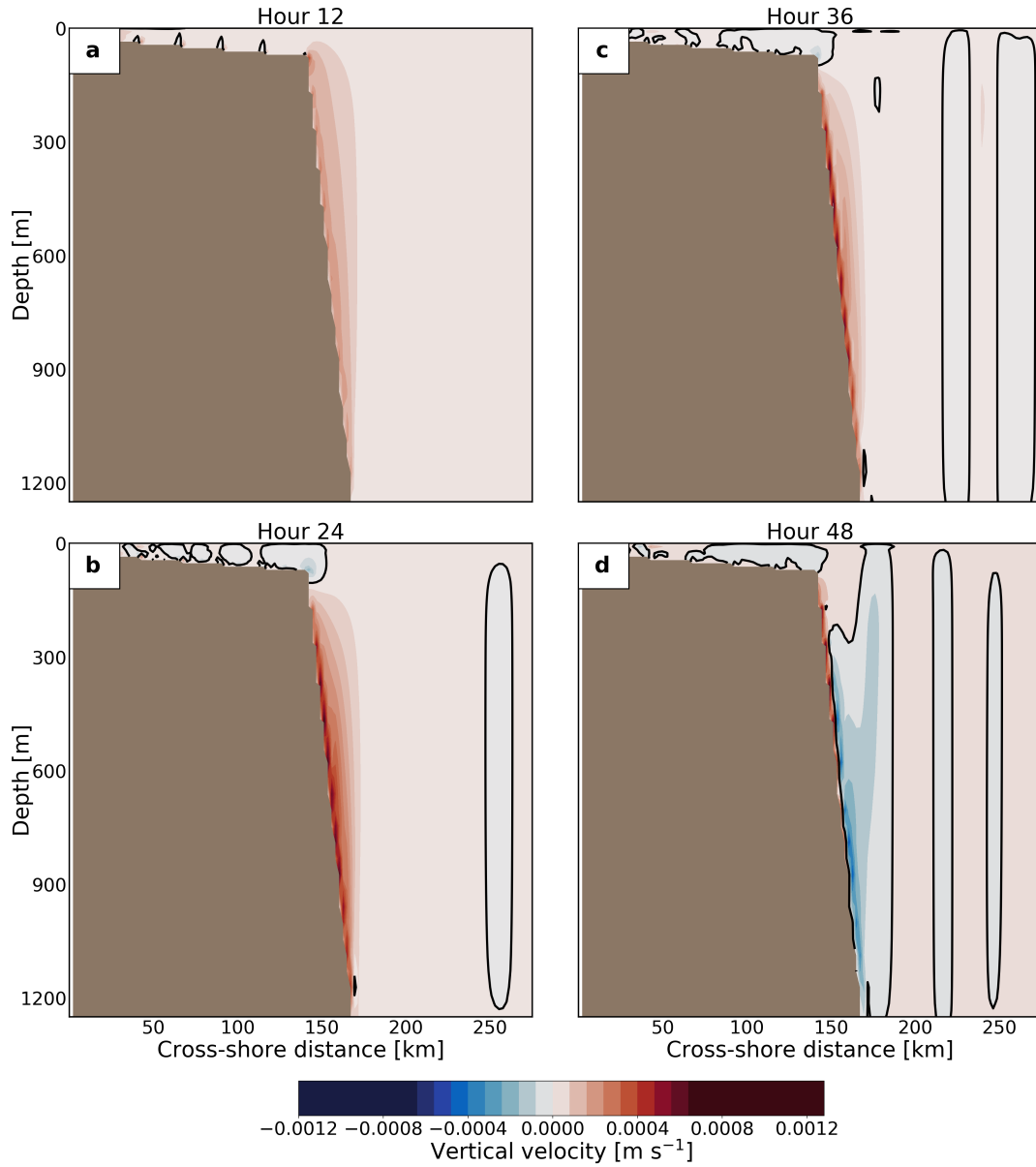

Figure C.3: Vertical velocity 1-hour averages showing the propagation and modification of the coastal trapped wave on the AW-representative surface between hours 18 and 84.

C.4 Structure of the lowest wave mode computed by the coastal trapped wave model
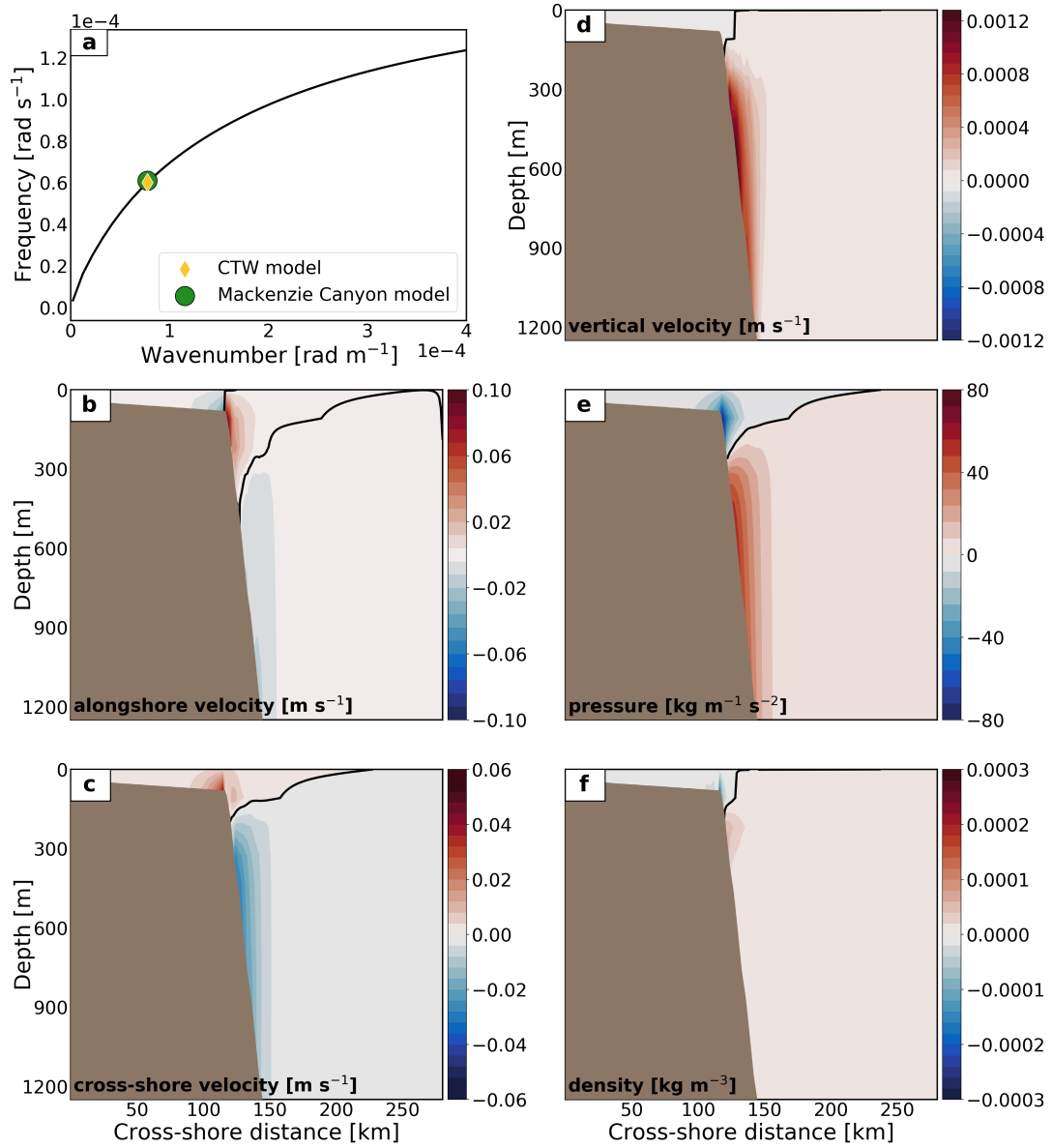
Figure C.4: Structure of the lowest wave mode calculated by the CTW model. a) Dispersion curve and vertical, cross-shore structure for b) u-velocity component $[\mathrm{m\,s^{-1}}]$, c) v-velocity component $[\mathrm{m\,s^{-1}}]$, d) w-velocity component $[\mathrm{m\,s^{-1}}]$, e) pressure $[\mathrm{kg\,m^{-1}\,s^{-2}}]$, and f) density $[\mathrm{kg\,m^{-3}}]$ of the lowest wave mode as calculated by the CTW model for the cross-shore bathymetry profile outlined by the dashed, black line in Figure 3.11. In panel (a), the green circle marks the wavenumber and frequency estimated between hours 24 and 36 for the CTW observed in the Mackenzie Canyon model simulations; the yellow diamond marks the wavenumber and frequency of the lowest wave mode computed by the CTW model. The magnitudes for all values (b-f) have been normalized for comparison with the Mackenzie Canyon model results.

## C.5 Structure for vertical velocity of the coastal trapped wave in the Mackenzie Canyon model simulations

Figure C.5: Evolution of the cross-shore structure for vertical velocity $[\mathrm{m\,s^{-1}}]$ of the CTW in the Mackenzie Canyon model simulations. The wave structure becomes more complex in time, as depicted by the 1-hour averages for hours a) 12, b) 24, c) 36, and d) 48.

Appendix D

Schematics

D.1 Circulation in narrow canyons
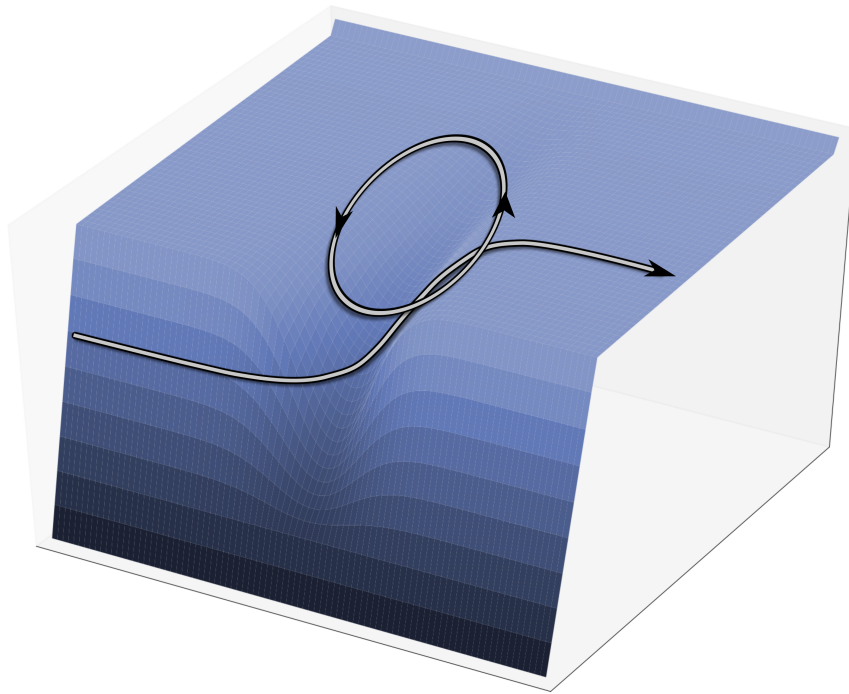
Figure D.1: Schematic of general circulation and upwelling in narrow canyons. Shelf and slope currents flow past the upstream side of the canyon mouth before being deflected onshore near the downstream wall. At the downstream wall, flows either upwell onto the shelf, continue towards the head, or turn offshore to exit the canyon. Cyclonic circulation in the canyon evolves into a cyclonic eddy at the canyon rim depth that spans the canyon width.

D.2 Circulation in Mackenzie Canyon
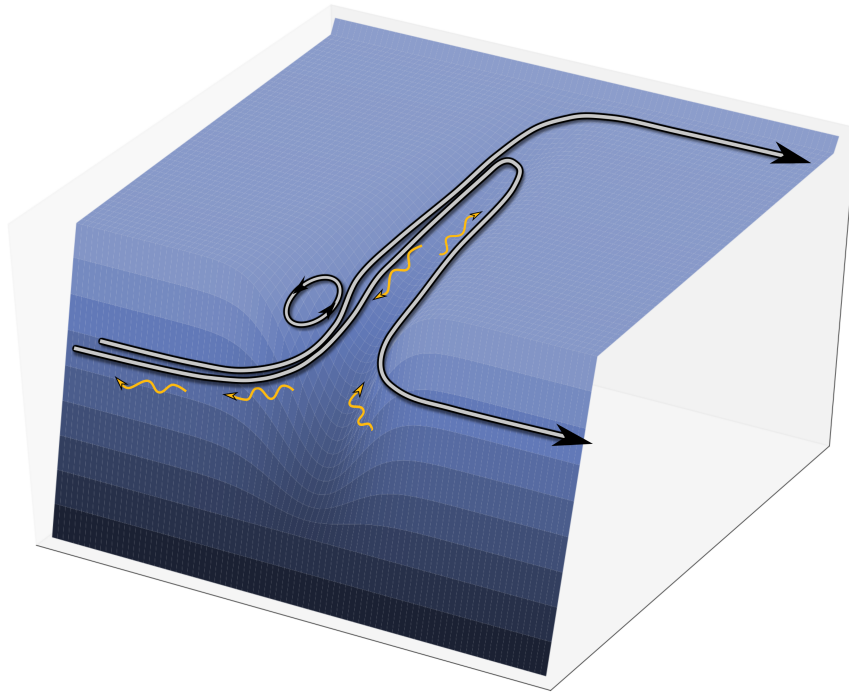
Figure D.2: Schematic of general circulation and upwelling in Mackenzie Canyon. Flows are topographically steered around the canyon walls. An onshore-directed jet encounters the canyon topography at the head, and upwelled flows are advected downstream. Along-slope flows separate from the topography on the upstream corner of the canyon mouth, resulting in the generation of high vorticity flows and the subsequent formation of a cyclonic eddy. The attached cyclonic eddy on the upstream corner of the canyon mouth becomes a site for strong upwelling. A coastal trapped wave is generated on the downstream side of the canyon and propagates the canyon upwelling signal upstream along the upstream wall and slope.